

**INTERACTION OF ALUMINIDE COATED Ni-Cr-Fe BASED  
SUPERALLOY SUBSTRATES WITH SIMULATED NUCLEAR WASTE  
AND BOROSILICATE GLASS**

By

**YUSUFALI C**

(CHEM01200904020)

Bhabha Atomic Research Centre, Mumbai

*A thesis submitted to the  
Board of Studies in Chemical Sciences*

*In partial fulfillment of requirements  
For the Degree of*

**DOCTOR OF PHILOSOPHY**

*of*

**HOMI BHABHA NATIONAL INSTITUTE**



**June, 2015**

# Homi Bhabha National Institute

## Recommendations of the Viva Voce Committee

As members of the Viva Voce Committee, we certify that we have read the dissertation prepared by **Mr. Yusufali C.** entitled "**Interaction of aluminide coated Ni-Cr-Fe based superalloy substrates with simulated nuclear waste and borosilicate glass**" and recommend that it may be accepted as fulfilling the thesis requirement for the award of Degree of Doctor of Philosophy.

Chairman – Prof. D. Das

*D. Das.*

Date:23/03/2017

Guide / Convener – Dr. R. J. Kshirsagar

*R. J. Kshirsagar*

Date:23/03/2017

Co-guide - Prof. G. K. Dey

*Gautam Kumar Dey*

Date:23/03/2017

Examiner – Dr. R. Jayaganthan

*R. Jay*

Date:23/03/2017

Member 1- Dr. V. Sudarsan

*Sudarsan.V*

Date:23/03/2017

Member 2- Dr. R. S. Dutta

*Rajeev Kumar Dutta*

Date:23/03/2017

Final approval and acceptance of this thesis is contingent upon the candidate's submission of the final copies of the thesis to HBNI.

We hereby certify that we have read this thesis prepared under our direction and recommend that it may be accepted as fulfilling the thesis requirement.

Date: March 23, 2017

Place: Mumbai

*Gautam Kumar Dey*

Prof. G. K. Dey  
(Co-guide)

*R. J. Kshirsagar*

Dr. R. J. Kshirsagar  
(Guide)

## STATEMENT BY AUTHOR

This dissertation has been submitted in partial fulfillment of requirements for an advanced degree at Homi Bhabha National Institute (HBNI) and is deposited in the Library to be made available to borrowers under rules of the HBNI.

Brief quotations from this dissertation are allowable without special permission, provided that accurate acknowledgement of source is made. Requests for permission for extended quotation from or reproduction of this manuscript in whole or in part may be granted by the Competent Authority of HBNI when in his or her judgment the proposed use of the material is in the interests of scholarship. In all other instances, however, permission must be obtained from the author.



(Yusufali C)

## DECLARATION

I, hereby declare that the investigation presented in the thesis has been carried out by me.  
The work is original and has not been submitted earlier as a whole or in part for a  
degree/diploma at this or any other Institution / University.

A handwritten signature in blue ink, appearing to be 'Yusufali C', written in a cursive style.

(Yusufali C)

## List of publications arising from the thesis

1. Infrared and X-ray photoelectron spectroscopy studies on sodium borosilicate glass interacted with thermally oxidized aluminides formed on Alloy 690

**C. Yusufali**, R.J. Kshirsagar, Jagannath, R.K. Mishra, R.S. Dutta and G.K. Dey, *J. Non-Cryst. Solids* 366 (2013) 54-58.

2. Surface studies on aluminized and thermally oxidized Alloy 690 substrates interacted with nitrate-based simulated nuclear waste and sodium borosilicate melt using Raman spectroscopy and X-ray photoelectron spectroscopy

**C. Yusufali**, R.J. Kshirsagar, Jagannath, R. Halder, G.J. Abraham, R.K. Mishra, C.P. Kaushik, R.S. Dutta and G.K. Dey, *Surf. Coat. Technol.* 266 (2015) 31-37.

### Other Publications:

1. Surface Studies On Aluminized And Thermally Oxidized Superalloy 690 Substrates Interacted With Simulated Nuclear Waste And Sodium Borosilicate Melt

**C. Yusufali**, R.J. Kshirsagar, R.K. Mishra, C.P. Kaushik, P. Sengupta, R.S. Dutta and G.K. Dey, *AIP Conf. Proc.* 1591 (2014) 861-863

2. Formation of diffusion barrier coating on superalloy 690 substrate and its stability in borosilicate glass at elevated temperature

R.S. Dutta, **C. Yusufali**, B. Paul, S. Majumdar, P. Sengupta, R.K. Mishra, C.P. Kaushik, R.J. Kshirsagar, U.D. Kulkarni, G.K. Dey, *J. Nucl. Mater.* 432 (2013) 72-77

3. Thermally grown oxide layer on aluminized superalloy 690 substrate and its stability in nitrate-based environment

R.S. Dutta, **C. Yusufali**, S. Majumdar, R. K. Mishra, C. P. Kaushik, R.J. Kshirsagar, U. D. Kulkarni and G. K. Dey, *Mater. Sci. Forum* 710 (2012) 733

4. Formation of aluminides on Ni-based superalloy 690 substrate, their characterization and first principle Ni (111)/NiAl(110) interface simulations  
R.S. Dutta, A. Arya, **C. Yusufali**, B. Vishwanadh, R. Tewari, G.K. Dey, *Surf. Coat. Technol.* 235 (2013) 741-747

### **Conferences/Symposia:**

1. International Conference of Electron Microscope Society of India-2011 (EMSI), Hyderabad, India.
2. Materials and Processing-2012 (MAP), Mumbai, India.
3. International Conference on Advances in Metallic Materials and Manufacturing Processes for Strategic Sectors-2012 (ICAMPS), Thiruvananthapuram, India.
4. Department of Atomic Energy-Solid State Physics Symposium-3013 (DAE-SSPS), Patiala, India.
5. Research Scholars Meet-2012, S.I.E.S. College of Arts, Science and Commerce, Sion, Mumbai.

  
(Yusufali C)

*To*  
*My beloved parents and family*

## ***Acknowledgements***

*First and foremost, I would like to praise Almighty God for blessing, protecting and endowing me with power and patience to chase the dream and to accomplish the task. His guidance in difficult situation, his support in the time of hardship and his un-conditional mercy towards me made this thesis in reality. Again I thank him.*

*I would like to express my deep sense of gratitude and sincere thanks to my guide, Dr. R.J. Kshirsagar for his invaluable guidance, constant encouragement, unstinted inspiration, keen interest, good wishes and valuable suggestions throughout my research period. I am also grateful to him for critically reviewing this thesis.*

*It gives me immense pleasure to acknowledge to my co-guide Prof. G.K. Dey for excellent supervision, incredible support and ceaseless encouragement. Your valuable suggestions and critical evaluation of my research activities time to time shaped my work better.*

*This thesis would not have been possible without the guidance, help, support, critical analysis and valuable suggestions from Dr. R.S. Dutta. I am also thankful to him for sharing his excellent knowledge and scientific understanding with me throughout the work. His enthusiasm, deep engagement in research and critical analysis strategy of experimental data has made a deep impression on me.*

*I would like to thank all members of doctoral committee for their critical review and suggestions during annual review presentations and pre-synopsis viva-voce. The committee members are Prof. D. Das (Chairman), Dr. R.J. Kshirsagar (Guide & Convenor), Prof. G.K. Dey (Co-guide), Dr. V. Sudarsan, Dr. U.D. Kulkarni (Former member) and Dr. R.S. Dutta.*

*I utilize this opportunity to thank Dr. R. Tewari for critically reviewing my thesis. I also thank Dr. R.K. Mishra, Dr. Jagannath, Dr. Geogy Abraham, Dr. S. Majumdar, B. Paul and Mr. Nachiket for providing me experimental and analytical support at various stages of my work. I also thank Dr. A. Laik and Dr. P. Sengupta for their support, encouragement and constructive criticism particularly while reviewing this thesis.*

*It is great pleasure to acknowledge my colleagues Dr. Nitin, Dr. Pooja, Mrs. Rumu, Mr. Srikanth, Mr. Sanjay, Mr. Adiga and Mr. Gawde for helping me and providing kind support and encouragement during my research work. I am also thankful to all my Materials Science Division colleagues and staff members of division office for their support at different times. I am grateful to DAE for giving me this opportunity and providing fellowship during this course of work.*

*I also extend my thanks to Mohammedali, Joy, Abdul Salam, Anand, Yunus, Sadiq, Ranjith, Shareef, Askar, Vidhu, Musthafa, Shafeeq, Arun, Sunil, Rammohan for their moral support during the period of my doctoral work.*

*Words fail me to express my appreciation to my roommates Dilip, Abdulla, Gangamallaiah, Ahmed, Khaisar, Suresh, Venkateshwararao, Vivek, Rajamurthy, Kamal for their close companionship and unconditional support during these years. I never forget those amazing moments that I had spent with all of you. I also thank Naresh and family, Satish and family and Dr. Pattanaik for their support and constant inspiration. I also extend thanks to my batch mates Avishek, Jerina, Shagufta, Vasundhara, Suman, Monika, Shikha and Debashree.*

*Also I am very thankful to my friends Aslam, Kareem, Thahir, Rafi, Rijeesh, Hashim, Sajeer, Nishad Perur, Jalaludheen, Aslam Pathiriyal, Ashraf, Anees, Vijayakumar, Ibrahim, Yusufali, Nishad, Firoz, Sirajudheen, Yusuf Poruthiyil, and Usman for their support and constant encouragement at different aspects and cherishing up during hardship times.*

*Finally, to my family, my words are not sufficient to express my heartfelt gratitude to my family members for their support, love and prayer. My beloved mother, Mrs. Ayisha who is my strength and it is her prayers and blessings that drive me. My father, Mr. Moosa who have always supported me with encouraging words. To my wife Jasna, thanks for being with me in every moments of my life with an unconditional love and care, who endured all my limitations with high patience. My eldest brother, Mohd. Rafeeq who always encouraged my education and accomplishments at every turn. Thanks to my brothers Anwar sadath and Musthafa, who bring joy to my life. I also thank my sister-in-laws for their support and prayers. Thanks are extended to my mother- and father-in-laws for their love and understanding.*

  
(Yusufali C)

# CONTENTS

	Page No.
<b>SYNOPSIS</b>	Xv
<b>LIST OF FIGURES</b>	Xxviii
<b>LIST OF TABLES</b>	Xxxvii
<b>Chapter 1: Introduction</b>	<b>1–4</b>
1.1 Background	1
1.2 Scope of the thesis	2
1.3 Outline of the thesis	3
<b>Chapter 2: Literature Review</b>	<b>5–28</b>
<b>2.1 Interaction of metals and alloys with molten glasses</b>	<b>5</b>
2.1.1 Interaction of chromium alloys with molten silicate glass	7
2.1.2 Interaction of chromium oxide with molten silicate glass	8
2.1.3 Interaction of nickel-based alloys with molten silicate glass	10
<b>2.2 Interaction of alloys with nuclear waste solution</b>	<b>16</b>
<b>2.3 Glass—a candidate material for immobilization of HLW</b>	<b>17</b>
2.3.1 Glass formation	19
2.3.2 Glass structure	21

---

2.3.3 Effect of foreign elements in glass structure	25
<b>2.4 Summary</b>	<b>27</b>
<b>Chapter 3: Experimental Methods and Characterization Techniques</b>	<b>29–51</b>
<b>3.1 Pack Aluminization</b>	<b>29</b>
<b>3.2 Thermal Oxidation</b>	<b>31</b>
<b>3.3 Exposure to Simulated Nuclear Waste</b>	<b>32</b>
<b>3.4 Exposure in Sodium Borosilicate Glass</b>	<b>34</b>
<b>3.5 Characterization Techniques</b>	<b>37</b>
3.5.1 Scanning Electron Microscopy (SEM) with Energy Dispersive X-ray Spectroscopy (EDS)	37
3.5.2 Electron Probe Micro-Analysis (EPMA)	40
3.5.3 Fourier Transform–Infrared Spectroscopy (FT-IR)	42
3.5.4 Micro-Raman Spectroscopy	45
3.5.5 X-ray Photoelectron Spectroscopy (XPS)	48
<b>Chapter 4: Interaction of aluminized (using high Al-containing pack) and oxidized Alloy 690 with simulated nuclear waste and sodium borosilicate melts</b>	<b>53–84</b>
<b>4.1 Introduction</b>	<b>53</b>
<b>4.2 Experimental Methods</b>	<b>54</b>

<b>4.3 Results</b>	55
4.3.1 Microstructure of aluminide coatings	55
4.3.2 Interaction of aluminized and thermally oxidized Alloy 690 specimen	56
4.3.2.1 Specimens exposed to simulated nuclear waste solution (Set A)	56
4.3.2.2 Specimens exposed to sodium borosilicate melt (Set B)	61
4.3.3 Interaction of bare Alloy 690 substrate	66
4.3.3.1 Specimens exposed to simulated nuclear waste solution	66
4.3.3.2 Specimens exposed to sodium borosilicate melt	69
<b>4.4 Discussions</b>	73
<b>4.5 Conclusions</b>	83
<b>Chapter 5: Interaction of aluminized (using low Al-containing pack) and oxidized Alloy 690 with simulated nuclear waste and sodium borosilicate melts</b>	<b>85–103</b>
<b>5.1 Introduction</b>	85
<b>5.2 Experimental Methods</b>	85
<b>5.3 Results</b>	86
5.3.1 Microstructure of aluminide coatings	86
5.3.2 Specimens exposed to simulated nuclear waste solution (Set C)	87
5.3.3 Specimens exposed to sodium borosilicate melt (Set D)	94

<b>5.4 Discussions</b>	100
<b>5.5 Conclusions</b>	102
<b>Chapter 6: Characterization of interacted sodium borosilicate glass</b>	<b>105–122</b>
<b>6.1 Introduction</b>	105
<b>6.2 Experimental Methods</b>	106
<b>6.3 Results</b>	107
6.3.1 Characterization of sodium borosilicate glass interacted with aluminized (with high Al-containing pack) and oxidized Alloy 690 specimen	107
6.3.1.1 FT-IR results	107
6.3.1.2 XPS spectra	109
6.3.2 Glass interacted with aluminized (with low Al-containing pack) and oxidized Alloy 690 specimen	111
6.3.2.1 Micro-Raman spectra	111
6.3.2.2 XPS spectra	113
<b>6.4 Discussions</b>	115
<b>6.5 Conclusions</b>	122
<b>Chapter 7: Summary and future scope</b>	<b>123–124</b>
Scope for future work	124

<b>References</b>	125
<b>List of Publications</b>	135

---

## Synopsis

Management of high level radioactive liquid waste (HLW) produced during the reprocessing of irradiated nuclear fuel is a challenging activity faced by nuclear industry. Vitrification of HLW in borosilicate glass is considered to be one of the most acceptable immobilization methods available today [1-2]. Out of various types of vitrification processes, processes based on induction heated metallic melter pot method and Joule heated ceramic melter pot method are widely followed at the Waste Immobilization plant scale [3-4]. The majority of the alloys and superalloys in contact with molten glasses that are used in the glass industry contain upto 30 wt% chromium. Upon exposure to molten glass, these alloys develop a chromia ( $\text{Cr}_2\text{O}_3$ ) layer at the metal/glass interface and the chromia layer exhibits low solubility in molten glass even at elevated temperature. Below the depassivation temperature and glass compositions with lower basicity, the chromia layer passivates the alloys and leads to low corrosion rates [5-10]. Therefore, Ni-based superalloys having about 30% of chromium are generally used as process pot, susceptor in multi-zone induction heated metallic melter pot furnace and the electrodes in Joule heated ceramic melter pot [3,11]. However, because of depletion of Cr adjacent to  $\text{Cr}_2\text{O}_3$  layer in Alloy 690 surfaces and flaking off thick Cr-oxide layer due to development of compressive stress, leaching out of Cr from the alloy takes place [11,12]. To increase the service life of vitrification furnace materials, efforts are being made to develop suitable coatings on superalloy substrates [11,13,14]. However, detailed interaction of aluminide coatings with simulated waste and borosilicate melt has not been studied so far. Keeping this in view, aluminized and oxidized Alloy 690 specimens have been exposed to simulated nuclear waste solution (nitrate-based environment) at 373 K for 216 hours and sodium borosilicate melt at 1248 K for 192 hours. This is followed by characterization of exposed specimens using various techniques such as, Raman spectroscopy, X-ray

photoelectron spectroscopy (XPS), electron probe microanalyzer (EPMA) and scanning electron microscopy (SEM) with energy dispersive X-ray spectroscopy (EDS). In addition, exposed sodium borosilicate glass has been characterized using Fourier transform infrared (FT-IR) spectroscopy, Raman spectroscopy, and XPS. The results of interaction have been discussed in detail in this thesis comprising seven chapters. A brief description of each chapter is given below.

## **Chapter 1**

This chapter gives a description of the background and motivation of the present work. Efforts are being pursued to improve the service life of vitrification furnace materials that are part of nuclear waste immobilization plants, by developing suitable coatings on superalloy substrates. But detailed investigations relating to interactions of these coated materials with environments pertaining to nuclear waste immobilization plant, e.g. nuclear waste solution and molten borosilicate glass, is not reported in the literature. The objective of the present work is to understand the interaction of aluminized and oxidized Alloy 690 specimens with simulated nuclear waste solution and sodium borosilicate melt through characterization of specimen surface and exposed glass using various techniques like Raman spectroscopy, X-ray photoelectron spectroscopy (XPS) and Fourier transform infrared (FT-IR) spectroscopy.

## **Chapter 2**

Ni-based superalloys are being used as furnace materials in nuclear waste immobilization plants across the world. This chapter provides a brief account of literature review related to the present topic that is on interaction of materials with glass melts and acidic environments at elevated temperatures. In particular, review of interaction of materials with borosilicate glass by using different techniques. Importance of borosilicate glass as candidate matrix for immobilization of HLW, structural aspects of borosilicate

glass and effect of incorporation of foreign elements in glass network structure are also reviewed.

### **Chapter 3**

This chapter deals with the experimental techniques and methods employed for interaction of aluminized and thermally oxidized Alloy 690 specimens in simulated nuclear waste solution and sodium borosilicate melt. Various techniques were used for characterization of specimens exposed to simulated nuclear waste solution and sodium borosilicate melt during this study. Techniques include Raman spectroscopy, X-ray photoelectron spectroscopy (XPS), Electron probe microanalyzer (EPMA), Scanning electron microscopy (SEM), Energy dispersive X-ray spectroscopy (EDS). The exposed sodium borosilicate glass has been characterized using Fourier transform infrared (FT-IR) spectroscopy, Raman spectroscopy and XPS. A brief account of working principle and characteristics of these techniques are presented in this chapter.

### **Chapter 4**

This chapter deals with interaction of pack aluminized (high Al-containing pack; 10 wt.% Al) and thermally oxidized Alloy 690 specimens with simulated nuclear waste solution at 373 K for 216 hours and sodium borosilicate melt at 1248 K for 192 hours. The exposed specimens were characterized by using Raman spectroscopy, XPS and EPMA techniques. Bare Alloy 690 substrates were also exposed to similar environments.

For aluminized and thermally oxidized sample exposed to simulated nuclear waste (373 K), micro-Raman spectroscopy revealed the presence of  $\text{Al}_2\text{O}_3$ , mixed oxides of  $\text{NiCr}_2\text{O}_4$  and  $\text{NiFe}_2\text{O}_4$ ,  $\text{NiO}$ , a small amount of  $\text{Cr}_2\text{O}_3$  and mixture of  $\text{Cr}^{+3}$  and  $\text{Cr}^{+6}$  oxides. Using the same technique, similar surface compositions were noticed for coated samples exposed to sodium borosilicate melt (1248 K). XPS analysis of aluminized and thermally oxidized sample exposed to simulated nuclear waste and sodium borosilicate melt showed

the presence of  $\text{Al}_2\text{O}_3$ ,  $\text{NiO}$  and elemental aluminium ( $\text{Al}^0$ ).  $\text{Al}2p$  and  $\text{O}1s$  XPS spectra of coated samples exposed to simulated nuclear waste are shown in Fig. 1. Back-scattered electron (BSE) image of the surface of coated samples exposed to simulated nuclear waste reveals a two phase structure, a whitish phase and a dark phase as shown in Fig. 2a. Qualitative Wavelength dispersive spectroscopy (WDS) analysis along with X-ray mapping revealed the homogeneous distribution of aluminium over the dark phase and distribution of nickel, chromium and iron on the whitish phase. This observation is in accordance with the findings by Raman spectroscopy and XPS studies. For coated samples exposed to sodium borosilicate melt, BSE image as demonstrated in Fig. 2b, shows continuous microstructure. Qualitative WDS analysis and X-ray imaging studies reveal that, the surface of the exposed specimen is enriched with aluminium along with small amounts of nickel, chromium and iron. This is also in agreement with the results of Raman spectroscopy and XPS analysis. The mixed oxides on coated samples are believed to have formed due to prior oxidation treatment.

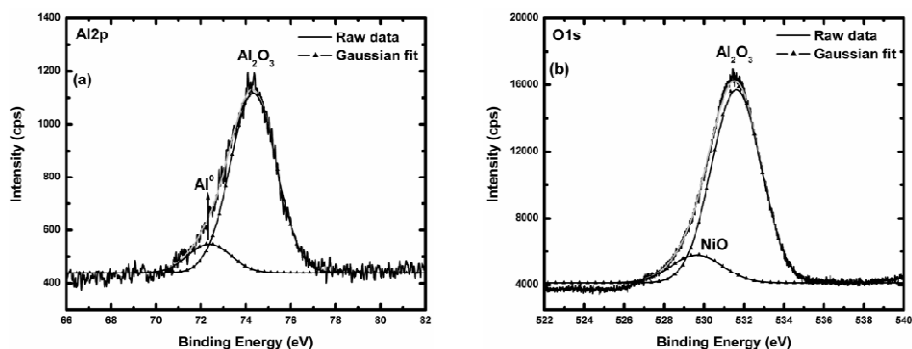


*Fig. 1. (a)  $\text{Al}2p$  and (b)  $\text{O}1s$  XPS spectra of aluminized and thermally oxidized*

*Alloy 690 substrate that exposed to simulated nuclear waste*

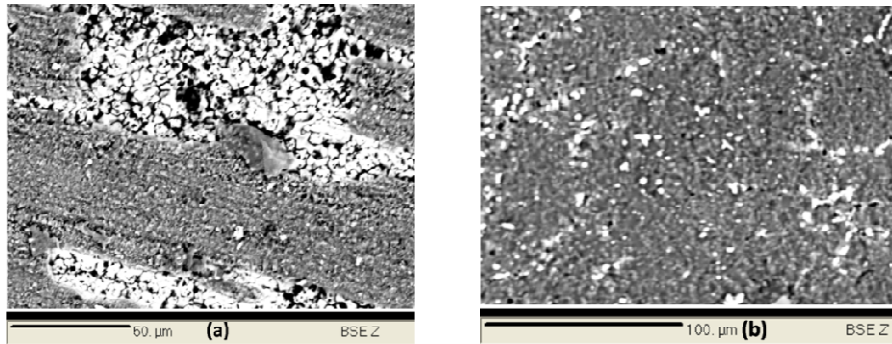


*Fig. 2. Back-scattered electron micrographs of aluminized and thermally oxidized Alloy 690 specimen exposed to (a) simulated nuclear waste and (b) sodium borosilicate melt*

For Alloy 690 substrate exposed to simulated nuclear waste, Raman spectroscopy indicated the presence of  $\gamma$ -Fe<sub>2</sub>O<sub>3</sub>, NiO, a small amount of Cr<sub>2</sub>O<sub>3</sub> and mixture of Cr<sup>+3</sup> and Cr<sup>+6</sup> oxides. The substrate exposed to sodium borosilicate melt revealed similar compositions along with presence of mixed oxides of NiCr<sub>2</sub>O<sub>4</sub> and NiFe<sub>2</sub>O<sub>4</sub>. The presence of mixed oxides on substrate exposed to molten glass could be due to high temperature (1248 K) exposure. XPS analysis of Alloy 690 substrate exposed to simulated nuclear waste solution showed the presence of Cr<sub>2</sub>O<sub>3</sub>, elemental chromium, NiO and elemental nickel, while the presence of Cr<sub>2</sub>O<sub>3</sub> and CrO<sub>3</sub> were found for the sample exposed to borosilicate melt. The difference in surface compositions indicated between Raman spectroscopy and XPS could be attributed to depth sensitivity of the two techniques. Microscopic analysis of Alloy 690 substrate that exposed to sodium borosilicate melt, using Back-scattered electron (BSE) image analysis indicated the two phase microstructure, a whitish phase and dark phase. Qualitative WDS analysis revealed that, the whitish phase is enriched with nickel along with small amount of iron and the dark phase is composed of chromium. These findings support the results obtained by Raman spectroscopy and XPS studies.

## Chapter 5

Chapter 5 discusses the results of interaction studies of pack aluminized (low Al-containing pack; 2 wt.% Al) and thermally oxidized Alloy 690 substrates with simulated nuclear waste solution at 373 K for 216 hours and sodium borosilicate melt at 1248 K for 192 hours. The interacted specimens were characterized by using Raman spectroscopy, XPS and Scanning electron microscopy (SEM) with Energy dispersive X-ray spectroscopy (EDS).

Raman spectroscopy reveals the presence of  $\text{Al}_2\text{O}_3$ ,  $\text{NiFe}_2\text{O}_4$  mixed oxide,  $\text{Cr}_2\text{O}_3$  and mixture of  $\text{Cr}^{+3}$  and  $\text{Cr}^{+6}$  oxides on aluminized and thermally oxidized Alloy 690 specimen surface after interaction with simulated nuclear waste solution and sodium borosilicate melt. X-ray photoelectron spectroscopy analysis has shown that the coated specimens interacted with simulated nuclear waste contain  $\text{Al}_2\text{O}_3$  and  $\text{Cr}_2\text{O}_3$  on the surface, whereas coated specimen exposed in sodium borosilicate melt has indicated the presence of NiO along with  $\text{Al}_2\text{O}_3$ . O1s XPS spectrum of aluminized and oxidized Alloy 690 specimen exposed to simulated nuclear waste and sodium borosilicate melt are given in Fig. 3a and 3b respectively. Microstructural analysis of coated samples exposed in simulated nuclear waste solution indicated the presence of continuous, pore-free spherical particles of nanosize (~ 200 nm) even after prolonged exposure. Quantitative EDS analysis has shown that the surface of the specimen contains mainly  $\text{Al}_2\text{O}_3$  along with small amounts of nickel, chromium and iron. X-ray mapping on the surface of exposed specimen confirmed the EDS analysis results. Uniform distribution of aluminium and oxygen and inhomogeneous distribution of nickel, chromium and iron are observed in  $\text{AlK}\alpha$ ,  $\text{OK}\alpha$ ,  $\text{NiK}\alpha$ ,  $\text{CrK}\alpha$  and  $\text{FeK}\alpha$  X-ray images. Almost homogeneous microstructure obtained for aluminized and thermally oxidized Alloy 690 substrate exposed to sodium borosilicate melt. Quantitative EDS analysis along with X-ray mapping indicated that,

aluminium, oxygen, nickel and chromium are almost uniformly dispersed on the surface and small amount of iron is concentrated in some regions. Secondary electron (SE) micrographs of coated samples exposed to simulated nuclear waste and sodium borosilicate melt are illustrated in Fig. 4a and 4b respectively. The existence of  $\text{Al}_2\text{O}_3$  phase along with  $\text{Cr}_2\text{O}_3$ ,  $\text{NiFe}_2\text{O}_4$  and mixed oxides of  $\text{Cr}^{+3}$  and  $\text{Cr}^{+6}$  on the surface of the coated specimen even after prolonged exposure in simulated nuclear waste and sodium borosilicate melt indicated the good stability of aluminide coatings, which is having  $\text{Al}_2\text{O}_3$  layer on top surface.

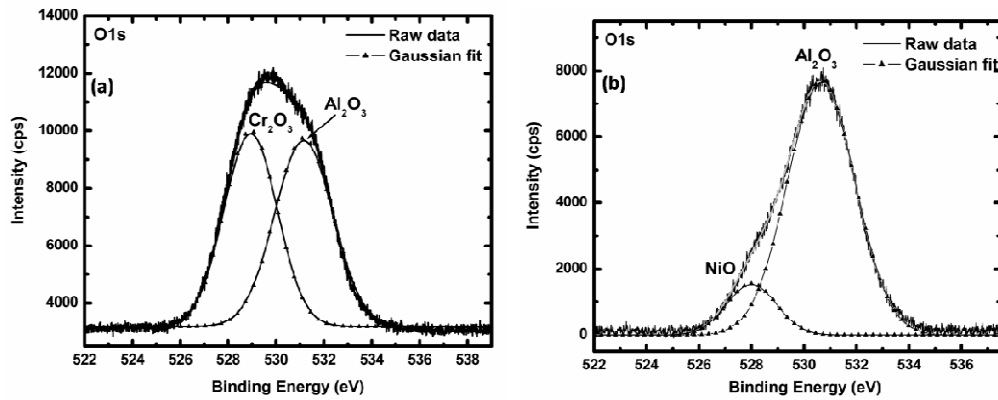


Fig. 3.  $\text{O}1s$  XPS spectrum of aluminized and oxidized Alloy 690 specimen exposed to (a) simulated nuclear waste and (b) sodium borosilicate melt

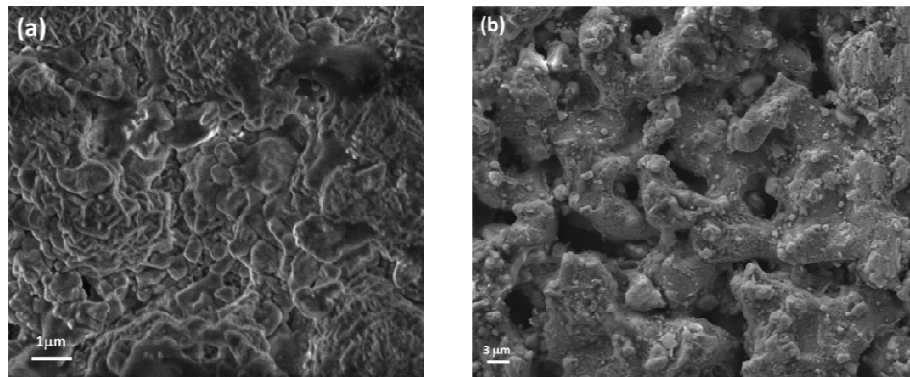
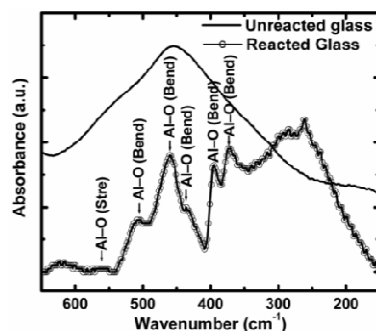


Fig. 4. Secondary electron micrographs of aluminized and thermally oxidized Alloy 690 specimens exposed to (a) simulated nuclear waste and (b) sodium borosilicate melt

## Chapter 6

In Chapter 4 and 5, it has been discussed about the interaction of aluminide coated Alloy 690 specimens in different environments and surface characterization using various techniques. In chapter 6, the characterization of sodium borosilicate glass that interacted with aluminized and thermally oxidized Alloy 690 substrates has been addressed. FT-IR spectroscopy, Raman spectroscopy and XPS were used for characterization of reacted glass samples.

The observed bands in mid-infrared spectra of sodium borosilicate glass that is exposed to aluminide coated samples having high aluminum content correspond to the vibrational bands of specific groups. These mid-infrared bands are strong and broad and overlaps on the weak Al—O bands. In far-infrared region, there are distinct spectral features of Longitudinal Optical (LO) and Transverse Optical (TO) stretching and bending Al—O vibrations. Far-infrared spectrum of exposed sodium borosilicate glass is given in Fig. 5. In X-ray photoelectron spectra of O1s region of reacted glass, non-bridging oxygen component disappeared due to incorporation of aluminium in the glass structure. Chemical shift towards higher energy side in B1s photoelectron spectra of reacted glass indicated the modified glass structure in consequence of inclusion of  $\text{Al}^{+3}$  in glass network.



*Fig. 5. Far-infrared absorption spectra of sodium borosilicate glass that interacted with aluminized + thermally oxidized Alloy 690 substrate (with high Al content) and unreacted glass*

Micro-Raman spectra of sodium borosilicate glass, which interacted with aluminized and thermally oxidized Alloy 690 substrate having low aluminium content, and unreacted glass is presented in Fig. 6. Four broad peaks were observed in Raman spectra of both reacted and unreacted glasses. No additional bands were observed in Raman spectra of sodium borosilicate glass. XPS survey of sodium borosilicate glass shows similar spectra for both reacted and unreacted glass. O1s, Si2p and B1s XPS spectra of reacted and unreacted sodium borosilicate glass have shown the binding energy peaks at similar positions. This indicates that, there is no structural modification of glass network after prolonged exposure with aluminized and thermally oxidized Alloy 690 substrate having low aluminium content at elevated temperature.

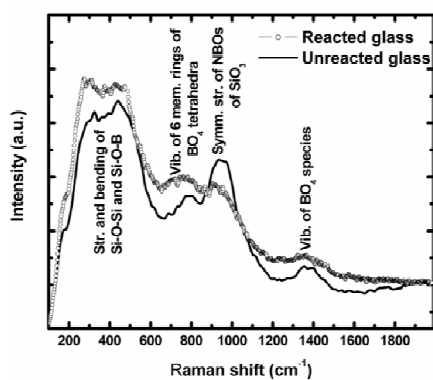


*Fig. 6. Raman spectra of sodium borosilicate glass that interacted with aluminized + thermally oxidized Alloy 690 substrate (with low Al content) and unreacted glass*

## Chapter 7

This chapter discusses the summary of the present work and also the scope for the future work. In the present work, aluminized (using high/low Al-containing pack) and thermally oxidized Alloy 690 substrates and bare specimens have been exposed to simulated nuclear waste solution and sodium borosilicate melt. Important findings are summarized below:

- Surface of aluminized (using high Al-containing pack) and thermally oxidized Alloy 690 specimen exposed to simulated nuclear waste solution consists of  $\text{Al}_2\text{O}_3$ ,  $\text{NiCr}_2\text{O}_4$  and  $\text{NiFe}_2\text{O}_4$  mixed oxides,  $\text{NiO}$ ,  $\text{Cr}_2\text{O}_3$ , mixture of  $\text{Cr}^{+3}$  and  $\text{Cr}^{+6}$  oxides and elemental aluminium. Similar surface compositions were noticed for coated samples exposed to sodium borosilicate melt.
- Aluminized (using low Al-containing pack) and thermally oxidized Alloy 690 specimen exposed to simulated nuclear waste solution contains of  $\text{Al}_2\text{O}_3$ ,  $\text{NiFe}_2\text{O}_4$  mixed oxide,  $\text{Cr}_2\text{O}_3$  and mixture of  $\text{Cr}^{+3}$  and  $\text{Cr}^{+6}$  oxides. Whereas coated specimens exposed to sodium borosilicate melt reveal similar surface compositions along with the presence of  $\text{NiO}$ .
- The surface composition of coated specimen exposed to simulated nuclear waste solution is similar to that exposed in sodium borosilicate melt. This could be attributed to the unaltered mixed oxides that were formed on the surface of the specimens during pre-oxidation treatment.
- For Alloy 690 bare substrates exposed to simulated nuclear waste solution, Raman spectroscopy indicated the presence of  $\gamma\text{-Fe}_2\text{O}_3$ ,  $\text{NiO}$ , some amount of  $\text{Cr}_2\text{O}_3$ , mixture of  $\text{Cr}^{+3}$  and  $\text{Cr}^{+6}$  oxides and elemental nickel and chromium, whereas bare substrate exposed to borosilicate melt reveal similar composition along with the presence of thick  $\text{Cr}_2\text{O}_3$  layer, mixed oxides of  $\text{NiCr}_2\text{O}_4$  and  $\text{NiFe}_2\text{O}_4$ . The presence of mixed oxides for substrate exposed in molten glass is due to high temperature (1248 K) exposure.
- Sodium borosilicate glass that was exposed to aluminized and oxidized Alloy 690 specimen with high aluminium content indicated modified glass structure due to incorporation of  $\text{Al}^{+3}$  in the glass network. On the other hand, glass

exposed with coated specimens with low aluminium content indicated no structural modification of the glass network after the prolonged exposure.

### **Scope for future work**

The present work can be extended by studying the interaction of different aluminide coated Ni–Cr-containing, Fe–Ni–Cr containing superalloys in corrosive environments pertinent to high temperature applications.

## References

- [1] M.A. Audero, A.M. Bevilacqua, N.B.M. de Bernasconi, D.O. Russo, M.E. Sterba, *J. Nucl. Mater.* 223 (1995) 151.
- [2] C.P. Kaushik, R.K. Mishra, P. Sengupta, Amar Kumar, D. Das, G.B. Kale, Kanwar Raj, *J. Nucl. Mater.* 358 (2006) 129.
- [3] K. Raj, K.K. Prasad, N.K. Bansal, *Nucl. Eng. Des.* 236 (2006) 914.
- [4] Pranesh Sengupta, Detlef Rogalla, Hans Werner Becker, Gautam Kumar Dey, Sumit Chakraborty, *J. Hazard. Mater.* 192 (2011) 208.
- [5] J.Di Martino, C. Rapin, P. Berthod, R. Podor, P. Steinmetz, *Corros. Sci.* 46 (2004) 1849.
- [6] J.Di Martino, C. Rapin, P. Berthod, R. Podor, P. Steinmetz, *Corros. Sci.* 46 (2004) 1865.
- [7] A. Carton, C. Rapin, R. Podor, P. Berthod, *J. Electrochem. Soc.* 153 (2006) 121.
- [8] C. Rapin, M. Vilasi, R. Podor, A. carton, B. Gaillard-Allemand, P. Berthod, P. Steinmetz, *Mater. Sci. Forum* 461-464 (2004) 1125.
- [9] H. Khedim, S. Abdelouhab, R. Podor, C. Rapin, M. Vilasi, P.-J. Panteix, M. Toplis, F. Faure, *J. Non-Cryst. Solids* 357 (2011) 31.
- [10] S. Abdelouhab, C. Rapin, R. Podor, P. Berthod, M. Vilasi, *J. Electrochem. Soc.* 154 (2007) 500.
- [11] R.S. Dutta, C. Yusufali, B. Paul, S. Majumdar, P. Sengupta, R.K. Mishra, C.P. Kaushik, R.J. Kshirsagar, U.D. Kulkarni, G.K. Dey, *J. Nucl. Mater.* 432 (2013) 72.
- [12] V. Kain, P. Sengupta, P.K. De, S. Banerjee, *Metall. Mater. Trans. A* 36 A (2005) 1075–1084.

- [13] R.S. Dutta, S. Majumdar, P.K. Limaye, U.D. Kulkarni, G.K. Dey, Trans. IIM 64 (2011) 31.
- [14] R.S. Dutta, C. Yusufali, S. Majumdar, R.K. Mishra, C.P. Kaushik, R.J. Kshirsagar, U.D. Kulkarni, G.K. Dey, Mater. Sci. Forum 710 (2012) 733.

## List of figures

		Page No.
Figure 2.1.	Schematic diagram showing major components of the induction heated metallic melter [36].	11
Figure 2.2.	Schematic diagram of Joule heated ceramic melter showing important components [49].	12
Figure 2.3.	SEM micrograph along the cross-section of aluminized and oxidized Alloy 690 substrate with adhered glass (exposed to sodium borosilicate melt at 1248 K for 192 h) revealing different multilayers without any phase formation at the coating/glass interface [11].	17
Figure 2.4.	Volume–temperature characteristics (schematic) for glassy, liquid and solid states [49]	20
Figure 2.5.	Schematic structures of (a) crystalline and (b) amorphous silica.	22
Figure 2.6.	Schematic structure of silicate glass [36].	24
Figure 2.7.	Schematic structure of nuclear waste glass [36].	25
Figure 3.1.	Schematic diagram of pack aluminization process.	31
Figure 3.2.	Experimental set-up used for exposure of specimens with simulated nuclear waste solution at 373 K for 216 h.	34
Figure 3.3.	Chamber type furnace used for exposure of specimens with sodium borosilicate melts.	36
Figure 3.4.	Sillimanite crucible used in the present study in which specimens along with borosilicate glass has been exposed.	36
Figure 3.5.	Different signals resulting from interaction of the electron beam with specimen.	37

Figure 3.6.	Schematic diagram of a scanning electron microscope.	38
Figure 3.7.	A schematic figure of EPMA.	41
Figure 3.8.	Schematic diagram of Michelson type interferometer.	44
Figure 3.9.	Schematic representation of the (a) Rayleigh, (b) Stokes Raman and (c) anti-Stokes Raman scattering effect.	46
Figure 3.10.	Schematic diagram of X-ray photoelectron spectroscopy.	49
Figure 4.1.	SEM micrograph showing the cross-sectional view of aluminized (using high Al-containing pack) and thermally oxidized Alloy 690 specimen.	55
Figure 4.2.	Surface image (BSE) of aluminized (using high Al-containing pack) and thermally oxidized Alloy 690 specimen.	55
Figure 4.3	Normalized Raman spectra of specimens of Set A exposed to simulated nuclear waste solution. Gaussian fit of the region 600–720 $\text{cm}^{-1}$ is shown in inset.	57
Figure 4.4.	XPS survey spectrum recorded on the surface of specimens of Set A exposed to simulated high level nuclear waste solution.	58
Figure 4.5.	XPS spectra recorded on the surface of specimens of Set A exposed to simulated high level nuclear waste, (a) Al2p spectrum reveals the presence of elemental aluminium and $\text{Al}_2\text{O}_3$ , (b) O1s spectrum showing NiO and $\text{Al}_2\text{O}_3$ .	58
Figure 4.6.	Representative back-scattered electron (BSE) image of specimens of Set A exposed to simulated nuclear waste solution.	59
Figure 4.7.	X-ray spectra (Lithium fluoride crystal, LiF) showing the variations in Ni, Cr and Fe X-ray intensities on the surface of specimens of Set A exposed to simulated nuclear waste solution	59

- (a) whitish phase and (b) dark phase.
- Figure 4.8. X-ray spectra (Thallium acid phthalate crystal, TAP) showing  $AlK\alpha$  X-ray intensities on the surface of specimens of Set A exposed to simulated nuclear waste solution (a) whitish phase and (b) dark phase. 60
- Figure 4.9. X-Ray images for (a)  $NiK\alpha$ , (b)  $CrK\alpha$ , (c)  $FeK\alpha$  and (d)  $AlK\alpha$  of surface of specimens of Set A exposed to simulated nuclear waste solution revealing the distribution of different elements. 61
- Figure 4.10. Normalized Raman spectra of specimens of Set B exposed to sodium borosilicate melt. 62
- Figure 4.11. XPS survey spectrum recorded on the surface of specimens of Set B exposed to sodium borosilicate melt. 63
- Figure 4.12. XPS spectra recorded on the surface of specimens of Set B exposed to sodium borosilicate melt, (a)  $Al2p$  spectrum showing elemental aluminium and  $Al_2O_3$  and (b)  $O1s$  spectrum reveals  $NiO$  and  $Al_2O_3$  and (c)  $Ni2p$  spectrum showing  $NiO$ . 63
- Figure 4.13. Representative back-scattered electron (BSE) image of specimens of Set B exposed to sodium borosilicate melt. 64
- Figure 4.14. X-ray spectra (LiF & TAP crystal) showing Ni, Cr, Fe and Al X-ray peaks on the surface of specimens of Set B exposed to sodium borosilicate melt. It reveals the enrichment of Al and depletion of Cr on the surface. 64
- Figure 4.15. X-Ray images for (a)  $NiK\alpha$ , (b)  $CrK\alpha$ , (c)  $FeK\alpha$  and (d)  $AlK\alpha$  of surface of specimens of Set B exposed to sodium borosilicate melt revealing the distribution of different elements. 65

Figure 4.16.	Normalized Raman spectra of Alloy 690 bare substrate exposed to simulated nuclear waste solution.	66
Figure 4.17.	XPS survey spectrum recorded on the surface of Alloy 690 bare substrate exposed to simulated high level nuclear waste solution.	67
Figure 4.18.	XPS spectra recorded on the surface of Alloy 690 bare substrate exposed to simulated nuclear waste solution, (a) Ni2p spectrum, presence of Ni <sup>0</sup> and NiO are visible,(b) Cr2p spectrum, reveals elemental chromium and Cr <sub>2</sub> O <sub>3</sub> and (c) O1s spectrum shows Cr <sub>2</sub> O <sub>3</sub> and NiO.	68
Figure 4.19.	X-ray spectrum (LiF crystal) showing the characteristic Ni, Cr and Fe X-ray peaks on the surface of Alloy 690 bare substrate exposed to simulated nuclear waste solution.	69
Figure 4.20.	Normalized Raman spectra of bare Alloy 690 bare substrate exposed to sodium borosilicate melt.	70
Figure 4.21.	XPS survey spectrum recorded on the surface of Alloy 690 bare substrate exposed to sodium borosilicate melt.	70
Figure 4.22.	XPS spectra recorded on the surface of Alloy 690 bare substrate exposed to sodium borosilicate melt, (a) Cr2p spectrum, Cr <sub>2</sub> O <sub>3</sub> and CrO <sub>3</sub> are visible and (b) O1s spectrum reveals Cr-oxide.	71
Figure 4.23.	Representative back-scattered electron (BSE) image of Alloy 690 bare substrate exposed to sodium borosilicate melt showing a whitish phase and dark phase.	71
Figure 4.24.	X-ray spectra (LiF crystal) showing the variations in Ni, Cr and Fe X-ray intensities on the surface of Alloy 690 bare substrate exposed to sodium borosilicate melt (a) whitish phase and (b)	72

	dark phase.	
Figure 4.25	X-Ray images for (a) NiK $\alpha$ , (b) CrK $\alpha$ and (c) FeK $\alpha$ of surface of Alloy 690 bare substrate that exposed to sodium borosilicate melt revealing the distribution of different elements.	73
Figure 4.26.	Schematic representation of interaction of Alloy 690 bare substrate with sodium borosilicate melts.	78
Figure 4.27.	Schematic representation of interaction of aluminized (high Al containing pack) and oxidized Alloy 690 specimen with sodium borosilicate melts.	78
Figure 5.1(a).	Aluminized (using low Al-containing pack) and thermally oxidized Alloy 690 specimen revealing Cr-rich layer, (NiCr) <sub>2</sub> Al, (NiCr) Al type aluminides and NiAl layer along the cross-section.	88
Figure 5.1(b).	EDS line scan along the cross-section of Aluminized (using low Al-containing pack) and thermally oxidized Alloy 690 specimen revealing Al <sub>2</sub> O <sub>3</sub> on the uppermost surface.	88
Figure 5.1(c).	Surface image (BSE) of aluminized (using low Al-containing pack) and thermally oxidized Alloy 690 specimen.	89
Figure 5.2.	Normalized Raman spectrum of a specimen from Set C after exposure to simulated nuclear waste solution.	89
Figure 5.3.	XPS survey spectrum recorded on a specimen from Set C after exposure to simulated high level nuclear waste solution.	90
Figure 5.4.	XPS spectra recorded on the surface of a specimen from Set C after exposure to simulated high level nuclear waste solution (a) Al <sub>2</sub> p spectrum showing Al <sub>2</sub> O <sub>3</sub> and native oxide of Al, (b) Cr <sub>2</sub> p	91

	spectrum, reveals $\text{Cr}_2\text{O}_3$ and (c) O1s spectrum shows $\text{Cr}_2\text{O}_3$ and $\text{Al}_2\text{O}_3$ .	
Figure 5.5.	Secondary electron micrograph of the of a specimen from Set C exposed to simulated nuclear waste revealing pore-free uniform microstructure.	92
Figure 5.6.	EDS spectra recorded on different locations of a specimen from Set C exposed to simulated nuclear waste solution.	93
Figure 5.7.	X-Ray images for (a) $\text{AlK}\alpha$ , (b) $\text{OK}\alpha$ , (c) $\text{NiK}\alpha$ , (d) $\text{CrK}\alpha$ and (e) $\text{FeK}\alpha$ of a specimen from set C that was exposed to simulated nuclear waste solution revealing the distribution of various elements.	94
Figure 5.8.	Normalized Raman spectrum of a specimen from Set D after exposure to sodium borosilicate melt.	95
Figure 5.9.	XPS survey spectrum recorded on the surface of a specimen from Set D exposed to sodium borosilicate melt.	96
Figure 5.10.	XPS spectra recorded on the surface of a specimen from Set D exposed to sodium borosilicate melt, (a) $\text{Al}2\text{p}$ spectrum showing $\text{Al}_2\text{O}_3$ and native oxide of Al and (b) O1s spectrum reveals NiO and $\text{Al}_2\text{O}_3$ .	96
Figure 5.11.	Secondary electron micrograph of a specimen from Set D that was exposed to sodium borosilicate melt revealing fairly homogeneous microstructure after prolonged exposure.	97
Figure 5.12.	EDS spectra recorded on different locations of a specimen from Set D exposed to sodium borosilicate melt.	98
Figure 5.13.	X-Ray images for (a) $\text{AlK}\alpha$ , (b) $\text{OK}\alpha$ , (c) $\text{NiK}\alpha$ , (d) $\text{CrK}\alpha$ and (e)	99

FeK $\alpha$  on s specimen from Set D that was exposed to sodium borosilicate melt revealing the distribution of various elements.

- Figure 6.1. Mid-infrared absorption spectrum of sodium borosilicate glass 108  
interacted with aluminized (with high Al containing pack) and thermally oxidized Alloy 690 specimen indicating different structural silicate and borate chains. Spectrum of unreacted glass is also shown for comparison.
- Figure 6.2. Far-infrared absorption spectrum of sodium borosilicate glass 109  
interacted with aluminized (with high Al containing pack) and thermally oxidized Alloy 690 specimen showing distinct spectral features of Al–O stretching and bending vibration bands. Spectrum of unreacted glass is also shown.
- Figure 6.3. XPS survey spectra of (a) sodium borosilicate glass that 110  
interacted with aluminized (with high Al containing pack) and thermally oxidized Alloy 690 specimen and (b) unreacted sodium borosilicate glass.
- Figure 6.4. O1s photoelectron spectrum of (a) unreacted sodium borosilicate 110  
glass and (b) glass interacted with aluminized (with high Al containing pack) and thermally oxidized Alloy 690 specimen. Non-bridging oxygen (NBO) component has disappeared from spectrum of reacted glass due to incorporation of Al<sup>+3</sup> in the glass structure.
- Figure 6.5. B1s photoelectron spectrum of (a) unreacted sodium borosilicate 111  
glass and (b) glass interacted with aluminized (with high Al containing pack) and thermally oxidized Alloy 690 specimen.

Chemical shift towards higher energy side in reacted glass is due to decrease in electron density on boron atom after conversion of trigonal boron to tetrahedral boron.

- Figure 6.6. Micro-Raman spectra of sodium borosilicate glass interacted with aluminized (with low Al containing pack) and thermally oxidized Alloy 690 specimen indicating different structural silicate and borate units. Spectra of unreacted glass are also shown. 112
- Figure 6.7. XPS survey spectra of (a) sodium borosilicate glass that interacted with aluminized (with low Al containing pack) and thermally oxidized Alloy 690 specimen and (b) unreacted sodium borosilicate glass. 113
- Figure 6.8. O1s XPS spectra of (a) unreacted sodium borosilicate glass and that of (b) sodium borosilicate glass that reacted with aluminized (with low Al containing pack) and thermally oxidized Alloy 690 substrate, showing the peaks of NBO and BO. 114
- Figure 6.9. Si2p XPS spectra of (a) unreacted sodium borosilicate glass and that of (b) sodium borosilicate glass that reacted with aluminized (with low Al containing pack) and thermally oxidized Alloy 690 substrate. 114
- Figure 6.10. B1s XPS spectra of (a) unreacted sodium borosilicate glass and that of (b) sodium borosilicate glass that reacted with aluminized (with low Al containing pack) and thermally oxidized Alloy 690 substrate. 115
- Figure. 6.11. Pictorial representation of modified sodium borosilicate glass 119

structure due to incorporation of  $Al^{3+}$  from high Al containing coating.

## List of tables

	Page No.
Table-3.1. Chemical composition of superalloy 690 (wt.%).	31
Table-3.2. Chemical composition of simulated nuclear high level waste solution used.	33
Table-3.3(a). Composition of oxides in sodium borosilicate glass used.	35
Table-3.3(b). Concentration of elements in borosilicate glass used.	36
Table-4.1. Summary of results.	74
Table-4.2. Details of Raman spectroscopy results and their peak assignments.	76
Table-4.3. Details of XPS peaks and their assignments.	80
Table-5.1. Different aluminides formed on Alloy 690 specimen in high Al and low Al containing coatings.	87
Table-5.2. Compositional EDS analysis results from different locations of a specimen from Set C exposed to simulated nuclear waste solution.	92
Table-5.3. Compositional EDS analysis results from different locations on a specimen from Set D that was exposed to sodium borosilicate melt.	97
Table-5.4. Details of Raman spectroscopy results and their peak assignments.	101
Table-5.5. Details of XPS peaks and their assignments.	101
Table-6.1. Composition of glass constituent elements after interaction with coated alloy.	107
Table-6.2. Details of FTIR peaks and their assignments.	117



## *Introduction*

---

### **1.1 Background**

Management of high level radioactive liquid waste (HLW) produced during the reprocessing of irradiated nuclear fuel is a challenging activity faced by nuclear industry. Vitrification of HLW in borosilicate glass is considered to be one of the most acceptable immobilization methods available today [1,2]. Out of various types of vitrification processes, processes based on induction heated metallic melter pot method and Joule heated ceramic melter pot method are widely followed at the Waste Immobilization plant scale [3,4]. The majority of the alloys and superalloys in contact with molten glasses that are used in the glass industry contain upto 30 wt% chromium. Upon exposure to molten glass, these alloys develop a chromia ( $\text{Cr}_2\text{O}_3$ ) layer at the metal/glass interface and the chromia layer exhibits low solubility in molten glass even at elevated temperature. Below the depassivation temperature and glass compositions with lower basicity, the chromia layer passivates the alloys and leads to low corrosion rates [5-10]. Therefore, Ni-based superalloys having about 30% of chromium are generally used as process pot, susceptor in multi-zone induction heated metallic melter pot furnace and the electrodes in Joule heated ceramic melter pot [3,11]. However, because of depletion of Cr adjacent to  $\text{Cr}_2\text{O}_3$  layer in Alloy 690 surfaces and flaking off thick Cr-oxide layer due to development of compressive stress, leaching out of Cr from the alloy takes place [11,12]. To increase the service life of vitrification furnace

materials, efforts are being made to develop suitable coatings on superalloy substrates [11,13,14]. However, detailed interaction of aluminide coatings with simulated waste solution and borosilicate melt has not been studied so far. Keeping this in view, aluminized and oxidized Alloy 690 specimens have been exposed to simulated nuclear waste solution (nitrate-based environment) at 373 K for 216 hours and sodium borosilicate melt at 1248 K for 192 hours. This is followed by characterization of exposed specimens using various techniques such as, Raman spectroscopy, X-ray photoelectron spectroscopy (XPS), electron probe microanalyzer (EPMA) and scanning electron microscopy (SEM) with energy dispersive X-ray spectroscopy (EDS). In addition, exposed sodium borosilicate glass has been characterized using Fourier transform infrared (FT-IR) spectroscopy, Raman spectroscopy, and XPS. Characterization of sodium borosilicate glass that interacted with aluminized specimens prepared from high aluminium containing pack (10 wt.% Al) indicated incorporation of  $Al^{3+}$  in glass network. The studies have also been carried out with specimens having low Al content (2 wt.% Al) to observe its effect on  $Al^{3+}$  incorporation in the glass network. The results of all the interaction studies have been discussed in detail in this thesis comprising seven chapters.

## **1.2 Scope of the thesis**

The present study is mainly focused on the interaction of aluminized and thermally oxidized Alloy 690 substrate with simulated nuclear waste solution and sodium borosilicate melt. The exposed specimens in both the media and sodium borosilicate glass that interacted with coated specimens are characterized using various techniques. The primary objectives for the present study are as follows:

- (a) To understand the interaction of aluminized (high Al-containing pack; 10 wt.% Al) and thermally oxidized Alloy 690 specimens with simulated nuclear waste solution at 373 K for 216 hours and sodium borosilicate melt at 1248 K for 192 hours.
- (b) To study the interaction of pack aluminized (low Al-containing pack; 2 wt.% Al) and thermally oxidized Alloy 690 substrates with simulated nuclear waste solution at 373 K for 216 hours and sodium borosilicate melt at 1248 K for 192 hours.
- (c) To characterize the sodium borosilicate glass that interacted with aluminized and thermally oxidized Alloy 690 substrates using various techniques.

### **1.3 Outline of the thesis**

The results of interaction studies have been discussed in detail in this thesis comprising seven chapters. A brief description of each chapter is given below:

Chapter 2: This chapter provides the review of work done by different researchers on interaction of alloy materials with glass melts and acidic environments at elevated temperatures. Importance of borosilicate glass as candidate matrix for immobilization of HLW, structural aspects of borosilicate glass and effect of incorporation of foreign elements in glass network structure are also reviewed in this chapter.

Chapter 3: This chapter deals with the experimental techniques and methods employed for interaction of aluminized and thermally oxidized Alloy 690 specimens in simulated nuclear waste solution and sodium borosilicate melt. Techniques include Raman spectroscopy, X-ray photoelectron spectroscopy (XPS), Electron probe microanalyzer (EPMA), Scanning electron microscopy (SEM), Energy dispersive X-ray spectroscopy (EDS) and Fourier transform infrared (FT-IR)

spectroscopy. A brief account of working principle and characteristics of these techniques are presented in this chapter.

Chapter 4: This chapter deals with interaction of pack aluminized (high Al-containing pack; 10 wt.% Al) and thermally oxidized Alloy 690 specimens with simulated nuclear waste solution at 373 K for 216 hours and sodium borosilicate melt at 1248 K for 192 hours. The exposed specimens were characterized by using Raman spectroscopy, XPS and EPMA techniques. Bare Alloy 690 substrates were also exposed to similar environments.

Chapter 5: This Chapter discusses the results of interaction studies of pack aluminized (low Al-containing pack; 2 wt.% Al) and thermally oxidized Alloy 690 substrates with simulated nuclear waste solution at 373 K for 216 hours and sodium borosilicate melt at 1248 K for 192 hours. The interacted specimens were characterized by using Raman spectroscopy, XPS and Scanning electron microscopy (SEM) with Energy dispersive X-ray spectroscopy (EDS).

Chapter 6: In this chapter, the characterization of sodium borosilicate glass that interacted with aluminized and thermally oxidized Alloy 690 substrates has been addressed. FT-IR spectroscopy, Raman spectroscopy and XPS were used for characterization of reacted glass samples.

Chapter 7: This chapter discusses the summary of the present work and also the scope for the future work.

### *Literature Review*

---

---

This chapter gives a brief account of literature review relevant to the present topic that is on interaction of materials with glass melts and acidic environments at elevated temperatures. This is, in particular, review of interaction of materials with borosilicate glass by using different techniques. Importance of borosilicate glass as candidate matrix for immobilization of HLW, structural aspects of borosilicate glass and effect of incorporation of foreign elements in glass network structure are also reviewed in this chapter.

#### **2.1 Interaction of metals and alloys with molten glasses**

A number of studies have dealt with the aspects related to the corrosion in molten glasses. These can be classified in two categories, (a) those, which are related to glass and soluble species, and (b) those dealing with the contact between glass and a foreign body (metals and alloys) [5,6,15-19]. Amongst these, corrosion of metals and alloys with molten glass requires more attention as they serve as material of construction of furnaces and other equipments in many industries. Molybdenum has been used as the electrode material in the process of electrical melting of glasses [16,20,21]. Corrosion of electrode material is one of the major problems associated with electrical melting of glass, which leads to the contamination of glass melts as well as loss of electrode materials. The corrosion behaviour of molybdenum electrodes in soda-lime glass melts has been studied using electrochemical

techniques [15]. Current potential curves on molybdenum electrode show an active potential region (Mo oxidized to  $\text{Mo}^{\text{III}}$ ) in which the corrosion rate is high and a passive region at more anodic potential (Mo oxidized to  $\text{Mo}^{\text{VI}}$ ) in which the corrosion rate is much lower. It has been assumed that only  $\text{Mo}^{\text{VI}}$  compounds are able to form a protective layer, which hinders the dissolution of molybdenum electrode [15]. Similarly, corrosion studies on combustion-heating tube materials such as molybdenum, molybdenum disilicide and  $\text{SiC}/\text{Al}_2\text{O}_3$  composite in soda-lime-silicate glass at 1838 K showed that all these materials got corroded by oxidation reactions [22]. Corrosion studies on other electrically conductive materials such as Pt, Ni, Co, Fe, W, Mo, Cr, graphite and stannic oxide in molten sodium diborate glass at 1173 K using linear potential sweep method in nitrogen or argon atmosphere have been performed [17]. Pt and Ni are found to act as insoluble electrodes. The order of increase of electrolytic current density (decrease in corrosion resistance) at 3V is  $\text{W} > \text{Fe} \gg \text{Mo} > \text{Co} > \text{Ni} > \text{Cr} \approx \text{graphite} \approx \text{Pt} > \text{stannic oxide}$  [17].

Martino et al. [5] have investigated the corrosion of pure metals Fe, Ni, Co and Cr in molten glass at 1323 K using electrochemical techniques and weight loss measurements. The authors [5] have found that the increase in glass working temperature can induce important changes in the metal behavior in glass corrosion. As an example, these authors have shown that when pure chromium rods are dipped in borosilicate molten glass, there is a modification of corrosion mechanism when the glass temperature is increased. Chromium is found to be more easily corroded metal when immersed in molten glass at temperature 1323 K, in comparison with Ni, Fe and Co. A 25 K decrease of reaction temperature (at 1298 K) leads four times lesser in corrosion rate due to the formation of a thin  $\text{Cr}_2\text{O}_3$  protective layer at the glass/metal interface. In a separate study, the same investigators [6] have performed the

corrosion experiments of cobalt and nickel based superalloys having high chromium content in molten borosilicate glass at 1323 K. They [6] found that active state of the alloy is characterized by fast dissolution of constitutive elements of the alloy in the glass melt.

### **2.1.1 Interaction of chromium alloys with molten silicate glass**

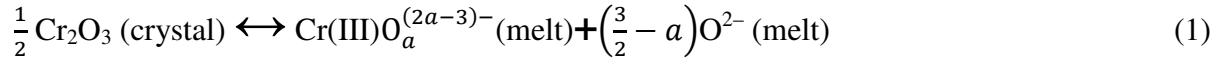
Alloys, which may be resistant to molten glass corrosion must be constituted with high chromium content in order to develop a  $\text{Cr}_2\text{O}_3$  protective layer when they are in contact with the glass [5-7,23,24]. Corrosion studies of pure chromium in four different borosilicate glasses as a function of temperature using scanning electron microscopy and electrochemical methods have revealed that direct immersion of chromium into glass can form a chromia layer at metal/glass interface, if melt temperature is low. This chromia layer is not sufficiently stable to shield the alloys from melt corrosion. When the melt temperature is high, chromium is in active state and reacts with oxidizing species present in the glass [7]. Electrochemical measurements performed at different temperatures also indicate that chromium can be passive up to a limited temperature range. Thermal oxidation of chromium in air atmosphere prior to immersion in molten glass permits the protection of the material from melt corrosion, because of the formation of a continuous  $\text{Cr}_2\text{O}_3$  layer at the metal/glass interface. This shielding is sustained up to the ‘depassivation temperature’, the temperature at which a transition from the passive to active state takes place [7].

The depassivation temperature of pure chromium in binary soda silicate melts ( $\text{Na}_2\text{O}-x\text{SiO}_2$ ) varies with the acidity of the glass. That is higher the glass acidity, higher the depassivation temperature [10]. The passive state domain extension depends on the melt composition and that is mainly governed by the stability of  $\text{Cr}_2\text{O}_3$  layer. Therefore, the protective chromia layer remains more thermally stable as the melt becomes acidic [10].

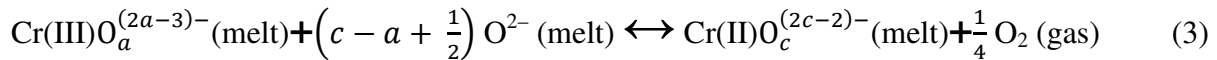
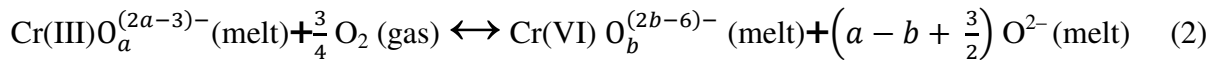
Electrochemical study of pure chromium corrosion and total Cr solubility in soda silicate melts indicate that, lower the total Cr solubility, better the Cr corrosion resistant [25].

### 2.1.2 Interaction of chromium oxide with molten silicate glass

Solubility of chromium oxide strongly depends on glass basicity (melt composition), temperature and oxygen fugacity [26,27]. Oxygen fugacity influences the redox properties of the glass and yields to the stabilization of high or low oxidation states of the multivalent elements in the melt. Therefore, the effects related to the action of both  $O^{2-}$  (basicity effect) and  $O_2$  (redox effect) rule together the chromium chemistry in binary soda–silicate melts [28,29]. These assumptions are also applicable to ternary systems like soda – lime – silicate melts [30]. Various chemical reactions occurring between the silicate melt and chromium oxide are reported in literature [26,28,31].



Under oxidizing conditions, Cr (III) species gets oxidized into Cr (VI) species as given in Eq. (2). Similarly, Cr (III) can be reduced to Cr (II) species under reducing conditions as given in Eq. (3) [31]:



The chromium content variations with melt composition follow the same phenomenon for any values of the temperature:

- Under an oxidizing atmosphere, the solubility of chromium oxide increases with the basicity (alkaline oxide content) of the glass.
- Under a reducing atmosphere, the solubility decreases when the basicity increases.

At the equilibrium stage, the total chromium dissolved in the glass Cr (tot) is measured as the sum of all chromium species:

$$\text{Cr (tot)} = \text{Cr (II)} + \text{Cr (III)} + \text{Cr (VI)}$$

The Cr(III) species dissolved in the melt which is in equilibrium with solid Cr<sub>2</sub>O<sub>3</sub> crystallites, remains steady for any value of oxygen fugacity for a given temperature and melt composition. This statement is convinced by the fact that chromium oxide dissolution (Eq. (1)) is an acid–base reaction which does not depend on oxygen fugacity. The Cr(III) contribution decides the minimum value of the chromium content in the glass. Therefore, the Cr(II) content considered is negligible, compared with Cr(III) and Cr(VI) contents, under oxidizing conditions, Similarly, the Cr(VI) content considered is negligible, compared with Cr (III) and Cr(II) contents, under reducing conditions. With these considerations, the aforementioned equation can be dissociated into the following two equations [31]:

Under oxidizing conditions:

$$\text{Cr (tot)} = \text{Cr (III)} + \text{Cr (VI)}$$

Under reducing conditions:

$$\text{Cr (tot)} = \text{Cr (II)} + \text{Cr (III)}$$

H. Khedim and co-workers [9] have studied the factors controlling the rate at which chromium oxide reaches saturation in Na<sub>2</sub>O–xSiO<sub>2</sub> liquids as a function of melt composition

and oxygen fugacity. They have observed that under an oxidizing atmosphere, depending on the concentration of sodium in the glass melts, liquid  $\text{Na}_2\text{CrO}_4$  or  $\text{Cr}_2\text{O}_3$  crystals are in equilibrium with soda–silicate melts. Under reducing conditions,  $\text{NaCrSi}_2\text{O}_6$  stabilizes in silica rich melts when temperature is lower than 1433 K, while  $\text{Cr}_2\text{O}_3$  is in equilibrium with the sodium–rich melts when temperature is above 1433 K [9].

### **2.1.3 Interaction of nickel-based alloys with molten silicate glass**

Vitrification of HLW is considered to be one of the best available immobilization options today [32-35]. Vitrification processes based on induction heated metallic melter pot method and Joule heated ceramic melter pot method are widely followed at the waste immobilization plant scale [3,4]. The major components of induction heated metallic melter pot are schematically shown in Fig. 2.1. The process pot has three major parts namely, top dish, cell and bottom dish. The cell is made by welding Alloy 690 sheath and it is joined with top and bottom dishes by welding. It is clear from this diagram that the material of construction melter pot and its associated components experience variable modes of degradation along their entire length during vitrification [36,37]. Earlier degradation of melter pot materials, especially components made up of nickel (Ni) based superalloy 690 (e.g. thermowells, feeders, electrodes, pour spout assemblies, metallic process pot, etc.) have been identified as one of the main reasons behind the unexpected shut down of vitrification plant operations [4]. Many experimental studies under partially simulated service conditions in order to understand such failures have been reported by Sengupta and co-workers [37-40].

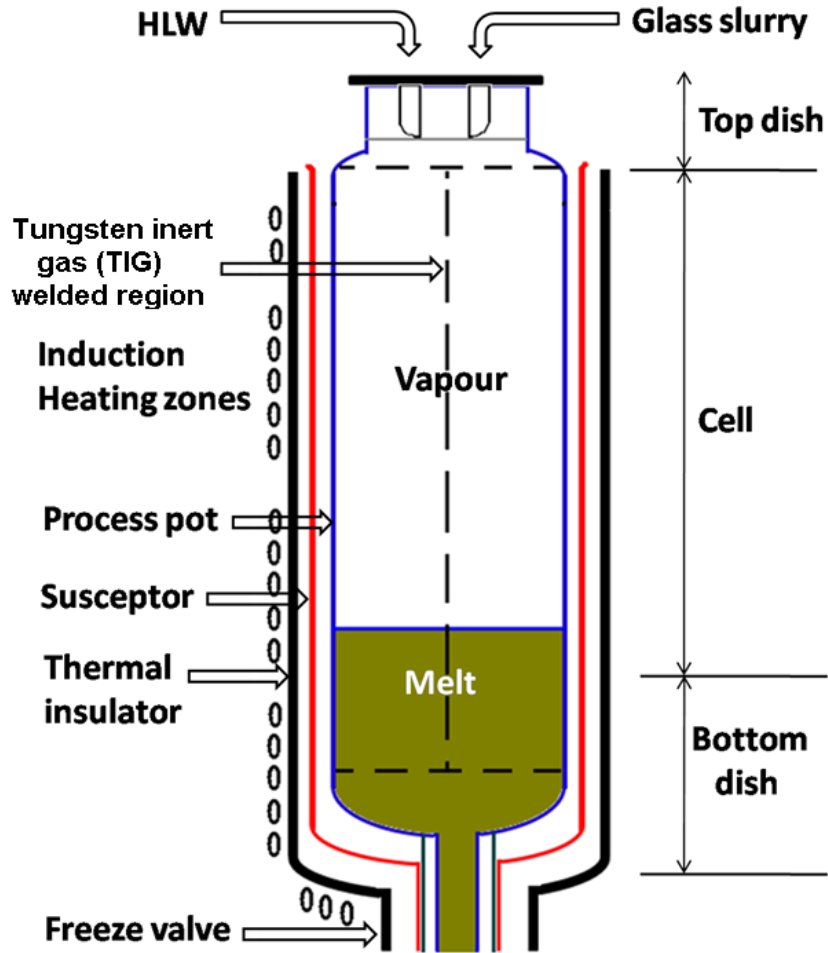


Fig. 2.1. Schematic diagram showing major components of the induction heated metallic melter [36].

The schematic diagram of Joule heated ceramic melter is illustrated in Fig. 2.2. In ceramic melter, electric current across Alloy 690 electrodes that dipped in borosilicate melt is used to produce heat by Joule effect ( $Q = I^2R$ ) which keeps the glass in molten stage and sustains evaporation, calcinations, fusion and soaking. During vitrification process, HLW and glass additives are directly added to the melting chamber and slurries are heated to 1423 K. The durability of the vitrification furnace is basically limited by degradation of metallic components under plant scale service conditions [36].

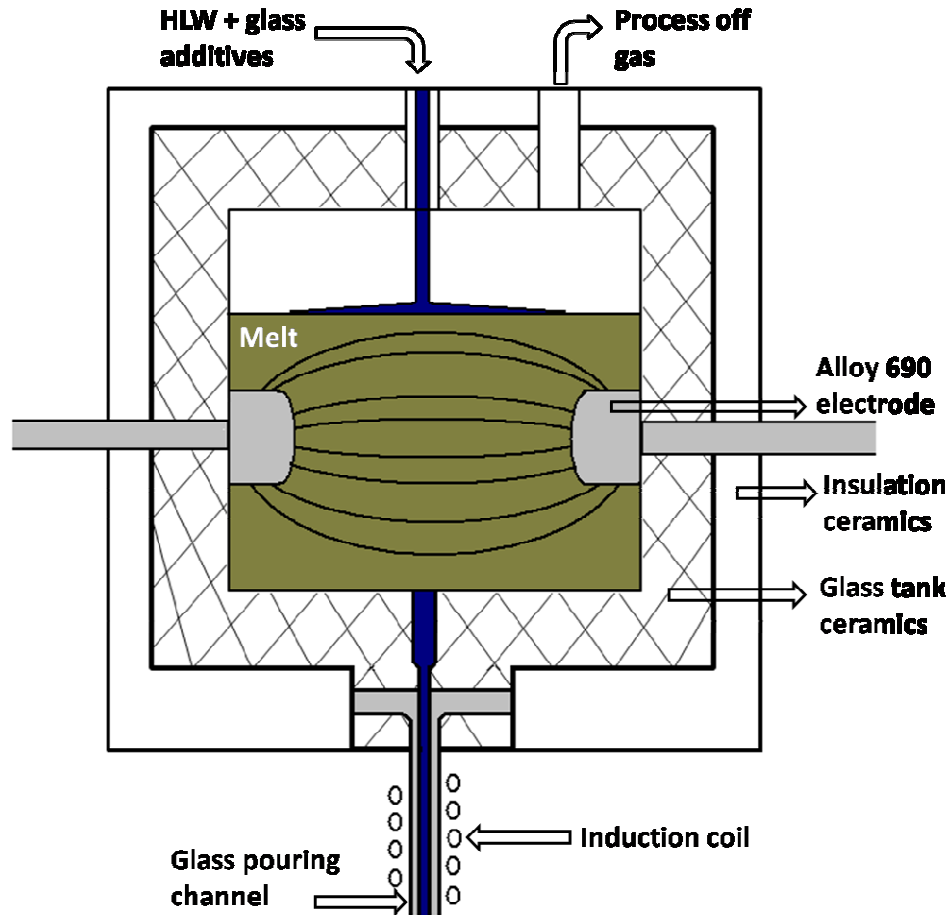


Fig. 2.2. Schematic diagram of Joule heated ceramic melter showing important components

[49].

Interaction of sodium borosilicate waste glass with Alloy 690 coupons at 1223 K at argon atmosphere for time period ranging from 8 h to 96 h has shown interesting physico-chemical changes within glass as well as within Alloy 690 specimen [37]. Ni and Cr diffuse from Alloy 690 to borosilicate melt leads to the development of  $(\text{Fe,Ni})\text{CrO}_4$  needle and  $(\text{Fe,Ni})\text{Cr}_2\text{O}_4$  cubic phases within the melt at borosilicate melt/Alloy 690 interface. Highly dense phases like  $(\text{Fe,Ni})\text{CrO}_4$  and  $(\text{Fe,Ni})\text{Cr}_2\text{O}_4$  are prone to settle down in the melter pot during vitrification and can arise the blockage in freeze valve. Besides the formation of Cr rich phases, enrichment of sodium along with the interface is noted. The local build up of Na

concentration will cause the formation of  $\text{Na}_2\text{SO}_4$  rich clusters especially during the vitrification of sulphate rich HLW. Development of such sulphate rich cluster can causes the sulfur corrosion attack on melter pot materials. Depletion of chromium in Alloy 690 side has been noticed near the interface [37]. Such significant depletion of chromium adjacent to interface is surprising as Cr offers resistance to intragranular and intergranular stress corrosion cracking attacks in Ni-base alloys [41]. Beside this, CrB precipitates have formed along the Alloy 690 grain boundaries. In a separate study [12], reaction between the molten borosilicate glass and Alloy 690 at 1223 K for 24 h in air, has shown the depletion of chromium on the Alloy 690 surface near the reacting interface. A distance of 10  $\mu\text{m}$  has been found to be depleted. On the glass side, there has been depletion of silicon near the reaction interface, enrichment of sodium, and also formation chromium-rich phase at the interface. The chromium content on the alloy surface has been found to have reduced to half of its original concentration in the alloy. The concentration of chromium in the reaction zone on the glass side is shown to have doubled from that present in the alloy. Chromium has selectively leached out from the surface of Alloy 690 in contact with molten glass at 1223 K to 1273 K. The loss of chromium on the surface is bound to change the surface properties and hence their corrosion rates at elevated temperature [12].

Because of continuous plant operation of thousands of hours, metallic components especially those, which are in contact with molten borosilicate waste glass, get coated with a heterogeneous mixture of glass and crystalline materials. This heterogeneous combination, which forms as layers on the metallic substrate, is referred as a glassy layer [38]. Interaction of Alloy 690 specimens with sodium barium borosilicate melt (used for immobilization of sulphate-rich HLW) with 21 wt.% of simulated waste oxides at 1223 K for different time

span ranging from 8 to 192 h has indicated formation of a partially crystalline and partially amorphous glassy layer, within borosilicate melt neighboring to metal/glass interface [38]. The detailed microstructural study of the interface shows the formation of three types of phases: (a) a continuous layer phase, (b) a needle phase, and (c) a cubic shaped phase. Based on compositional analyses along with X-ray imaging studies at the interface, the authors [38] have concluded that the layer phase is  $\text{Cr}_2\text{O}_3$ , needle phase is having  $\text{Ni}_2\text{CrO}_4$  stoichiometry and the cubic shaped phase is of  $\text{NiCr}_2\text{O}_4$ . The width of glassy layer is found to be increased from 5 to 15  $\mu\text{m}$  for the interaction time of 8 to 192 h respectively. In order to simulate the situation when the glassy layer detaches from the glass melter and is mixed into the melt pool, the authors have carried out the interaction studies with addition of excess amount of  $\text{Cr}_2\text{O}_3$  and  $\text{NiO}$  to the glass. It leads to the formation of barium chromate and nickel silicate crystals within borosilicate waste glass and that is expected to depreciate its chemical durability as barium chromate stabilizes the yellow phase and nickel silicate is prone to alteration. Therefore, the researchers [38] have suggested that essential steps should be adopted to reduce the growth of a glassy layer on Alloy 690 in HLW vitrification melters. Similar investigations [39] have shown that the interactions may result in Cr carbide precipitation along the grain boundaries, significant depletion of Cr content within austenitic matrix close to interface and intergranular attack close to alloy 690/borosilicate melt pool interfaces. These aspects can influence the longevity of process pot significantly [39].

Interactions between borosilicate melts and bellow liner materials, which are placed in between the pour spot and stainless steel canister in Joule heated ceramic melters are reported in literature. Interaction of materials such as copper, stainless steel and nickel based superalloys with borosilicate melt has been performed by Sengupta et. al [40]. They have

observed that a considerable elemental exchange occur across the alloy and borosilicate melt interface. In both case of nickel based superalloys and stainless steel, Cr (along with Ni and Fe) has a strong preference to get depleted from alloy matrix. This is somewhat upsetting as in both the cases Cr is purposefully added to improve alloys' oxidation resistance. Significant microstructural and compositional modifications within copper specimen has also been observed. Alloys containing Cr (i.e. Ni–Cr–Fe, Ni–Cr–Mo, Fe–Cr–Ni alloys) have a tendency to develop  $(\text{Fe,Cr})_2\text{O}_3$  layer on the interface due to chemical reaction with borosilicate melt. Copper specimen did not exhibit any hint for the formation of adherent oxide layer formation at the interface ( $\text{Cu}_2\text{O}$  formed was distributed in the melt). Therefore, the authors [40] have suggested that copper based materials are better choice for construction of bellow liner materials.

Corrosion studies of Alloy 690 and 693 in iron phosphate melt containing 30 wt.% of simulated low activity waste at 1323 K for 155 days have shown superior corrosion resistance of Alloy 693 as compared to Alloy 690 [42]. An altered surface layer depleted in nickel and consisted of  $(\text{Fe,Cr})_2\text{O}_3$  type phase has been noticed on the Alloy 690 and 693 specimens exposed in iron phosphate melt. This altered layer appears to act as a chemically protective layer on the metals [42]. In a similar investigation [43], isothermal corrosion behavior of Alloy 690 and 693 between 1273 K and 1463 K in an iron-phosphate glass containing 26 wt.% of a simulated Hanford AZ102 Low activity waste (LAW) for 7 and 14 days have been carried out. For both alloys, three distinct temperature-dependent corrosion regimes have been observed. At low temperatures (both alloys: 1273 K), no internal sulfides formed in the alloys, but the internal Cr-carbides, voids and Cr-depletion are significant. In the intermediate temperature range (Alloy 690: 1323–1373 K; Alloy 693: 1323–1438 K),

both alloys have shown the best corrosion resistance. At the highest temperatures (Alloy 690: 1413 K; Alloy 693:1463 K), the Cr concentrations (~10 wt.%) at metal surfaces were too low to form a protective scale and both alloys suffered catastrophic corrosion caused by a low-melting point Ni-phosphide eutectic corroding along grain boundaries. Over the entire temperature range, 1373–1463 K, Alloy 693 has better corrosion resistance than Alloy 690 in iron phosphate melt [43].

## **2.2 Interaction of alloys with nuclear waste solution**

Understanding of mode of interaction between Alloy 690 process pot and sulphate containing HLW at the feed stage is important as far as the durability of the melter pot is concerned. Long-term exposure of Alloy 690 melter pot material to sulphate containing HLW shows the following changes within the material, (i) depletion of Cr from the alloy at the interface (ii) intergranular attack and (iii) building up of  $\text{Cr}_2\text{O}_3$ – $\text{Ni}_2\text{O}_3$ – $\text{Fe}_2\text{O}_3$  mixed oxide surface layer containing Na and Cs precipitates and it was found that the extent of these modifications increases with increase in exposure time [44].

In order to increase the service life of melter pot materials, efforts are being made to develop suitable coatings on superalloy substrates [11,13,14]. Aluminized and thermally oxidized Alloy 690 substrates have shown good adherence in nitrate-based simulated nuclear waste solution [14] and good stability of coatings in borosilicate melt without any phase formation at the coating/glass interface [11]. SEM micrograph along the cross-section of aluminized and oxidized Alloy 690 substrate with adhered glass (exposed to sodium borosilicate melt at 1248 K for 192 h) is shown in Fig. 2.3.

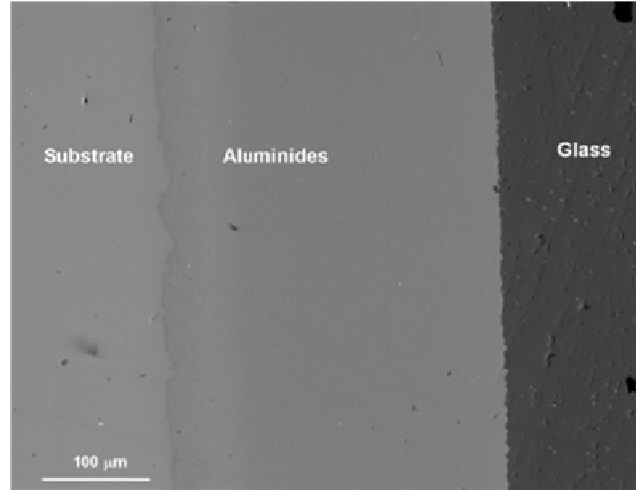


*Fig. 2.3. SEM micrograph along the cross-section of aluminized and oxidized Alloy 690 substrate with adhered glass (exposed to sodium borosilicate melt at 1248 K for 192 h) revealing different multilayers without any phase formation at the coating/glass interface [11].*

### **2.3 Glass—a candidate material for immobilization of HLW**

Nuclear waste is generated at every stage of the nuclear fuel cycle, which includes the mining of uranium, fuel fabrication through reactor operations and subsequent reprocessing of spent fuel [45]. Radioactive wastes are generated in various forms like solid, liquid or gaseous with variety of physical, chemical/radiochemical characteristics. Out of these wastes, liquid wastes require more attention due to their volumes and mobility. Depending on the level of radioactivity, radioactive liquid waste streams are commonly classified as exempt waste, low-level waste ( $37\text{--}3.7\times 10^6$  Bq/L), intermediate-level waste ( $3.7\times 10^6\text{--}3.7\times 10^{11}$  Bq/L) and high-level waste (above  $3.7\times 10^{11}$  Bq/L) [3,46]. The concentrations of long-lived radionuclides and tritium are also taken into account while classifying the liquid wastes. Among all the radioactive wastes generated in the entire nuclear fuel cycle, high level

radioactive liquid waste (HLW) contains majority (~99% of total) of the radioactivity [3,46]. Hence, it requires not only immobilization to avoid radionuclides spreading around the biosphere but also shielding and in some cases remote handling.

Since the HLW produced during reprocessing is in liquid form and highly radioactive, it requires special treatment to ensure its effective isolation from biosphere and observation for extended periods of time [46]. The commonly established approach for isolation is to convert the liquid waste into a suitable solid form, which is chemically, mechanically and thermally stable over the life time of major long lived isotopes. Solidification provides better safety during handling, transportation, storage and disposal. It also minimizes leaching of radioisotopes into the ground water [45,47]. The research and development work is directed in exploration of a suitable matrix with poor leaching (good chemical durability) and good mechanical strength. The general requirements for immobile matrix for incorporating HLW are [48,49]:

- (i) High waste loading: the matrix must be able to accommodate large amount of waste (typically 20–35%).
- (ii) Easy processing: immobilization process should be able to perform at low temperature and at air atmosphere, using well established method.
- (iii) High radiation stability: it should exhibit high tolerance to radiation effects from radionuclides present in HLW over extensive periods of time.
- (iv) Good chemical flexibility: system must be able to accommodate a mixture of radionuclides and other contaminant species.
- (v) Good durability: it should show very low leachability.

- (vi) Good mechanical strength and shock resistance: it should ensure the safe transportation to storage and disposal.
- (vii) Availability of natural analogues: naturally occurring minerals that are similar to the immobile matrices, give important hint as to the effects on the material of the natural environment thereby, creating confidence in the future performance.

Several candidate matrices like glass based matrices and crystalline matrices have been investigated and developed for immobilization of HLW worldwide. In 1950's, Canadian geoscientists came forward with the proposal to synthesize aluminosilicate glass of nephelinite bulk composition to condition HLWs [36]. The reason behind suggesting glass matrix has been essentially to take advantage of amorphous structure, which can incorporate wide variety of ions and molecular clusters within its network. Glasses are now the primary choice as materials for immobilization of potentially hazardous radionuclide in HLW [47-51]. Superior properties of glass, which make it more suitable, compared to other matrices, are: (i) small volume of the resulting waste form, (ii) the open glass structure, which allows incorporating large number of elements, (iii) simplicity in processing technique, (iv) high durability, (v) high chemical resistance leads to good corrosion stability, (vi) good thermal and radiation stability and (vii) inexpensive raw materials [45,50]. These characteristic properties of glass make vitrification as a common practice for management of high-level radioactive waste all over the world.

### **2.3.1 Glass formation**

There are two main types of pathway that a liquid may follow on cooling. Either it may crystallize at or below the melting temperature,  $T_m$ , or it may undercool sufficiently,

without crystallization, to form a glass. The relation between crystal, liquid, and glass can easily be explained by means of a volume–temperature diagram as shown in Fig. 2.4. On cooling a liquid from the initial state A, the volume will decrease gradually along AB. If the rate of cooling is slow, and nuclei are present, crystallization will occur at the melting temperature,  $T_m$ . The volume will decrease sharply from B to C, thereafter; the solid will contract with falling temperature CD. If the rate of cooling is adequately fast, crystallization does not occur at  $T_m$ ; the volume of the supercooled liquid decreases along BE, which is a smooth continuation of AB. At a certain temperature  $T_g$ , the volume-temperature graph undergoes a significant change in slope and continues almost parallel to the contraction graph CD of the crystalline form.  $T_g$  is called the glass transition temperature. Only below  $T_g$  is the material glass. The location of E, the point corresponding to  $T_g$ , varies with the rate of cooling – and thus it is appropriate to call it a transformation range rather than a fixed point [52,53].

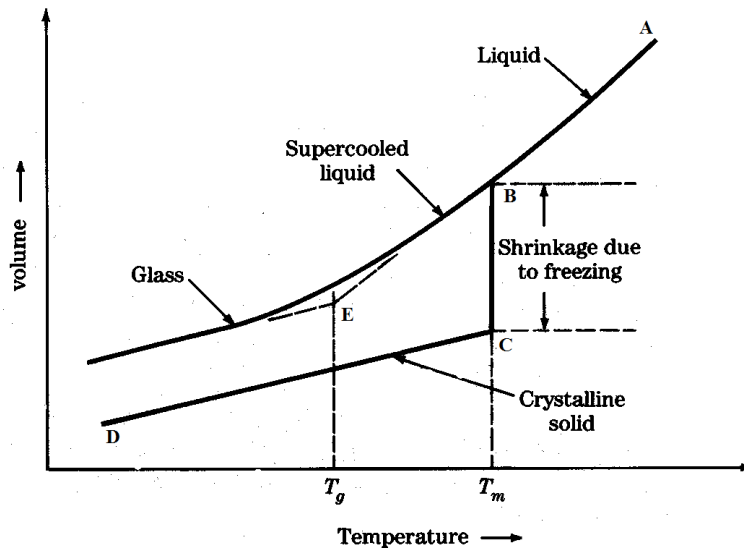


Fig. 2.4. Volume–temperature characteristics (schematic) for glassy, liquid and solid states

[49].

### 2.3.2 Glass structure

Glass is the fusion product of inorganic materials, which have been cooled to a rigid condition without crystallization. It is rigid, non-crystalline (amorphous) material. Since the mechanical properties and density of an oxide glass are similar to those of the corresponding crystal, the interatomic distances and interatomic forces must also be similar [52]. Zachariasen [54] postulated that, as in crystals, the atoms in glass must form extended three dimensional networks. But the diffuseness of the X-ray diffraction patterns shows that the network in glass is not symmetrical and periodic as in crystals. For example, in the case of  $\text{SiO}_2$  crystalline form,  $\text{Si}^{4+}$  cations are bonded to  $\text{O}^{2-}$  anions in all the three dimensions in such a way that both short-range ordering (SRO) and long-range ordering (LRO) exist within the network. However, in case of  $\text{SiO}_2$  glass, where though  $\text{Si}^{4+}$  and  $\text{O}^{2-}$  are found to polymerize in all the three directions, but due to the presence of randomness in the ionic linkages, no LRO arrangement is noticed in the network (only SRO is present) [36]. Such a difference is shown pictorially in Fig. 2.5 for silica in both crystalline (a) and amorphous (b) forms. A comparison between these two structures clearly suggests that more number of ions can be incorporated in  $\text{SiO}_2$  glass as it offers wider range of locations such as cation-, anion positions and free volumes of different sizes and shapes, for entrapment.

Zachariasen [54] proposed a set of empirical rules, which an oxide must satisfy if it is to be a glass former:

- (1) An oxygen atom is linked to no more than two other atoms.
- (2) The coordination number of the other atoms is small.
- (3) The oxygen polyhedra, formed by oxygen atoms around the other atoms, share corners and not edges or faces.

- (4) At least three corners of each polyhedron must be shared to form a three-dimensional network [52-54].

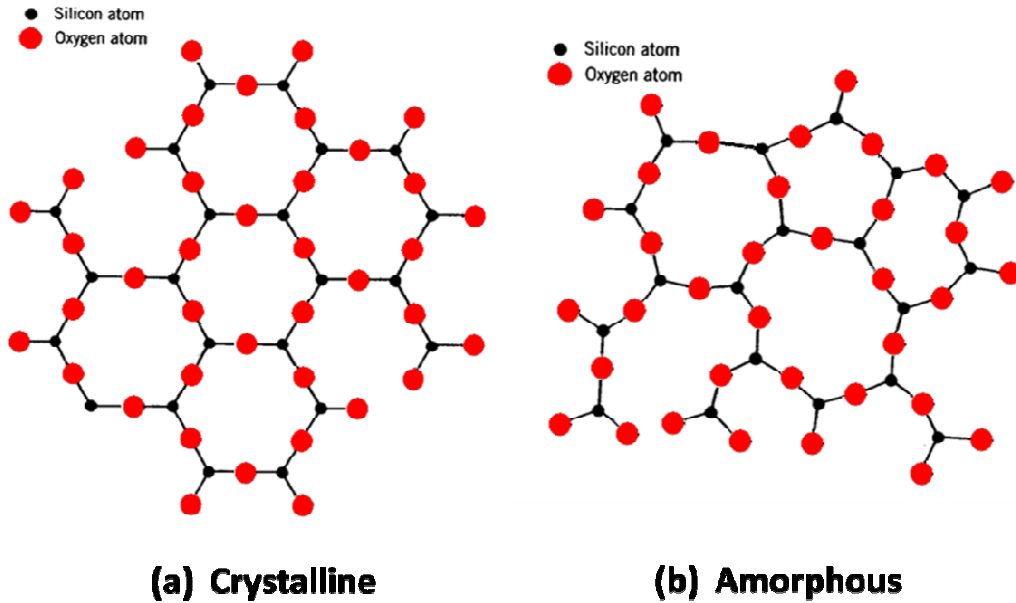


Fig. 2.5. Schematic structures of (a) crystalline and (b) amorphous silica.

The oxides involved in the glass formations can be categorized as follows [47]:

- (a) **Network former**– Oxides of elements (coordination number 4) that can produce glasses by forming chains and networks in a random manner. Normally network frames are acidic (e.g.  $\text{SiO}_2$ ,  $\text{B}_2\text{O}_3$  etc.).
- (b) **Network modifier**– Oxides of elements (coordination number higher than 4 in some compounds) that can produce glasses by melting with network formers. Generally, glass network modifiers are basic (e.g.  $\text{Na}_2\text{O}$ ,  $\text{K}_2\text{O}$ ,  $\text{Li}_2\text{O}$ ,  $\text{BaO}$ ,  $\text{CaO}$ ).
- (c) **Intermediate**– Oxides of elements (coordination number lying in between those of glass formers and modifiers) that can produce glasses by fusion with network formers. These can also act as network formers. Generally, intermediates are amphoteric (e.g.  $\text{Al}_2\text{O}_3$ ,  $\text{Fe}_2\text{O}_3$  etc.).

The glass structure further opens up when network modifiers (alkali or alkaline earth cations) enter the structure (Fig. 2.6). Incorporation of such cations requires charge compensation and this is fulfilled through depolymerization of the network. This modification in the network due to introduction of network modifier leads to the formation of non-bridging oxygens (NBO; oxygen linked to  $\text{Si}^{4+}$  and  $\text{Na}^+$ ) from bridging oxygen precursors (BO; oxygen linked to two  $\text{Si}^{4+}$  cations) and transformation of  $\text{Si}^{4+}$  cations from  $\text{Q}^4$  type to  $\text{Q}^3$ ,  $\text{Q}^2$  and  $\text{Q}^1$  types, where  $\text{Q}^n$  denotes 'n' number of BOs linked with one  $\text{Si}^{4+}$  cation. Chemical durability of the glass increases with increase in the number of BOs, since they help in maintaining the network continuity. NBO's bond covalently with formers and ionically with modifiers and cannot keep the network continuity due to the electrostatic nature of the ionic bond. This kind of network modification makes the glass matrix more suitable for wider range of radionuclide entrapment (Fig. 2.7) and reduces its synthesis temperature. However, significant decrease in leach resistance of the glass matrix may occur due to excess of depolymerization of the network, which is not acceptable as far as waste immobilization application is concerned. As stated earlier, it was initially thought to use nephelinite based aluminosilicate glass compositions for HLW immobilization, but in laboratory scale, it was noted that synthesis temperature had to be as high as 1673–1773 K in order to achieve homogeneous loading of sufficient amount of simulated HLW. Such temperature range is however difficult to attain in induction heated metallic melters as the components of the melter pots are made up of Alloy 690, whose melting point is less than 1673 K. To overcome this problem, the idea of replacing  $\text{Al}_2\text{O}_3$  component of the aluminosilicate glass by  $\text{B}_2\text{O}_3$  flux has been implemented and this has considerably reduced the synthesis temperature to 1223–1273 K. This leads to the concept of using borosilicate

glass matrices for immobilization of HLWs [36]. Borosilicate based glass system has been investigated extensively and has become the primary choice of material worldwide for immobilization of nuclear waste materials having capability to hold radioactivity for long durations [55-61]. Sodium borosilicate glass has ability to tolerate minor variations of waste composition. Moreover, its high chemical, mechanical and thermal stability, sufficient waste solubility, moderate processing temperatures (1273 K-1473 K) and more compatibility as host solid with the waste components makes it more suitable as matrices for nuclear waste immobilization [62-64].

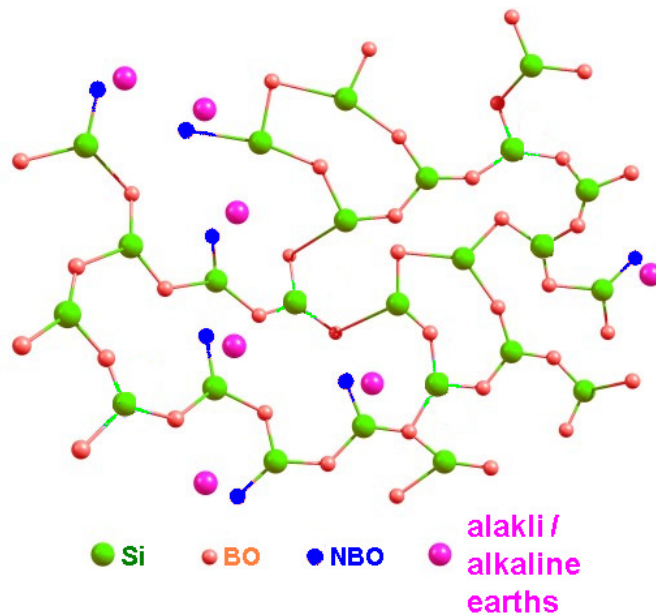


*Fig. 2.6. Schematic structure of silicate glass [36].*

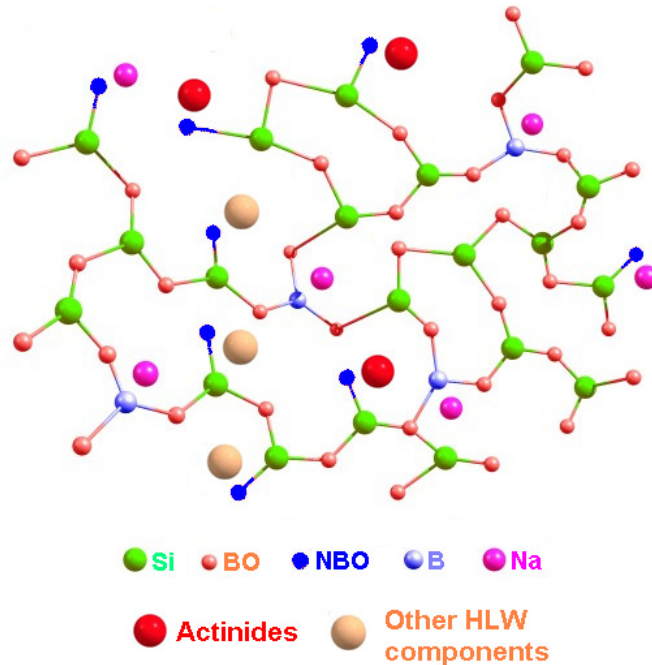


Fig. 2.7. Schematic structure of nuclear waste glass [36].

### 2.3.3 Effect of foreign elements in glass structure

Uranium ions play a part in the network formation of multi component borosilicate  $\text{SiO}_2\text{-B}_2\text{O}_3\text{-Na}_2\text{O-BaO-ZrO}_2$  glass loaded with 30 wt.%  $\text{UO}_3$  [65]. It has been established that the basic network structure consists of tetrahedral  $\text{SiO}_4$  units and of mixed tetrahedral  $\text{BO}_4$  and trigonal  $\text{BO}_3$  units, being rather similar to the network structure of the corresponding host glass [66]. Neutron and X-ray diffraction studies have revealed that with increasing boron content, the relative number of  $\text{BO}_3/\text{BO}_4$  increases and the first neighbor  $r_{\text{B-O}}$  distance decreases [65]. The ionic conductivity of the barium borosilicate glasses is independent of  $\text{ThO}_2$  content upto 5 mol% [67]. The results of electrical properties, differential thermal analysis (DTA), and  $^{29}\text{Si}$  and  $^{11}\text{B}$  magical angle spinning nuclear magnetic resonance spectroscopy (MAS NMR) studies suggest that borosilicate network is unaffected by  $\text{ThO}_2$  incorporation in the glass [67]. For barium borosilicate glasses

containing 15.86 wt.% ThO<sub>2</sub> and different amounts of uranium oxide, MAS NMR studies have indicated that uranium oxide incorporation is linked with distortion of borosilicate network due to increase in relative concentration of Q<sup>2</sup> structural units of silicon as well as the increase in quadrupole coupling constant (C<sub>q</sub>) of BO<sub>3</sub> structural units [68]. This increased concentration of Q<sup>2</sup> structural units of silicon generates more number of NBOs and facilitates the incorporation of both uranium and thorium ions in the sites created by NBOs (network modifying positions) in the glass. X-ray diffraction studies show that uranium oxide incorporation above 7.5 wt.% results in the phase separation of ThO<sub>2</sub> [68]. The addition of vanadium oxide (V<sub>2</sub>O<sub>5</sub>) to the sodium barium borosilicate glass within the solubility limit (≤5 mol%) results in the depolymerization of the borate network through the formation of Q<sup>3</sup> and Q<sup>4</sup> structural units, leads to decrease in hardness of the glass [69]. Beyond 5 mol%, it separates out into three phases, (i) silica, (ii) Barium (Ba) – Vanadium (V) oxide, and (iii) glass matrix. Below 5 mol% of V<sub>2</sub>O<sub>5</sub> addition, silicate network is mainly composed of Q<sup>2</sup> and Q<sup>3</sup> structural units. In case of borate network, the concentration of BO<sub>4</sub> unit increases gradually up to 5 mol% and then it decreases at the expense of BO<sub>4</sub> (1B, 3Si), BO<sub>3</sub> (symmetric) and BO<sub>3</sub> (assymmetric) units [69].

Incorporation of nuclear waste elements such as U, Cs and Bi does not amend the basic features of the parent iron phosphate glass [70]. An O1s XPS spectrum indicates that only 16–26 % of the oxygen ions are BOs in iron phosphate glasses and in the glasses containing waste components UO<sub>2</sub>, Cs<sub>2</sub>O and Bi<sub>2</sub>O<sub>3</sub>. Much change in BO/(BO+NBO) ratio has not observed after the addition of waste components. The Mössbauer hyperfine parameters, isomer shift and quadrupole splitting, have shown that the environment around the Fe ions is independent of the glass composition. The isomer shifts and quadrupole

splitting indicates that the  $\text{Fe}^{3+}$  and  $\text{Fe}^{2+}$  ions in iron phosphate glasses are in octahedral or distorted octahedral coordination. The fraction of  $\text{Fe}^{2+}$  in the glass increases with the melting temperature [70].

The interfacial reaction between borosilicate glass and sapphire ( $\alpha\text{-Al}_2\text{O}_3$ ) at 1123–1223 K have indicated the buildup of interdiffusion layer with  $\text{Al}^{3+}$  ion dissolving from sapphire and other alkali ions such as  $\text{K}^+$ ,  $\text{Na}^+$  and  $\text{Li}^+$  dissolving from borosilicate glass onto the interface of sapphire/borosilicate glass, and  $\text{Al}^{3+}$  and  $\text{K}^+$  are all the time linked together in the reaction layer [71].  $\text{Na}^+$  and  $\text{Li}^+$  could not be detected clearly because of their low molecular weight and concentration. The interdiffusion layer shifts toward borosilicate glass with time and the reaction starts instantly at selected temperatures without any incubation time. The growth kinetics for the interdiffusion layer follows a parabolic rate law. The interdiffusion layer at the interface is rich in  $\text{Al}^{3+}$ ,  $\text{K}^+$ , and poor in  $\text{Si}^{4+}$  in a glassy matrix whose composition is different from borosilicate glass [71].

## 2.4 Summary

The detailed discussion presented above deals with interaction of molten glass with metals and alloys such as chromium alloys, chromium oxide and nickel-based alloys at elevated temperature. Interaction of these materials with molten glass with different compositions as a function of temperature and characterization by using various techniques has been discussed in detail. Interaction of alloys with acidic environment (nuclear waste solution) has been discussed subsequently. Glasses are the first choice as materials for immobilization of potentially hazardous radionuclide in HLW. Properties of glass that makes

suitable for immobilization, conditions for the formation of glass, structural aspects and effects of foreign elements on the glass structure are discussed in detail.

From the above discussions, it is clear that several studies have been reported in the literature related to the interaction of a variety of materials with molten glass and acidic environment. However, detailed interaction of aluminide coated nickel based superalloys with simulated nuclear waste and molten borosilicate glass has not been appeared in literature. Keeping this in mind, interaction of aluminized and oxidized Alloy 690 specimens with simulated nuclear waste solution (nitrate-based environment) and sodium borosilicate melt followed by characterization have been performed and discussed in detail in this thesis.

# *Experimental Methods and Characterization*

## *Techniques*

---

This chapter mainly deals with the experimental methods used for preparation of the samples, thermal oxidation studies and exposure experiments with simulated high-level nuclear liquid waste and sodium borosilicate melt. In addition, the analytical and the instrumental techniques used for characterization purpose has also been discussed.

### **3.1 Pack Aluminization:**

Several methods for surface coatings e.g. thermal spraying, physical vapour deposition, pack cementation, plasma spraying, magnetron sputtering, hot dipping have been recommended in literature. Out of these, pack cementation is not only most effective, but also inexpensive. Pack cementation is essentially an in-situ chemical vapour deposition (CVD) process that has been used to make corrosion- and wear-resistant coatings on metallic surfaces [72]. For nickel-based superalloys, aluminium is the element, which is most commonly deposited by this method to form nickel aluminide coatings. At high operating temperatures, aluminium in the coating oxidizes preferentially to form a thin, adherent and dense alumina scale, which acts as a diffusion barrier and thus protects the substrate from oxidation.

The substrates to be coated are placed in a sealed or semi-sealed container together with a powder mixture that consists of metallic elements to be deposited, halide activators and inert filler (usually alumina). The components may be buried in or placed above the powder mixture. The halide activators are usually added in small quantities (2 to 5 wt.%) and they may be stable halide or unstable halide salts, like  $\text{NH}_4\text{Cl}$ . The sealed container is heated under a protective atmosphere of Ar to a temperature between  $700^\circ\text{C}$  to  $1150^\circ\text{C}$  and held there for a specified duration. At these coating temperatures, the halide activators react with the metallic elements in the powder mixture and form a series of metal halide vapours such as  $\text{AlCl}$  with a characteristic partial pressure distribution, which is determined by their thermodynamic stability in a particular powder pack. The coating is formed via reduction reactions of metal halide vapours at the substrate surface and subsequent solid state diffusion of the metal elements into the substrate. For this reason, the coatings produced using this process is also termed “diffusion coatings”.

Commercially available mill-annealed Ni-based superalloy 690 was used as substrate in the present investigation. The chemical composition of the alloy is given in Table-3.1. Substrates having initial dimensions of about  $10\text{ mm} \times 10\text{ mm} \times 4\text{ mm}$  were ground (all the sides) up to 600 silicon carbide emery paper. This was followed by cleaning, drying and weighing prior to pack aluminization. A schematic diagram of pack aluminization process is shown in Fig. 3.1. Two sets of aluminized samples were prepared with different pack compositions. The high Al-containing pack was composed of 10 wt.% Al powder (particle size finer than  $200\ \mu\text{m}$ ), 5 wt.%  $\text{NH}_4\text{Cl}$  and 85 wt.%  $\text{Al}_2\text{O}_3$  powder while the low Al-containing pack was composed of 2 wt.% Al powder, 2 wt.%  $\text{NH}_4\text{Cl}$  and 96 wt.%  $\text{Al}_2\text{O}_3$  powder. The alloy substrates were embedded in an alumina crucible one by one after proper

ramming of the space separating them. After putting alumina lid, the whole crucible was covered with high temperature cement and kept for drying for 2 days. The pack aluminization was carried out in a resistance heating furnace having a constant temperature zone of about 200 mm. The packs were heated at a rate of 4K/min to 1273 ( $\pm 5$ ) K, the high Al-containing pack was soaked for 10 h and low Al-containing pack was soaked for 4h and cooled to room temperature at a rate of 4K/min. An argon atmosphere was maintained during entire cycle.

Table-3.1: Chemical composition of the substrate superalloy 690 (wt.%).

C	Ni	Cr	Fe	Cu	Mn	S	Si
0.03	Bal	28.0	9.6	0.05	0.17	0.001	0.04

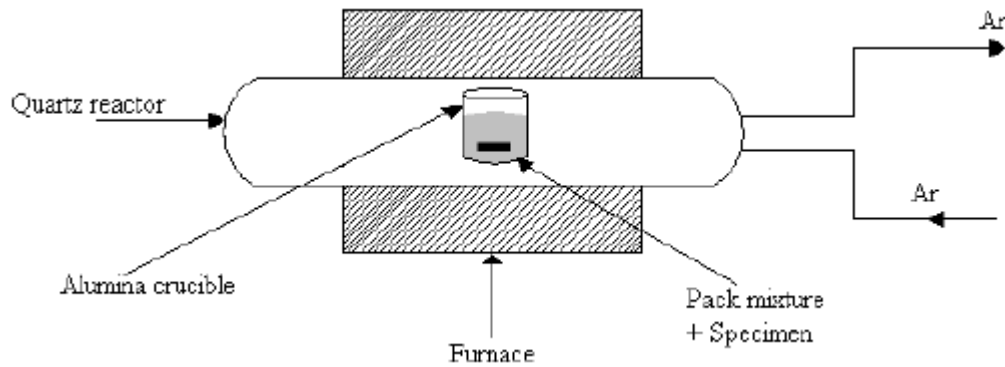


Fig. 3.1. Schematic diagram of pack aluminization process.

### 3.2 Thermal Oxidation:

Pack aluminized specimens of superalloy 690 were polished upto 320 grit emery paper to obtain a smooth surface. Thermal oxidation of aluminized specimens made from

high Al-containing pack was carried out at 1273 K for a total period of 4 h. Aluminized specimens from low Al-containing pack was carried out for 8 h at 1273 K, in a resistance heating horizontal furnace without using any controlled atmosphere followed by air cooling. After every 2 hours of heat treatment, samples were taken out and cleaned, dried and weight changes were noted.

### **3.3 Exposure to Simulated Nuclear Waste:**

Aluminized (with high and low Al-containing packs) and thermally oxidized Alloy 690 specimens having dimensions of about 10 mm × 10 mm × 5 mm were exposed to simulated high-level nuclear liquid waste (nitrate-based environment) at 373 K for a period of 216 h. The selection of time and temperature parameters for the present experiments was done by considering the real plant scale vitrification process. Feeding (mixing of HLW and glass additive slurry) and evaporation are performed at 373–378 K and 378–393 K respectively in actual vitrification process [36] and that is why the temperature was kept at 373 K. As the vitrification process is carried out in a batchwise manner, the exposure experiments were carried out for longer durations in order to simulate the effect of repeated cyclic process. Prior to the exposure, initial weight of the specimens were taken. In order to avoid handling of high-level radioactive liquid waste, simulated nuclear waste was used. Composition of simulated nuclear waste solution used in the present study is given in Table-3.2.

The cleaned samples (aluminized and thermally oxidized Alloy 690 substrate) were immersed in 100 ml simulated nuclear waste solution that was taken in a 250 ml round-bottomed flask and the flask was maintained at a temperature of 373 K during the experiment. The flask was fitted with an air-cooled condenser to avoid loss of the solution.

The experimental set-up of exposure system is illustrated in Fig. 3.2. For comparison of results, samples of bare Alloy 690 substrate (without aluminization and oxidation) were also exposed in the same simulated nuclear waste under the similar experimental conditions. At the end of the experiments, samples were removed from the flask, cleaned, dried and weighed.

Table-3.2: Chemical composition of simulated nuclear high level waste solution used.

Chemicals	Conc. (g/l)
$\text{Ca}(\text{NO}_3)_2 \cdot 4\text{H}_2\text{O}$	2.5926
$\text{Al}(\text{NO}_3)_3 \cdot 9\text{H}_2\text{O}$	30.6495
$\text{Fe}(\text{NO}_3)_3 \cdot 9\text{H}_2\text{O}$	10.4528
$\text{Ni}(\text{NO}_3)_2 \cdot 6\text{H}_2\text{O}$	1.3374
$\text{CrO}_3$	0.7019
$\text{Mg}(\text{NO}_3)_2 \cdot 6\text{H}_2\text{O}$	2.5838
$\text{Mn}(\text{NO}_3)_2 \cdot 6\text{H}_2\text{O}$	2.8996
$\text{MoO}_3$	0.3976
$\text{Ce}(\text{NO}_3)_3 \cdot 6\text{H}_2\text{O}$	0.3408
$\text{La}(\text{NO}_3)_3 \cdot 6\text{H}_2\text{O}$	0.2337
$\text{NaNO}_3$	17.4148
$\text{Sr}(\text{NO}_3)_2$	0.1449
$\text{Ba}(\text{NO}_3)_2$	0.1700
$\text{CsNO}_3$	0.5147

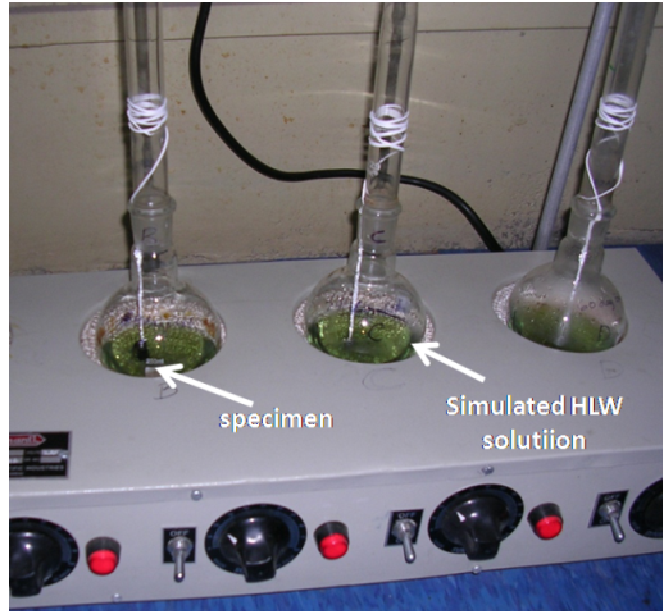


*Fig. 3.2. Experimental set-up used for exposure of specimens with simulated nuclear waste solution at 373 K for 216 h.*

### **3.4 Exposure in Sodium Borosilicate Glass:**

Aluminized (with high and low Al-containing packs) and thermally oxidized Alloy 690 specimens having dimensions of about 10 mm × 10 mm × 5 mm were subjected to interaction with sodium borosilicate melt at 1248 K for a total period of 192 hours. In actual plant scale operations, temperature of the borosilicate melts, while pouring, generally fall in between 1223–1273 K [2] and hence present experiments were performed at 1248 K. Borosilicate melt is soaked for 10 h for homogenization, however to replicate the effect of repeated cyclic process, experiments were carried out for longer periods. A known weight of sodium borosilicate glass was treated with hydrofluoric acid and warmed. The resultant solution was then boiled with perchloric acid to remove excess HF. Once all HF is removed, the solution is evaporated to dryness and then nitric acid was added and made upto a known fixed volume and analyzed for elements like Na, Fe, Ti etc. by atomic emission spectroscopy

(AES). In order to analyze the silicon and boron content, a known weight of glass was fused with sodium carbonate at 1100°C in a platinum crucible. The residual mass was dissolved in nitric acid and the solution was analyzed by AES. The atomic composition of elements of the glass was determined theoretically from the composition of oxides chosen for preparation of glass. Composition of oxides in the sodium borosilicate glass and atomic composition of elements are given in Table-3.3(a) and Table-3.3(b) respectively. About 6 gram of glass beads was taken in a sillimanite crucible of internal diameter of about 17 mm and height of 18 mm and that was kept in a pre-heated (1248 K) chamber type furnace in air atmosphere. The furnace and the sillimanite crucible used in this study are shown in Figs. 3.3 and 3.4 respectively. Aluminized and thermally oxidized Alloy 690 specimen was dipped in glass when it reached molten state and the temperature of the melt was maintained at 1248 K for a period of 192 hours. Bare Alloy 690 substrates were also kept in another crucible under similar experimental condition for comparison. After exposure of the specimens (both aluminized + thermally oxidized and bare alloy samples) in borosilicate melt, the adhered glass phase was removed carefully from the specimen and used for analysis with FTIR spectroscopy, XPS and micro-Raman spectroscopy. Surfaces of the exposed specimens (after removal of glass phase from the top) were analyzed using X-ray photoelectron spectroscopy (XPS), Electron probe micro-analyzer (EPMA), micro-Raman spectroscopy and scanning electron microscopy (SEM) with Energy dispersive X-ray spectroscopy (EDXS) techniques.

Table-3.3 (a): Composition of oxides in sodium borosilicate glass used.

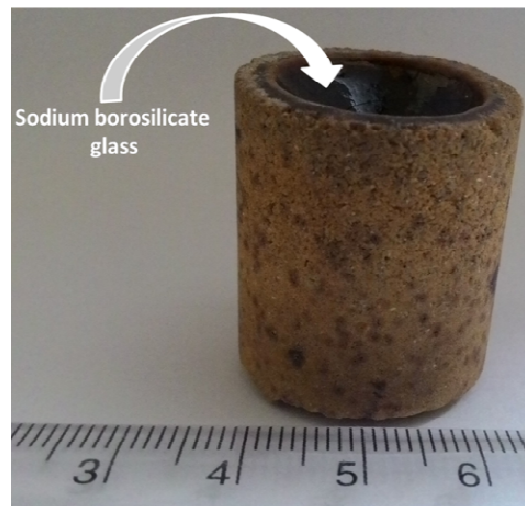
Compositions of oxides (wt.%)				
SiO <sub>2</sub>	B <sub>2</sub> O <sub>3</sub>	Fe <sub>2</sub> O <sub>3</sub>	TiO <sub>2</sub>	Na <sub>2</sub> O
48.0	26.0	4.5	9.5	12.0

Table-3.3 (b): Concentration of elements in borosilicate glass used.

Compositions of elements (at.%)					
O	Si	B	Na	Ti	Fe
60.59	14.94	13.95	7.24	2.2	1.04



*Fig 3.3. Chamber type furnace used for exposure of specimens with sodium borosilicate melts.*



*Fig 3.4. Sillimanite crucible used in the present study in which specimens along with borosilicate glass has been exposed.*

### 3.5 Characterization Techniques:

#### 3.5.1 Scanning Electron Microscopy (SEM) with Energy Dispersive X-ray Spectroscopy (EDS):

Scanning Electron Microscope uses a focused beam of high-energy electrons to generate a variety of signals at the surface of solid specimen. Three major signals that result from interaction of the electron beam with the sample are secondary electrons (SE), backscattered electrons (BSE) and transmitted electrons. Emission of characteristic X-rays, cathodoluminescence and absorption of electrons also happen during the interaction. Various interactions of the electron beam with specimen is shown in Fig. 3.5.

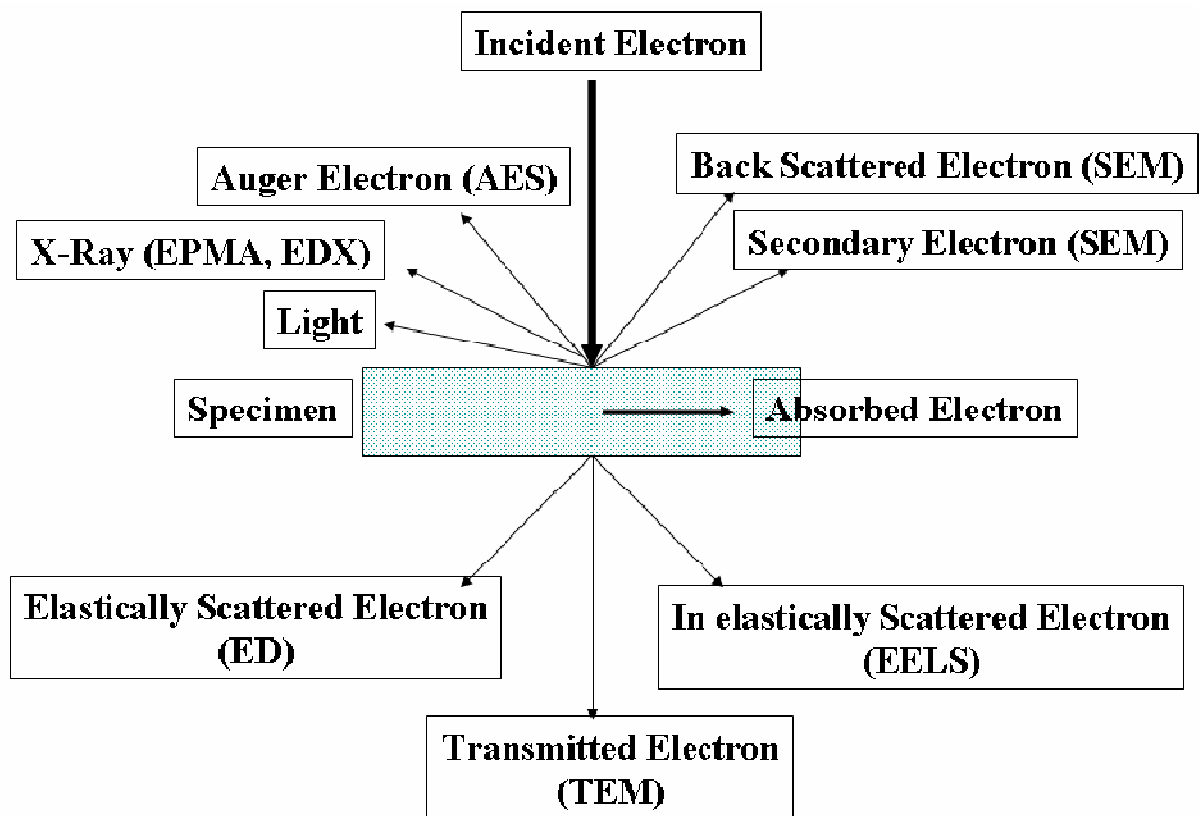


*Fig. 3.5. Different signals resulting from interaction of the electron beam with specimen.*

In scanning electron microscopy, the signals generated from the surface of the specimen like secondary and backscattered electrons are detected and are fed to a synchronously scanned cathode ray tube (CRT) monitor as an intensity-modulating signal and thus an image of the specimen is generated on the CRT screen [73]. The CRT monitor width divided by the electron probe scanning width determines the image magnification. Scanning microscope is composed of (i) electron optical system, (ii) specimen stage, (iii) display and recording system and (iv) vacuum system. A schematic of scanning electron microscope is given in Fig. 3.6.

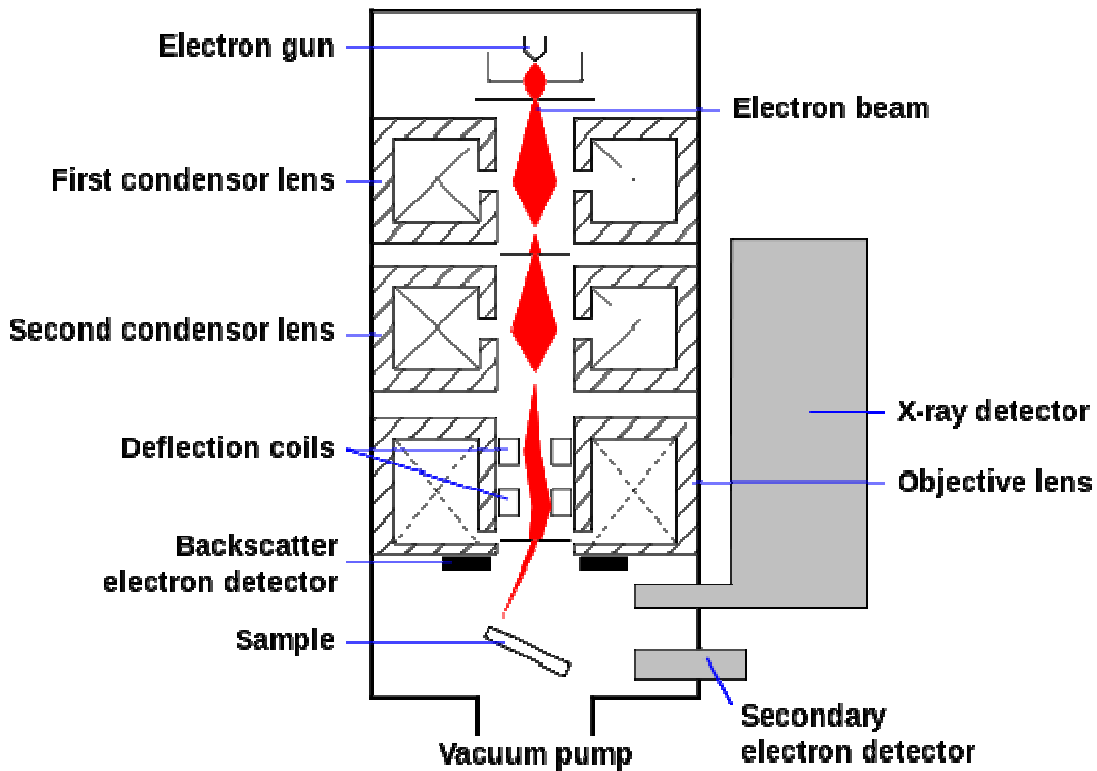


*Fig. 3.6. Schematic diagram of a scanning electron microscope.*

In SEM [73], a finely focused beam of high energy electrons (0.2 keV to 40 keV) are rastered on surface of the sample. The electron beam interacts with the sample to generate a

host of signals like BSE, SE and transmitted electrons. Electrons are reflected by the surface of the sample and emitted secondary electrons are detected to give a map of the surface topography of the sample. It is useful for looking at particle size, crystal morphology, magnetic domains, surface defects, etc. A wide range of magnification can be used, the best achievable resolution being about 2 nm. An electron beam incident on a metal gives rise to the emission of characteristic X-rays from the metal. In electron microscopy, the elements present in the sample also emit characteristic X-rays. These are dispersed by a silicon-lithium detector and each signal is collected, amplified and corrected for absorption and other effects, to give both qualitative and quantitative analysis of the elements present (for elements of atomic number greater than 11) by using a technique known as energy dispersive X-ray spectroscopy (EDS).

In the present study, SEM (Camscan MV2300CT/100, UK) was used for examining the thermally grown oxide layer formed on aluminized Alloy 690 specimen (prepared from high Al-containing pack) along the cross-section under BSE as well as SE modes. EDS (Oxford, X-Max 80) analysis was carried out for quantitative analysis of elements at different locations on point-to-point basis along the cross-section. SEM with EDXS was also used for microstructural characterization along the cross-section of specimens (both aluminized + thermally oxidized and bare alloy samples) with adhered glass after the exposure in borosilicate melt. SEM (Carl Zeiss Auriga FE-SEM) was used to study surface of the aluminized and thermally oxidized Alloy 690 specimen (prepared from low Al-containing pack), that was exposed to simulated nuclear waste and sodium borosilicate melt and EDS (Oxford EDS detector 50 mm X-Max) technique was used for composition analysis of surface of the exposed specimen. Typical depth resolution for characterization of

composition using EDS technique is  $\sim 1\text{--}2\ \mu\text{m}$ . Minimum detectable concentration of elements using EDS technique is 1000–3000 parts per million (ppm). The energy of spectrum was calibrated with standard samples and it was found to be 128 eV for EDS.

### 3.5.2 Electron Probe Micro-Analysis (EPMA):

Electron micro-probe analyzer include an electron optical column to produce a finely focused electron beam, a scanning system, one or more electron detectors and a cathode ray tube (CRT) display system. Micro-chemical analysis in EPMA is based on measurement of the X-rays generated by the focused electron beam. The ability to perform chemical analysis in an EPMA is the result of existence of a relationship between the wavelength  $\lambda$  of the characteristic X-ray emitted from an element and its atomic number  $Z$  (for K radiation) which can be given as

$$Z \propto \lambda^{-1/2}$$

When the electron beam strikes the sample, vast majority of the energy is dissipated thermally. A fraction of the incident electrons having sufficient energy to exceed the excitation potential  $E_c$  (the bonding energy of the core electron), cause ejection of the core electron from an atom leaving a vacancy. This vacancy is then filled by an electron from higher energy state by the electronic relaxation with simultaneous release of a discrete energy corresponding to the difference between the orbital energy levels. This energy may be either in the form of an X-ray or an auger electron. These X-rays are detected and characterized by means of an energy-dispersive spectrometer (EDS) or a wavelength-dispersive spectrometer (WDS, also known as crystal diffraction spectrometer, CDS). The basic operating principles of the instrument are demonstrated in Fig. 3.7.

An electron optical column containing an electron gun, magnetic lenses, a specimen chamber and various detectors are maintained at vacuum of at least  $10^{-5}$  mm Hg. A directly heated filament provides a source of electron for the electron gun. The filament is held at a negative potential, 5 to 30 kV relative to the gun anode, which is grounded. A grid placed between the filament and the anode is biased at a potential slightly less than that of the filament. Thus electrons are attracted from the filament to the anode focused by the field of the grid cap. The electron gun acts as a lens, forming an image of the filament which is then demagnified by two or more magnetic lenses to form the final probe. The probe size is in the range of 0.1 to 1  $\mu\text{m}$  with corresponding probe currents in the range of about 10–1000 nA.

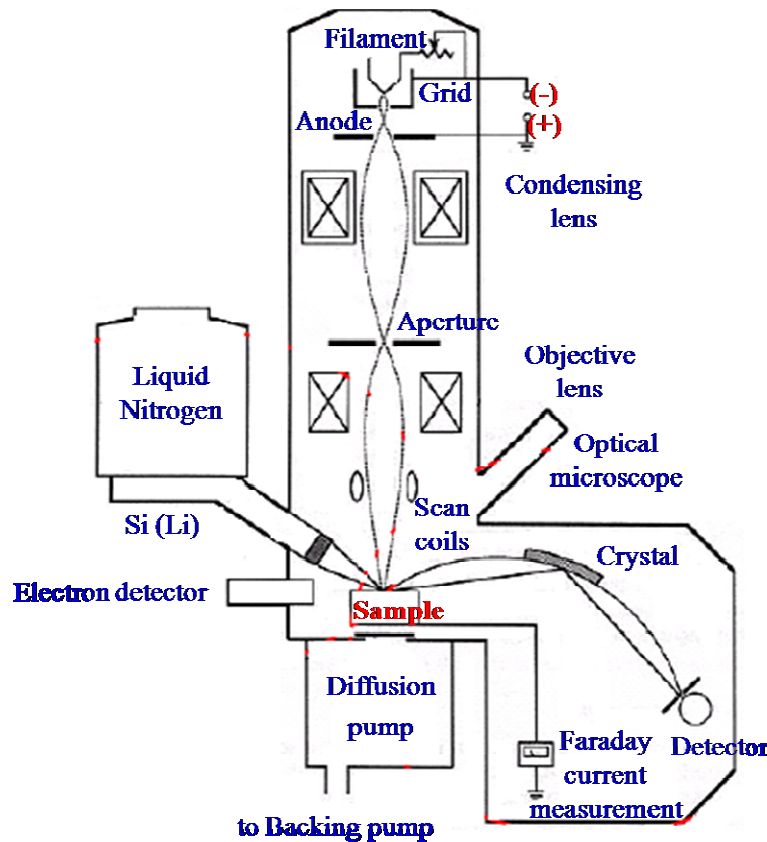


Fig. 3.7. A schematic figure of EPMA.

When the focused electron beam strikes the sample a variety of signals are generated, including backscattered electrons, secondary electrons and X-rays. The backscattered electron signal varies with atomic number. It is the X-rays that provide a unique way of performing both quantitative and qualitative analysis which can be detected by either WDS or EDS systems. By using wavelength dispersive spectra better resolution in the compositional analysis can be obtained in EPMA than that in the energy dispersive SEM analysis. In this study, EPMA with WDS was used for surface characterization of the aluminized and thermally oxidized Alloy 690 substrate (prepared from high Al-containing pack) exposed with simulated nuclear waste and sodium borosilicate melt. In the present study, images for SEM are obtained in secondary electron (SE) and back-scattered electron (BSE) mode. Typical depth resolution for characterization of composition using WDS technique is ~1–2  $\mu\text{m}$ . Minimum detectable concentration of elements using WDS technique is 30–300 ppm. The energy of spectrum was calibrated with standard samples and it was found to be 2 eV for WDS.

### **3.5.3 Fourier Transform–Infrared Spectroscopy (FT-IR):**

Infrared absorption spectroscopy is one of the most important techniques used in a wide variety of scientific fields. It is a non-destructive tool, which gives information about the structure of material by investigating interaction between electrical component of the infrared radiation and matter [74]. An infrared spectrum is obtained by passing infrared radiation through the sample and determining the fraction of the incident radiation, which is absorbed at certain energy. The energy at which any peak in an absorption spectrum appears corresponds to the frequency of vibration of a part of a molecule in the sample. Infrared spectrum is a plot of wavenumber vs. absorbance (or transmittance) as a measure of band

intensity, where wavenumber is number of waves that exist over unit length (normally in centimeter) and the unit used is  $\text{cm}^{-1}$ . It is given by the following relationship:

$$\bar{\nu} = \frac{1}{\lambda}$$

Where  $\bar{\nu}$  is wavenumber and  $\lambda$  is wavelength of the radiation.

The infrared spectrum is displayed by plotting the quantity  $T = I/I_0$  as a function of wavenumber, where  $T$  is the transmittance,  $I_0$  and  $I$  are the intensity of the incident radiation and the transmitted radiation, respectively. In most of the cases, the absorbance  $A$  ( $A = -\log T$ ) is plotted against wavenumber since the absorbance at a given wavelength is directly proportional to the concentration of a sample according to the Beer's law is given below:

$$A = \log_{10} \frac{I_0}{I} = \epsilon dc$$

Where  $A$  is absorbance,  $I_0$  and  $I$  are the intensity of the incident radiation and the transmitted radiation,  $\epsilon$  is the extinction coefficient which reflects the transition probability,  $c$  is the concentration of the sample, and  $d$  is the thickness through which the radiation is travelling (i.e., the path length).

The infrared spectra of most of the materials consist of a large number of absorption bands. These bands originate from the interaction (energy exchange) between discrete light quanta and mechanical motions (vibrational and rotational) of the molecules which are excited by the absorption of infrared radiation. The frequencies of the vibrational motion of the molecules are in the same frequency range with that of infrared radiation. For a vibration to give rise to absorption of infrared radiation, there are two criteria:

- A molecule should have a frequency of vibration similar to electromagnetic wave
- Change in dipole moment should not be equal to zero

FTIR method is based on the interference of radiation between two beams to yield an interferogram. The interferogram is a signal produced as a function of the change of path length between two beams. The most important feature of FTIR spectrometer is that, it measures intensity over a narrow range of wavelengths at a time. Fourier Transformation is simply a mathematical means of sorting out the individual frequencies from the interferogram for the final representation of an IR spectrum [75].

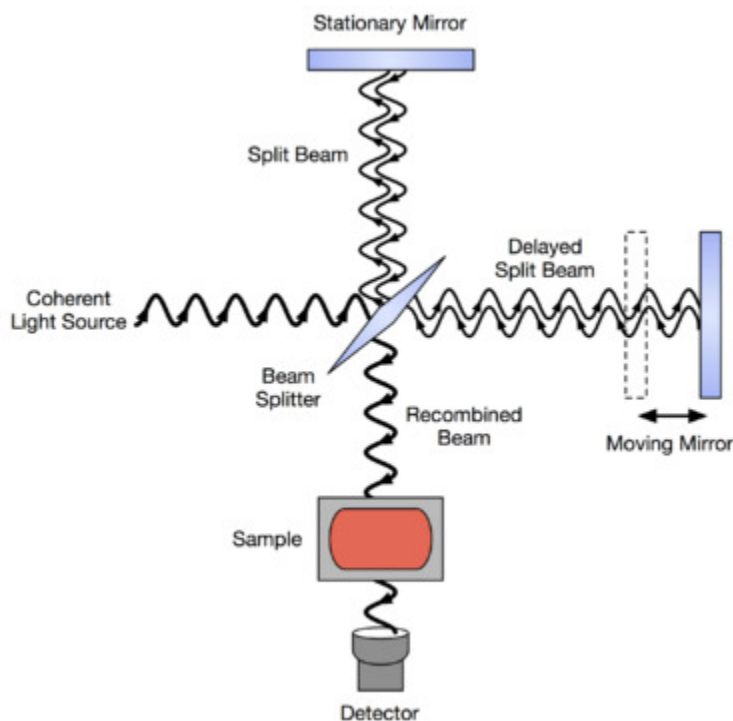


*Fig. 3.8. Schematic diagram of Michelson type interferometer.*

The most commonly used interferometer is Michelson Interferometer (Fig 3.8). It consists of two perpendicular plane mirrors one of which can travel in a direction perpendicular to its plane. A semi-reflecting film called beam-splitter bisects the planes of these two mirrors. When a collimated beam of monochromatic radiation of wavelength  $\lambda$  passes through an ideal beam splitter 50 % of the incident radiation will be reflected to one of the mirror. The two beams are reflected from these mirrors returning to the beam-splitter

where they recombine and interfere. 50 % of the beam reflected from the fixed mirror is transmitted through the beam-splitter and passes into the sample compartment, and the other 50 % is reflected back in the direction of the source. The beam, which emerges from the interferometer at 90 degrees to the input beam, is called transmitted beam and this is the beam, which is detected in FTIR spectroscopy [76]. Usually the pellets used for FTIR acquisition are made up of CsI, KBr, CaF<sub>2</sub> or LiF which are virtually transparent to infrared radiation, unlike glass which has very high absorbance in the conventional infrared range.

FT-IR absorption spectra of sodium borosilicate glass interacted with aluminized samples (using high Al-containing pack) having Al<sub>2</sub>O<sub>3</sub> layer on surface were recorded at room temperature in two separate regions, viz. mid-infrared (400-4000 cm<sup>-1</sup>) and far-infrared (150-650 cm<sup>-1</sup>) using Bruker Vertex 80 V FT-IR spectrometer. About 1.0 mg powder of glass sample taken from the vicinity of the aluminized and oxidized superalloy 690 specimen after the interaction was mixed with 100 mg of CsI in an agate mortar and then pressed to obtain 13 mm diameter pellets. The spectra were recorded in the transmission mode with a spectral resolution of 4 cm<sup>-1</sup> using a globar source, KBr beam splitter and deuterated triglycine sulfate (DTGS) detector in mid-infrared region, whereas in far-infrared region, Hg source, mylar beam splitter and DTGS detector were used. The spectra of unreacted glass were recorded as background spectrum in both the regions. In the present investigation, sodium borosilicate glass that interacted with and oxidized Alloy 690 specimen were analyzed by making pellets with CsI.

#### **3.5.4 Micro-Raman Spectroscopy:**

Raman spectroscopy is a vibrational spectroscopy technique based on the phenomenon known as ‘Raman effect’, named after the Indian scientist Sir Chandrasekhara

Venkata Raman who first discovered it in 1928 (Nobel prize in 1930) [77-79]. Raman spectroscopy probes molecular and crystal lattice vibrations and therefore is sensitive to the composition, bonding, chemical environment, phase, and crystalline structure of materials. These characteristics make it a useful technique for identification of a wide range of substances in different states viz. solids, liquids and gases. When light quanta of energy  $h\nu_0$  hits matter, a small fraction of the incident radiation is scattered, either elastically (Rayleigh scattering, Fig. 3.9) or inelastically, giving rise to emitted photons of energies either higher or lower than that of the incoming radiation: this is called Raman effect. The photons emitted at the lower energy,  $h\nu_0-h\nu_1$ , are called Stokes Raman photons (Fig. 3.9). The energy difference  $h\nu_1$  arises from the energy lost from the incoming photon to promote the molecule into an excited vibrational level of the ground electronic state. Anti-Stokes Raman photons (Fig. 3.9) appear at the same energy difference in relation to the excitation line, but on the high-energy side of the Rayleigh photons [80]. The intensities of anti-Stokes Raman bands are very weak, and temperature dependent (following the Boltzmann law). Consequently, Raman spectra reported in the literature commonly include only the Stokes portion.

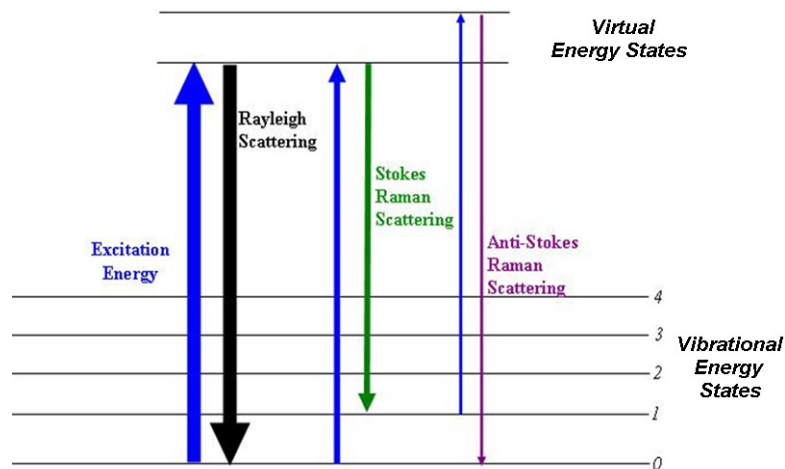


*Fig. 3.9. Schematic representation of the (a) Rayleigh, (b) Stokes Raman and (c) anti-Stokes Raman scattering effect.*

Other photons of potentially different energies,  $h\nu_i$ , will be generated by a polyatomic molecule for each of its  $i$  normal vibrational modes meeting the selection rules (molecule must have anisotropic polarizability) for Raman scattering. By spectrally sorting the Raman scattered photons generated from these Raman-active modes, a highly characteristic vibrational spectrum can be obtained for the molecule under study. In order to make Raman spectra easier to evaluate, frequency or even better wavenumber shifts are usually recorded; the exciting radiation defining the zero of this recorded variable. The wavenumber shift for a Raman band is in fact constant, regardless of the excitation line used (which might affect only the relative intensity of lines), and it directly relates to energy of the vibrational level being probed,  $h\nu_i$ . It is therefore analogous to the vibrational information provided by IR absorption spectroscopy, but complementary to it rather than identical, owing to the different selection rules governing Raman scattering (mandatory change in polarizability) and IR absorption (mandatory change in dipole moment).

Micro-Raman spectrometer consists of a monochromatic source of laser light such as HeNe, Ar/ion, diode or Kr/ion, a standard optical microscope with focusing and collecting objective, a series of mirrors which direct the laser beam towards the sample and collect the returning Raman signal, and a monochromator system that disperses Raman scattered light into its component wavelengths which are detected by a sensitive detector like Photomultiplier tube (PMT) or liquid nitrogen cooled charged couple device (CCD). The wavelength/intensity information is then converted by the complementary software into a wavenumber/intensity plot which is a typical Raman spectrum.

The micro laser Raman instrument employed for the present study was Lab Ram HR 800 with a focal length of 800 mm and having a CCD based monochromator. The laser

wavelength used was 514 nm, from an air cooled Argon ion laser of power 30 mW. The surfaces of exposed specimens were analyzed by placing them on the microscope stage having a long distance 50× objective. The finely powdered glass samples that were taken from the vicinity of the aluminized and oxidized Alloy 690 specimen after the interaction with borosilicate melt were put on a glass slide and kept on the microscope stage of the instrument. Raman spectra were recorded in the range of 230–1000  $\text{cm}^{-1}$  range for specimen surface analysis and that of 100–2000  $\text{cm}^{-1}$  for glass sample analysis using a Peltier cooled charge coupled device (CCD) and 1800 line/mm grating. Depth and spatial resolution of Raman spectroscopy is about 2  $\mu\text{m}$  and spectral resolution is 1  $\text{cm}^{-1}$ .

### **3.5.5 X-ray Photoelectron Spectroscopy (XPS):**

X-ray Photoelectron Spectroscopy (XPS) or Electron Spectroscopy for Chemical Analysis (ESCA) is one of the most powerful surface analytical techniques capable for providing accurate qualitative and quantitative elemental analysis (for all elements but hydrogen and helium), bonding in different chemical states of elements, oxidation state determination of elements, identification of chemical state of the metal oxide films and elemental depth profiling etc [81-83].

XPS involves irradiating a sample with X-rays of a characteristic energy and measuring the energy of flux of electrons leaving the surface [84]. The energy spectrum for the ejected electrons is a combination of an overall trend due to energy loss processes within the sample, transmission characteristics of the spectrometer, and resonance structures that derive from electronic states of the material under analysis. In principle it consists of (a) X-ray source, (b) electronic focusing system, (c) electron energy analyzer, and (d) detector. The schematic of X-ray photoelectron spectroscopy is shown in Fig. 3.10 [84].

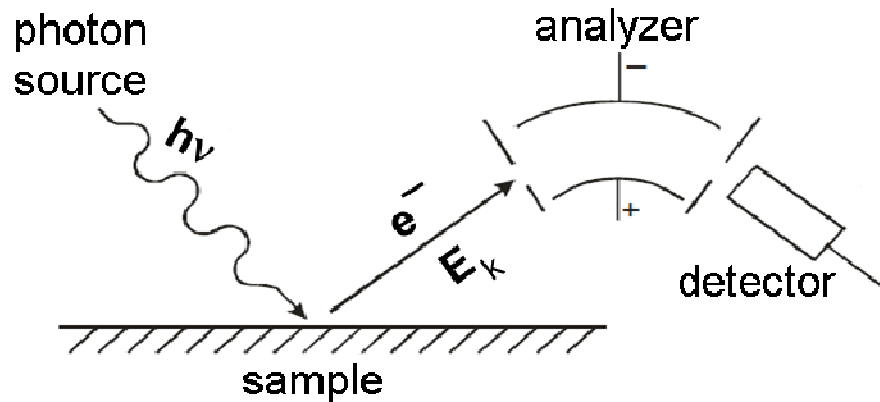


Fig. 3.10. Schematic diagram of X-ray photoelectron spectroscopy.

Since the kinetic energy of the photoelectron is measured, binding energy of emitted electron can be obtained from the following equation:

$$E_{binding} = E_{photon} - (E_{kinetic} + \Phi)$$

Where  $E_{photon}$  is the energy of the X-ray photons being used,  $E_{kinetic}$  is the kinetic energy of the electron as measured by the instrument and  $\Phi$  is the work function dependent on both the spectrometer & the material.

Al  $K\alpha$  (1486.6 eV) and Mg  $K\alpha$  (1253.6 eV) are universally used in laboratory XPS studies. The monochromatic X-ray is generated based on Bragg's relation by diffraction of a crystal for reduced background, narrow peak width, and filtering of satellite peaks. The monochromatized X-ray source is then refocused to the sample surface. Irradiation of the specimen with X-ray causes emission of photoelectrons of discrete energy. This is known as photoelectric effect. Analysis of energies of these photoelectrons emitted from the surface of the specimen is the primary role of XPS. Kinetic energy of the emitted electrons are measured by an electron energy analyzer (spectrometer). Basic function of the spectrometer

is to separate out electrons in a desired band of energies from all other electrons entering the spectrometer with wide range of energies. The most common type of spectrometer used is concentric hemispherical analyzer (CHA). The current reaching the exit slit of the energy analyzer from the energy analyzed electrons is very low, and usually requires electron multiplier for detecting the photoelectrons of different energy. There are two types of electron multiplier currently in use, those are (a) discrete dynode and (b) channel electron multiplier. The current gains from such electron multipliers are within  $10^4$ - $10^8$  range. In the detector, photoelectron spectra directly give the detected electron density versus their binding energy. Identification of elements on the surface is realized with their characteristics peaks appearing on the wide range energy spectrum.

XPS analyses of aluminized and thermally oxidized Alloy 690 specimens prepared using both high and low Al-containing packs, exposed to simulated nuclear waste and sodium borosilicate melt (the same samples used in Raman spectroscopic studies) were carried out using XPS system (SPECS) that employed monochromatic  $AlK\alpha$  X-ray ( $h\nu=1486.74$  eV) radiation as the primary radiation source. The optimum energy resolution of the detector is 0.5 eV. Survey scans over a range of 0 to 1000 eV were recorded for the specimen. The pass energy used for taking survey scan was 25 eV. After identifying the energy spectrum for the elements of interest, detailed high resolution (pass energy–25 eV) scan carried for each element. XPS spectra were recorded for a  $2p_{3/2}$  level of Al, Cr, 2s level of Al and for 1s level of oxygen. The binding energies at the peaks observed in the photoelectron spectra were corrected with the reference to the C1s peak at a binding energy of 284.6 eV. The XPS analyses of sodium borosilicate glass that interacted with aluminized (using high Al-containing pack) and thermally oxidized Alloy 690 specimens were carried

out in an electron spectrometer using a monochromatic MgK $\alpha$  X-rays ( $h\nu = 1253.6$  eV) as the primary radiation source. The energy resolution of detector is 0.5 eV. The energy spectra of the photoelectrons were analyzed by VG Microtech Clam-2 analyzer. The energy resolution of detector was calibrated using standard sample of pure silver. Sodium borosilicate glass that interacted with aluminized (using low Al-containing pack) and thermally oxidized Alloy 690 specimen was analyzed using the XPS system (SPECS) that used the non-monochromatic MgK $\alpha$  X-rays ( $h\nu=1253.6$  eV) as radiation source. Unreacted glass was also analyzed for the sake of comparison. Survey scans were recorded over the region of 0 to 1000 eV for the glass samples. The resolution of the detector is 0.9 eV. The glass samples were powdered and put on a glass slide using non-reacting glue and used for analysis. The XPS spectra were recorded for 2p $_{3/2}$  level of Si, Ti and Fe, for 1s level of B and O. The spectra were smoothed by averaging the raw data, wherever it was necessary. For peak fitting, the functions Gaussian and Lorentzian were used. It was observed that, Gaussian fitting provided better fitting compared to the combination of Gaussian and Lorentzian functions.



# *Interaction of aluminized (using high Al-containing pack) and oxidized Alloy 690 with simulated nuclear waste and sodium borosilicate melts*

---

---

### 4.1 Introduction

This chapter is devoted to study the interaction of pack aluminized (high Al-containing pack; 10 wt.% Al) and thermally oxidized Alloy 690 substrates with simulated nuclear waste solution at 373 K for 216 hours. Exposure time and temperature was selected by considering the real plant scale vitrification process. In actual vitrification process, feeding and evaporation are performed between 373–378 K and 378–393 K respectively. It is, therefore, decided to select the exposure temperature as 373 K. As the vitrification process is carried out in a batchwise manner, where typical duration of exposure is close to 216 hours, the exposure experiments in the present study were carried out for longer durations (216 hours).

Interaction of coated specimens with sodium borosilicate melt at 1248 K for 192 hours is also discussed in this chapter. In actual plant-scale operations, pouring temperature of borosilicate melt generally fall between 1223–1273 K and hence present experiments were performed at 1248 K. Borosilicate melt was soaked for 10 h for homogenization, however, to

replicate the effect of repeated cyclic process, experiments were carried out for longer duration (192 hours). The exposed specimens were characterized by Raman spectroscopy, XPS and EPMA techniques. In order to compare the performance of coatings, bare Alloy 690 substrates were also exposed to similar environments.

## **4.2 Experimental Methods**

Alloy 690 specimens, having dimensions 10 mm × 10 mm × 5 mm, were aluminized with high Al-containing pack (10 wt.% Al powder, 5 wt.% NH<sub>4</sub>Cl and 85 wt.% Al<sub>2</sub>O<sub>3</sub> powder), soaked for 10 h at 1273 K and subsequently heat treated at 1273 K for 4 h, to grow an oxide layer at the surface. These heat treated specimens were distributed into two sets viz. Set A and Set B. The specimens of set A were exposed to simulated high-level nuclear liquid waste (nitrate-based environment) solution at 373 K for a period of 216 h, and specimens of Set B were exposed to sodium borosilicate melt at 1248 K for a period of 192 h. At the end of the exposure, the specimens of Set A were removed from the flask, cleaned, dried and characterized without any surface modification, using Raman spectroscopy, XPS and EPMA techniques. After exposure of Set B specimens in borosilicate melt, adhered glass was removed from specimens. Surfaces of exposed specimens (after removal of adhering glass) were characterized using Raman spectroscopy, XPS and EPMA techniques. Linear baseline corrections have been carried out on all the data acquired for the XPS spectra in order to eliminate the background. The positions of all the XPS peaks in the spectrum were assigned on the basis of Gaussian model of peak fitting. The detailed experimental procedure and the characterization techniques have already been discussed in detail in Chapter 3. For the purpose of comparison of results, samples of bare Alloy 690 substrate (without aluminization

and oxidation) were exposed in simulated nuclear waste and sodium borosilicate melt under similar experimental conditions.

### 4.3 Results

#### 4.3.1 Microstructure of aluminide coatings

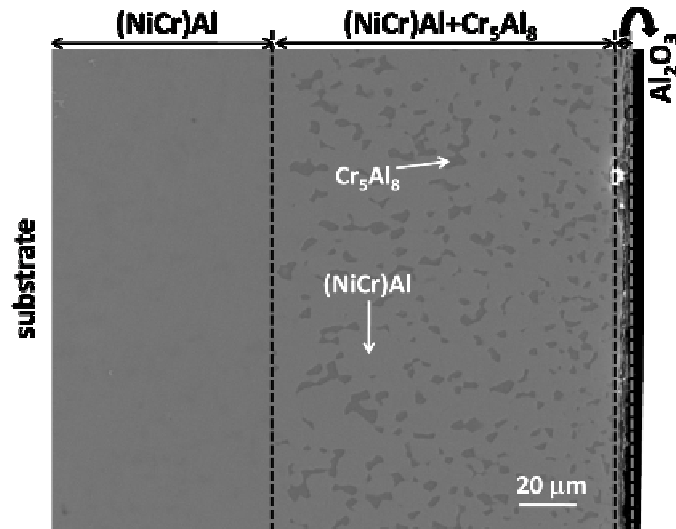


Fig. 4.1. SEM micrograph showing the cross-sectional view of aluminized (using high Al-containing pack) and thermally oxidized Alloy 690 specimen.

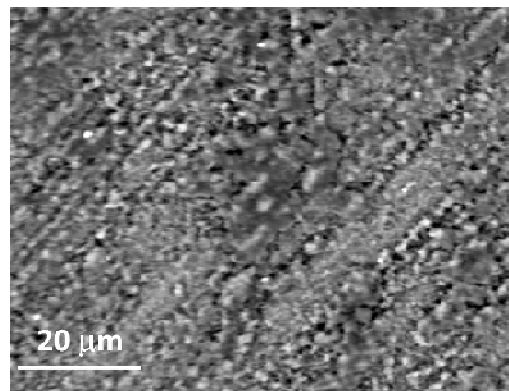


Fig. 4.2. Surface image (BSE) of aluminized (using high Al-containing pack) and thermally oxidized Alloy 690 specimen.

Typical microstructure along the cross-section of aluminized and thermally oxidized Alloy 690 substrate is shown in Fig. 4.1. The microstructure reveals presence of multilayered aluminides. Chemical composition of multilayers was determined by EDS point analyses. A continuous interdiffusion layer (composition: 26.42Al-0.62Ti-37.40Cr-6.83Fe-28.73Ni, at.%) was observed very close to the substrate. It was followed by (Ni,Cr)Al type layer (composition: 56.25Al-7.82Cr-4.69Fe-31.24Ni, at.%) and (Ni,Cr)Al+Cr<sub>5</sub>Al<sub>8</sub> type layers (composition of Cr<sub>5</sub>Al<sub>8</sub>: 61.14Al-0.28Ti-30.36Cr-3.68Fe-4.54Ni, at.%). A continuous layer of 2 μm thick Al<sub>2</sub>O<sub>3</sub> was observed at the topmost surface. Chemical composition of Al<sub>2</sub>O<sub>3</sub> layer as revealed by EDS point analyses shows typical as: 59.86O-35.30Al-1.57Cr-0.89Fe-2.38Ni (at.%). Surface microstructure of aluminized and thermally oxidized Alloy 690 substrate is also shown in Fig. 4.2.

## **4.3.2 Interaction of aluminized and thermally oxidized Alloy 690 specimen**

### **4.3.2.1 Specimens exposed to simulated nuclear waste solution (Set A)**

Raman spectrum (Fig. 4.3) of specimens of set A exposed to simulated nuclear waste medium predominantly shows the presence of aluminium oxide (Al<sub>2</sub>O<sub>3</sub>) bands at 649 cm<sup>-1</sup> and 255 cm<sup>-1</sup> [85-90]. A shoulder at 692 cm<sup>-1</sup> corresponds to NiCr<sub>2</sub>O<sub>4</sub> mixed oxide and the band observed at 906 cm<sup>-1</sup> indicates the presence of nickel oxide (NiO) [91-94]. The bands at 489 cm<sup>-1</sup> and 310 cm<sup>-1</sup> correspond to NiFe<sub>2</sub>O<sub>4</sub> mixed oxide and Cr<sub>2</sub>O<sub>3</sub> respectively [91], while the weak band at 881 cm<sup>-1</sup> shows the presence of mixed oxides of Cr<sup>+3</sup> and Cr<sup>+6</sup> [95].

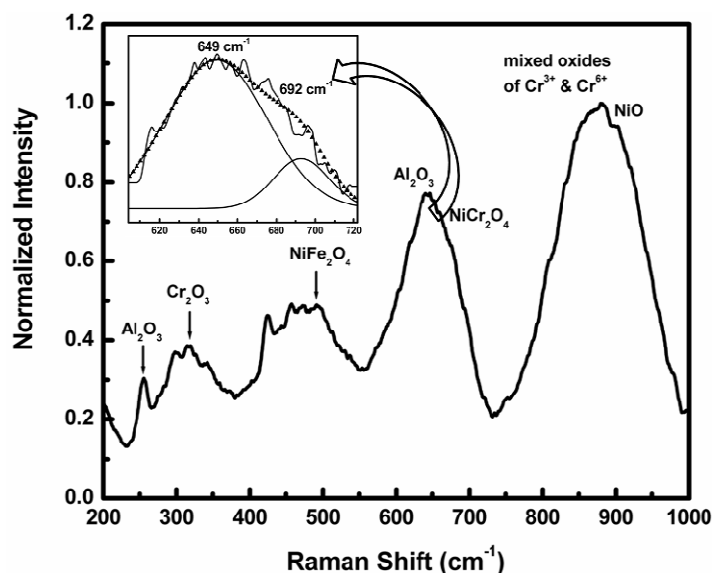


Fig. 4.3. Normalized Raman spectra of specimens of Set A exposed to simulated nuclear waste solution. Gaussian fit of the region 600–720  $\text{cm}^{-1}$  is shown in inset.

Fig. 4.4 shows the XPS survey spectrum and Figs. 4.5 (a & b) show  $\text{Al}2\text{p}_{3/2}$  and  $\text{O}1\text{s}$  high resolution spectra, respectively of specimens of Set A exposed to simulated high level nuclear waste solution for 216 hours. Two peaks are observed in  $\text{Al}2\text{p}_{3/2}$  XPS spectrum. The first peak at 72.41 eV corresponds to elemental aluminium ( $\text{Al}^0$ ), and the second strong peak occurring at 74.33 eV corresponds to  $\text{Al}_2\text{O}_3$  [96-101] (Fig. 4.5a). The peak at 531.6 eV in the  $\text{O}1\text{s}$  XPS spectrum assigned to  $\text{Al}_2\text{O}_3$  [98,101,102] as evident from Fig. 4.5b.

Back-scattered electron (BSE) image of specimens of Set A that exposed to simulated nuclear waste solution is shown in Fig.4.6. The BSE image reveals two different phases, which based upon the image contrast, could be identified as a whitish phase and a dark phase, as shown in Fig. 4.6. To find the compositional difference between the two phases, Wavelength dispersive spectroscopy (WDS) analysis was carried out on each phase. Representative WDS spectra obtained from both whitish and dark phases are shown in Fig. 4.7 and 4.8.

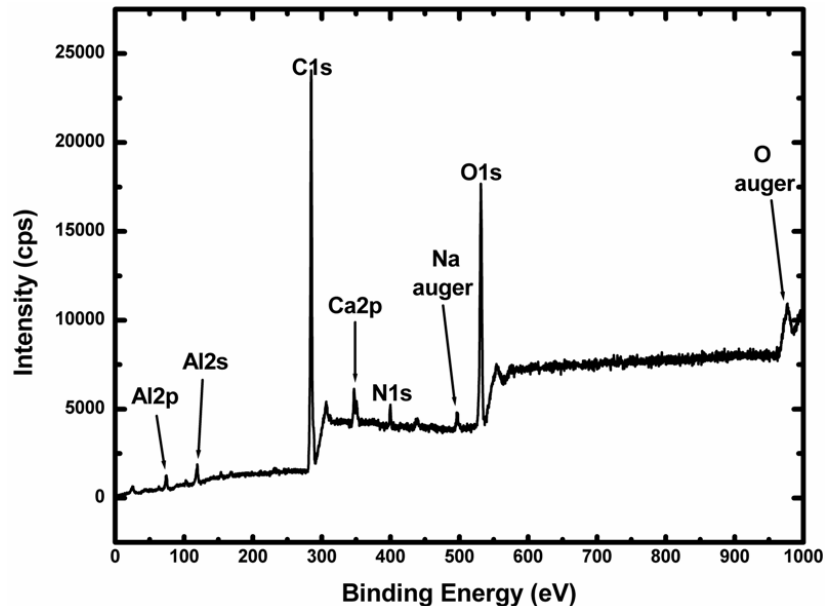


Fig. 4.4. XPS survey spectrum recorded on the surface of specimens of Set A exposed to simulated high level nuclear waste solution.

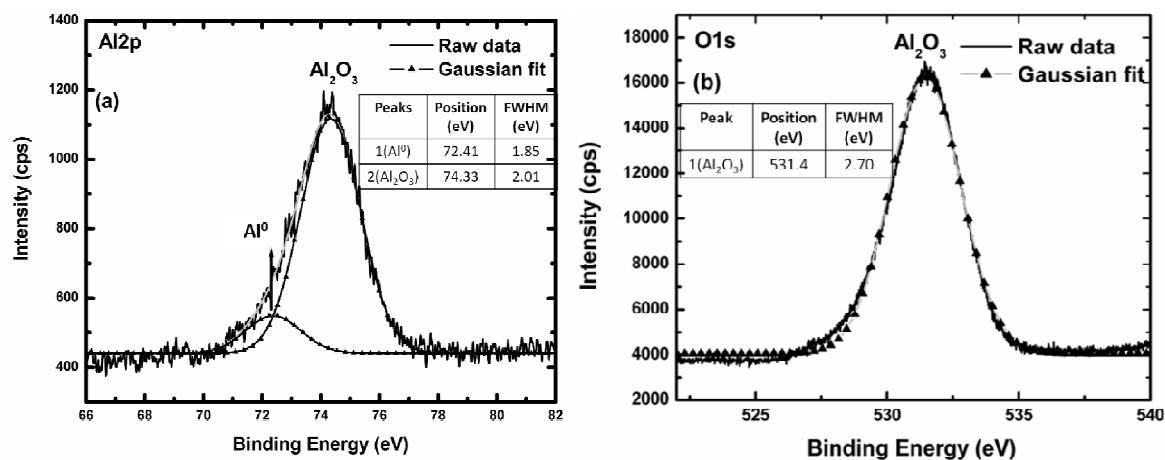


Fig. 4.5. XPS spectra recorded on the surface of specimens of Set A exposed to simulated high level nuclear waste, (a) Al<sub>2</sub>p spectrum reveals the presence of elemental aluminium and Al<sub>2</sub>O<sub>3</sub>, (b) O<sub>1</sub>s spectrum showing Al<sub>2</sub>O<sub>3</sub>.

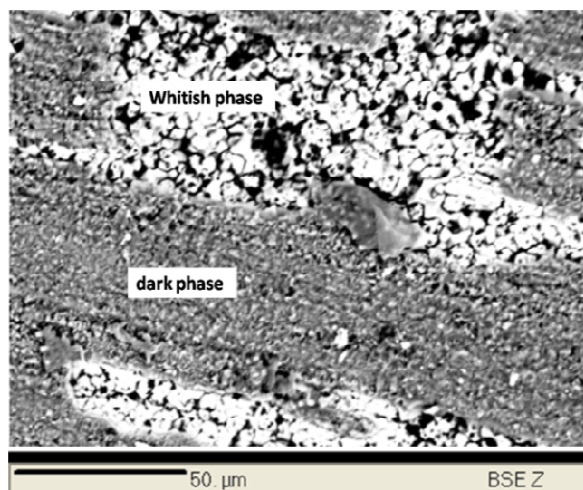


Fig. 4.6. Representative back-scattered electron (BSE) image of specimens of Set A exposed to simulated nuclear waste solution.

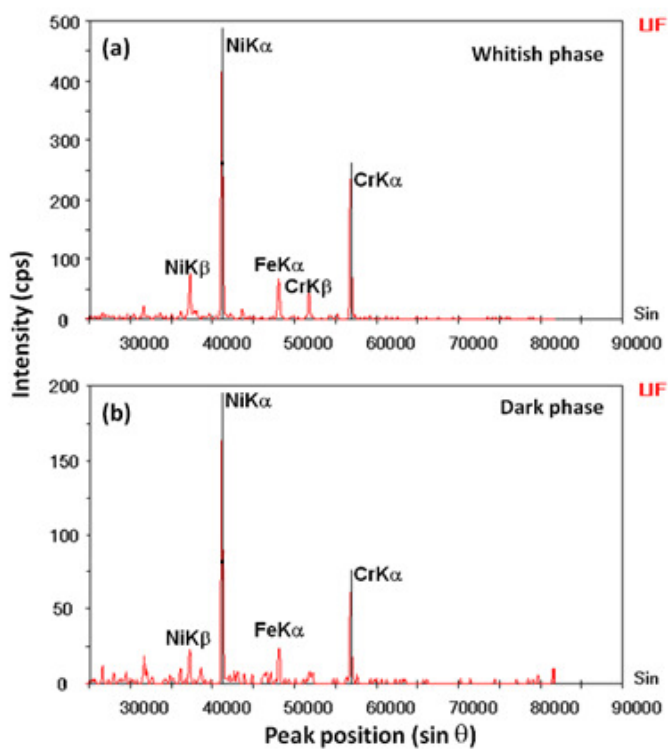
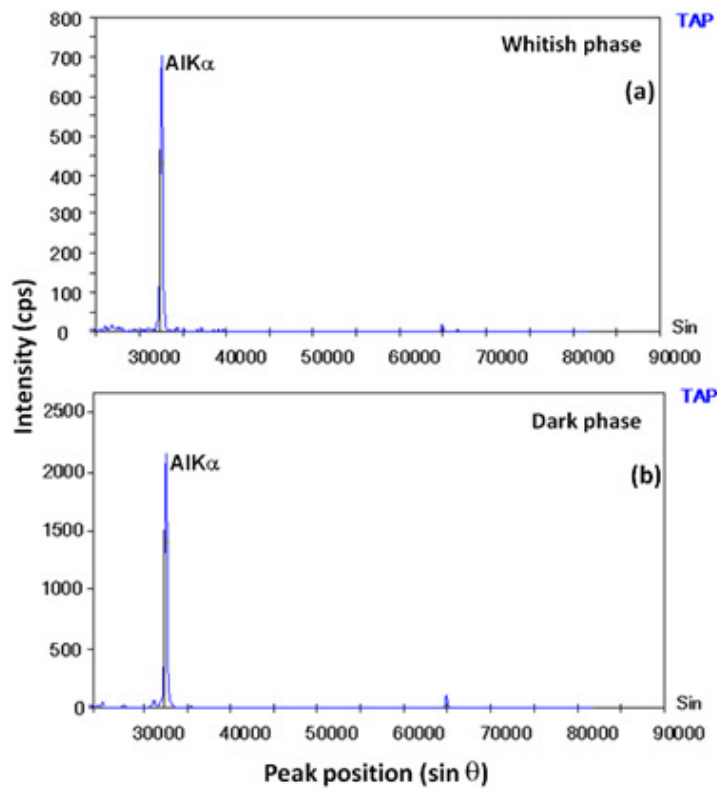


Fig. 4.7. X-ray spectra (Lithium fluoride crystal, LiF) showing the variations in Ni, Cr and Fe X-ray intensities on the surface of specimens of Set A exposed to simulated nuclear waste solution (a) whitish phase and (b) dark phase.

From these spectra it can be observed that  $NiK\alpha$ ,  $CrK\alpha$  and  $FeK\alpha$  intensities are high in whitish phase; whereas higher  $AlK\alpha$  intensity is observed in the dark phase. X-ray mapping on the surface of exposed specimens were carried out and  $AlK\alpha$ ,  $NiK\alpha$ ,  $CrK\alpha$  and  $FeK\alpha$  X-ray images are shown in Fig. 4.9 (a–d).  $AlK\alpha$  X-ray image shows the uniform distribution of aluminium over the dark phase, while  $NiK\alpha$  and  $CrK\alpha$  images demonstrate that the whitish phase is composed of two oxides; one rich in Ni and another in Cr. Based on this observation, the presence of  $NiCr_2O_4$  phase as shown in Fig. 4.3, could be identified as  $NiO$  and  $Cr_2O_3$ .



*Fig. 4.8. X-ray spectra (Thallium acid phthalate crystal, TAP) showing  $AlK\alpha$  X-ray intensities on the surface of specimens of Set A exposed to simulated nuclear waste solution (a) whitish phase and (b) dark phase.*

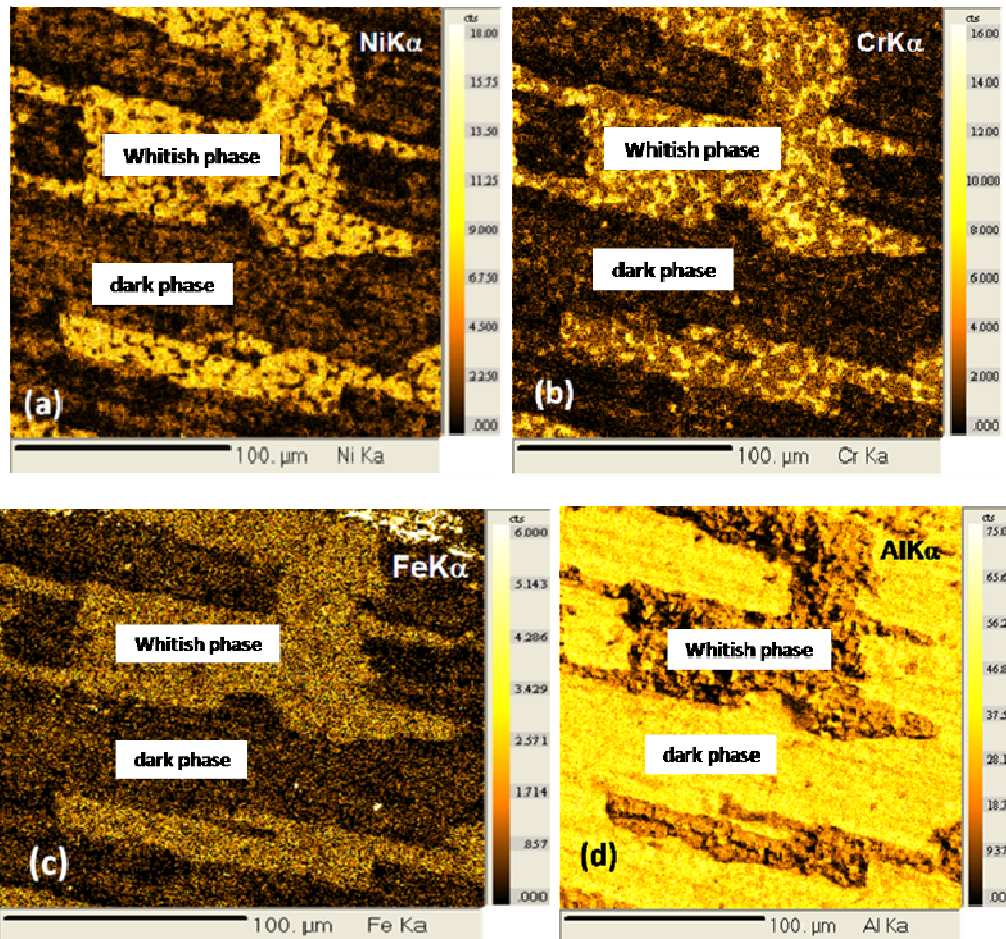
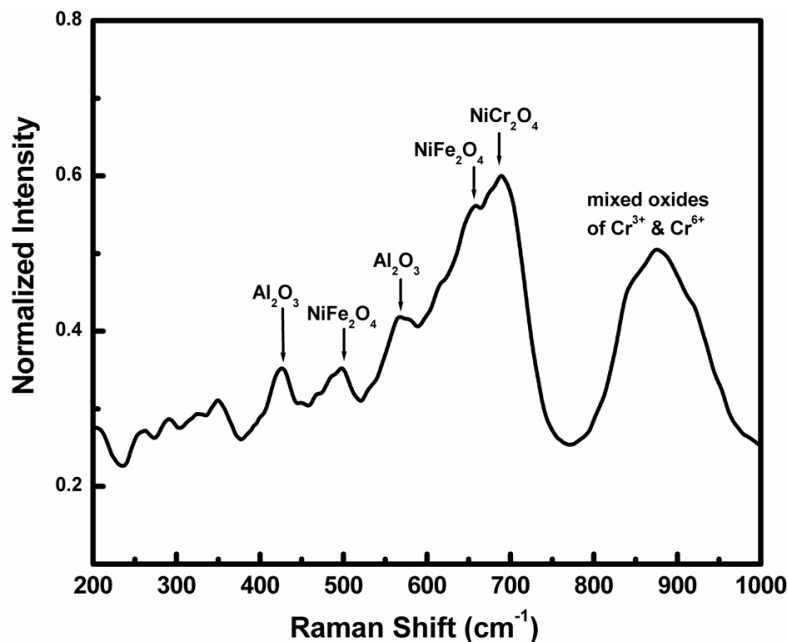


Fig. 4.9. X-Ray images for (a) NiKa, (b) CrKa, (c) FeKa and (d) AlKa of surface of specimens of Set A exposed to simulated nuclear waste solution revealing the distribution of different elements.

#### 4.3.2.2 Specimens exposed to sodium borosilicate melt (Set B)

Fig. 4.10 shows the Raman spectrum of specimens of Set B exposed to sodium borosilicate glass. A strong band at  $687\text{ cm}^{-1}$  corresponds to  $\text{NiCr}_2\text{O}_4$  mixed oxide [91,92] and the band at  $500\text{ cm}^{-1}$  and a shoulder at  $656\text{ cm}^{-1}$  correspond to the presence of  $\text{NiFe}_2\text{O}_4$  mixed oxide [91,103-105]. A broad band appearing at  $875\text{ cm}^{-1}$  corresponds to the mixture of

$\text{Cr}^{3+}$  and  $\text{Cr}^{6+}$  oxides [106]. The Raman spectrum also shows the bands corresponding to  $\text{Al}_2\text{O}_3$  at  $430\text{ cm}^{-1}$  and  $571\text{ cm}^{-1}$  [85,89,107].



*Fig. 4.10. Normalized Raman spectra of specimens of Set B exposed to sodium borosilicate melt.*

The XPS survey spectrum and high resolution spectra recorded for the  $2p_{3/2}$  level of Al and 1s level of O of the specimens of Set B exposed to sodium borosilicate melt for 192 hours are shown in Figs. 4.11 and 4.12 respectively. For  $\text{Al}2p_{3/2}$  XPS spectrum, two XPS peaks noticed at 72.6 eV and 74.9 eV correspond to elemental aluminium ( $\text{Al}^0$ ) [96] and  $\text{Al}_2\text{O}_3$  [99] respectively, as evident from Fig. 4.12a. Two peaks were observed in O1s XPS spectrum. The first O1s peak occurred at 528.6 eV corresponding to a value that is lower than that of NiO [96, 108] whereas, the second one occurred at 531.6 eV assigned to  $\text{Al}_2\text{O}_3$  [102] as shown in Fig. 4.12b. For Ni2p region, the peak obtained at 856.0 eV corresponding to a value that is slightly higher than that of NiO [109-111] as shown in Fig. 4.12c.

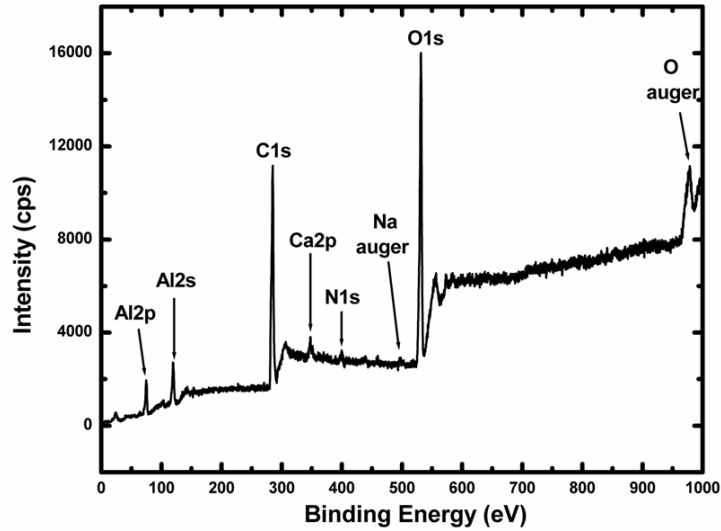


Fig. 4.11. XPS survey spectrum recorded on the surface of specimens of Set B exposed to sodium borosilicate melt.

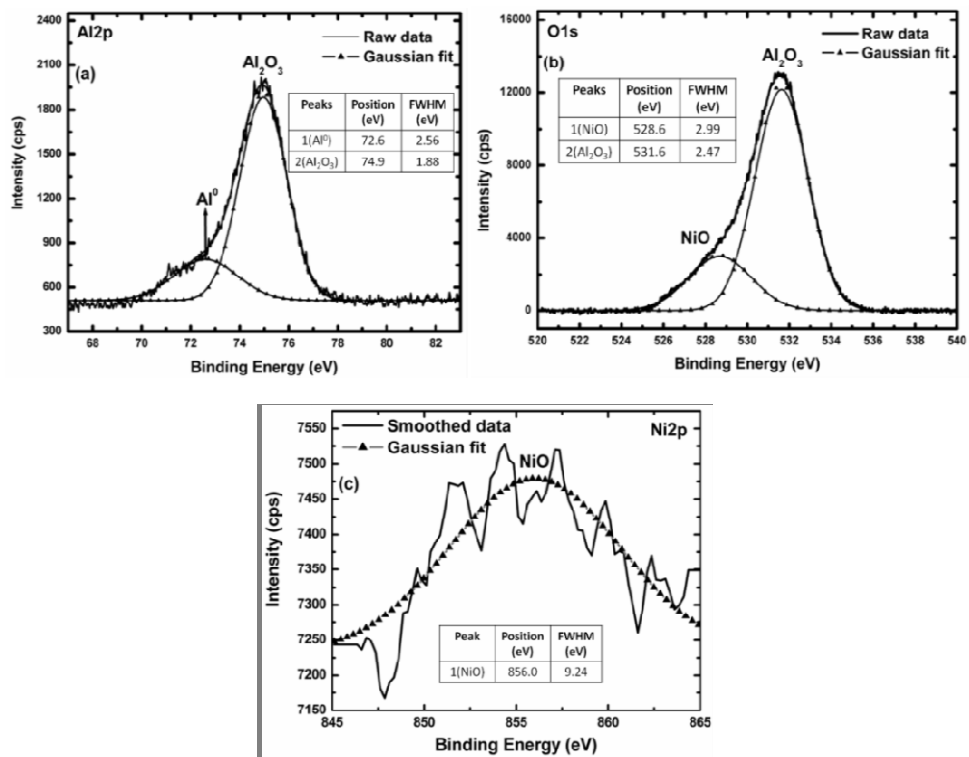


Fig. 4.12. XPS spectra recorded on the surface of specimens of Set B exposed to sodium borosilicate melt, (a) Al<sub>2</sub>p spectrum showing elemental aluminium and Al<sub>2</sub>O<sub>3</sub>, (b) O1s spectrum reveals NiO and Al<sub>2</sub>O<sub>3</sub> and (c) Ni<sub>2</sub>p spectrum showing NiO.

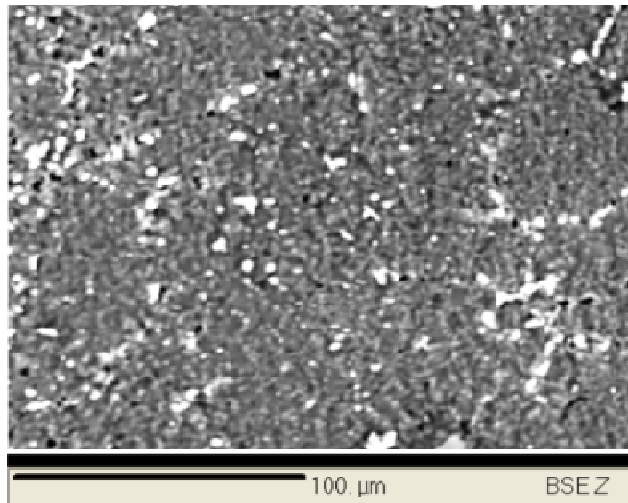


Fig. 4.13. Representative back-scattered electron (BSE) image of specimens of Set B exposed to sodium borosilicate melt.

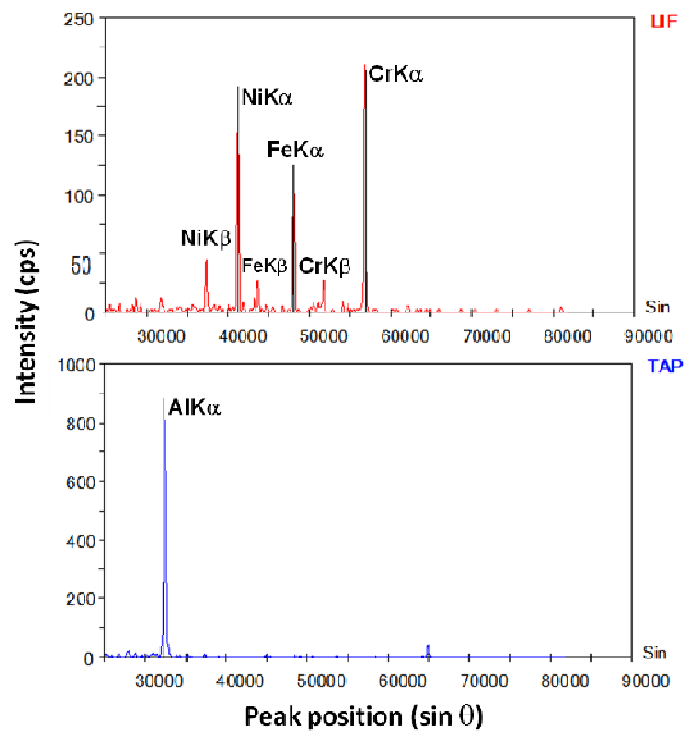
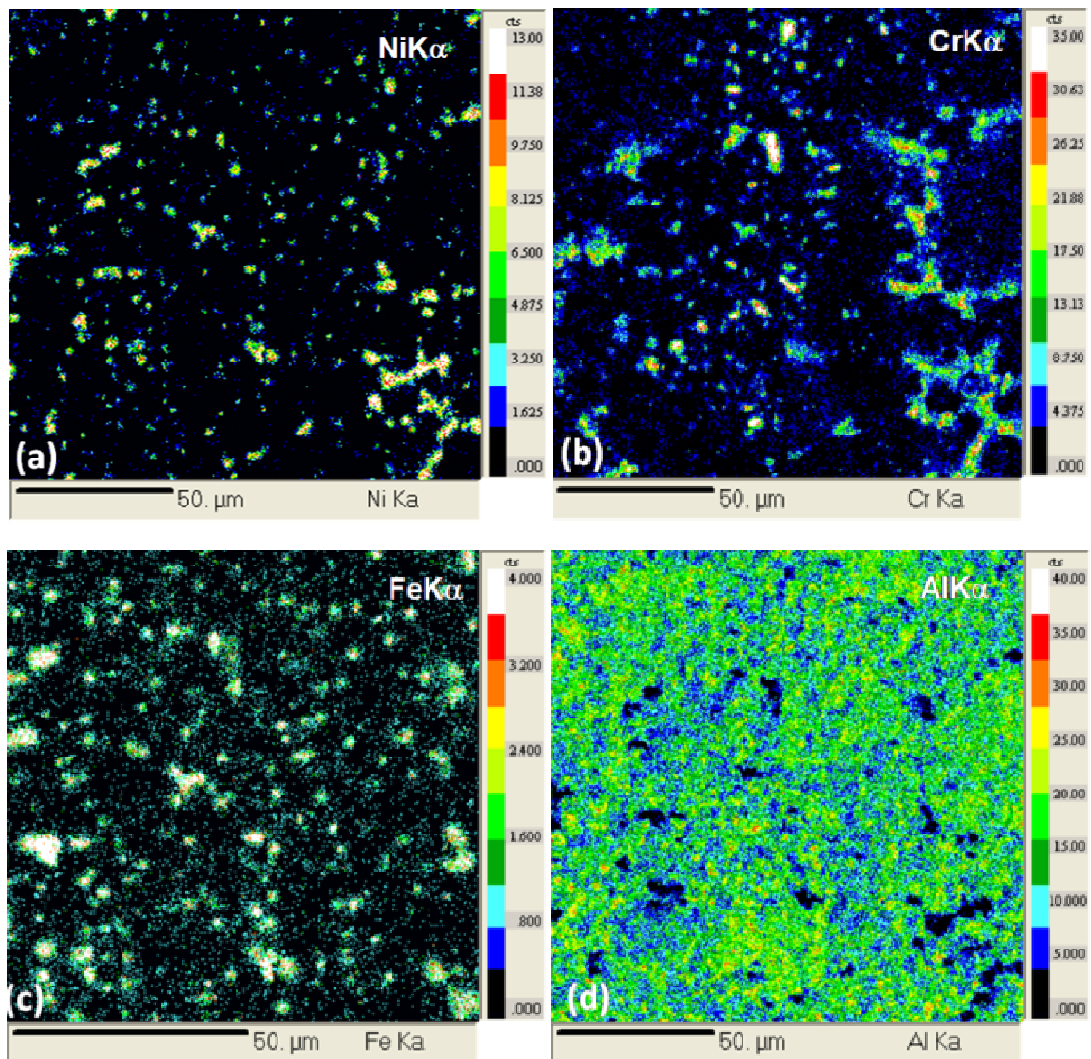


Fig. 4.14. X-ray spectra (LiF & TAP crystal) showing Ni, Cr, Fe and Al X-ray peaks on the surface of specimens of Set B exposed to sodium borosilicate melt. It reveals the enrichment of Al and depletion of Cr on the surface.



*Fig. 4.15. X-Ray images for (a) NiK $\alpha$ , (b) CrK $\alpha$ , (c) FeK $\alpha$  and (d) AlK $\alpha$  of surface of specimens of Set B exposed to sodium borosilicate melt revealing the distribution of different elements.*

EPMA analyses of specimens of Set B that was exposed to sodium borosilicate melt indicated a uniform microstructure as shown in Fig. 4.13. WDS analysis on the surface of the exposed specimen was carried out and the spectra are given in Fig. 4.14. It is observed that, Ni, Cr and Fe peaks were obtained at lower intensities, whereas high intensity peak was

obtained for  $AlK\alpha$ . Elemental X-ray images for  $NiK\alpha$ ,  $FeK\alpha$  and  $AlK\alpha$  were recorded on the surface of the exposed specimen and these are illustrated in Fig. 4.15 (a–d). X-ray images and WDS analyses clearly reveal that, the surface of the exposed specimen is enriched with aluminium along with small amounts of nickel, chromium and iron [11,112].

### 4.3.3 Interaction of bare Alloy 690 substrate

#### 4.3.3.1 Specimens exposed to simulated nuclear waste solution

Raman spectrum (Fig. 4.16) of bare Alloy 690 substrate, which was exposed to simulated nuclear waste solution, shows a strong and broad band around  $660\text{ cm}^{-1}$  indicating the existence of oxide of iron ( $\gamma\text{-Fe}_2\text{O}_3$ ) [106]. The weak bands obtained at  $540\text{ cm}^{-1}$  and  $910\text{ cm}^{-1}$  correspond to  $\text{Cr}_2\text{O}_3$  and  $\text{NiO}$  respectively [91,93,94,113-115]. The band observed at  $872\text{ cm}^{-1}$  can be assigned to mixed oxides of  $\text{Cr}^{+3}$  and  $\text{Cr}^{+6}$  [106].

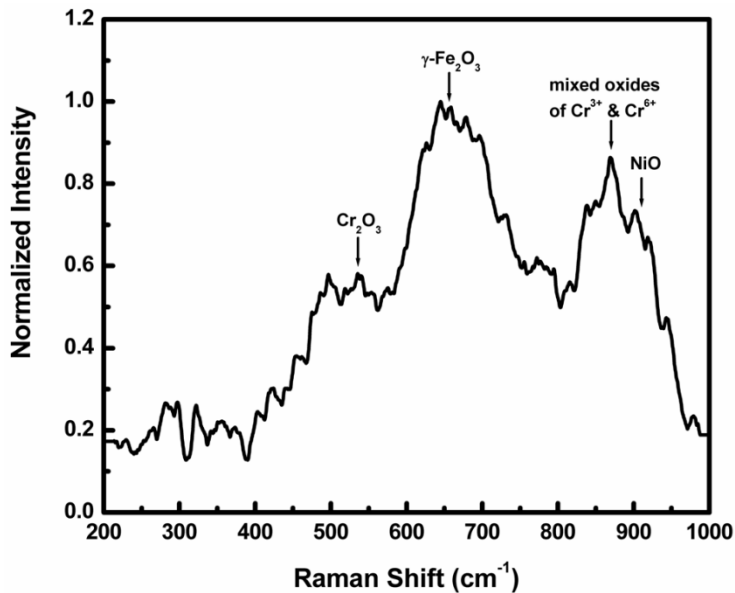
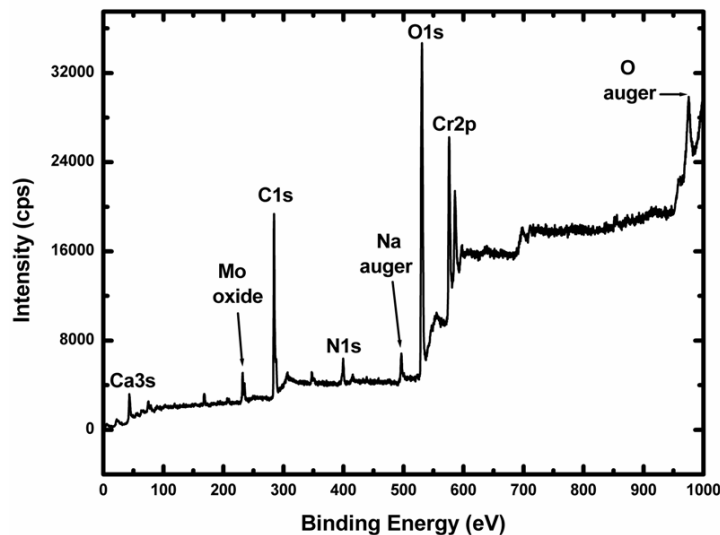


Fig. 4.16. Normalized Raman spectra of Alloy 690 bare substrate exposed to simulated nuclear waste solution.

For the Alloy 690 bare substrate, which was exposed to simulated high level nuclear waste solution for 216 hours, XPS survey spectrum (Fig. 4.17) and high resolution spectra recorded for the  $2p_{3/2}$  level of Ni and Cr, and the  $1s$  level of O. Two XPS peaks were noticed for  $Ni2p_{3/2}$  spectrum (Fig. 4.18a). The first  $Ni2p_{3/2}$  peak occurred at 851.7 eV corresponding to a value that is close to that of elemental nickel ( $Ni^0$ ) [108,116] whereas, the second one occurred at 855.6 eV corresponding to a value that is slightly higher than that of NiO [109-111]. For chromium, XPS peaks noticed at 575.6 eV corresponding to a value that is slightly higher than that of elemental chromium ( $Cr^0$ ) and at 576.6 eV ( $2p_{3/2}$ ) along with a satellite peak at 586.3 eV ( $2p_{1/2}$ ) indicating the presence of  $Cr_2O_3$  [117-119] as shown in Fig. 4.18b. The O1s spectrum obtained as a combination of two peaks. The first peak observed at 529.6 eV assigned to NiO [96,108] and the second one noticed at 531.1 eV corresponds to a value that is higher than that of chromium oxide [116,118] as evident from Fig. 4.18c.



*Fig.4.17. XPS survey spectrum recorded on the surface of Alloy 690 bare substrate exposed to simulated high level nuclear waste solution.*

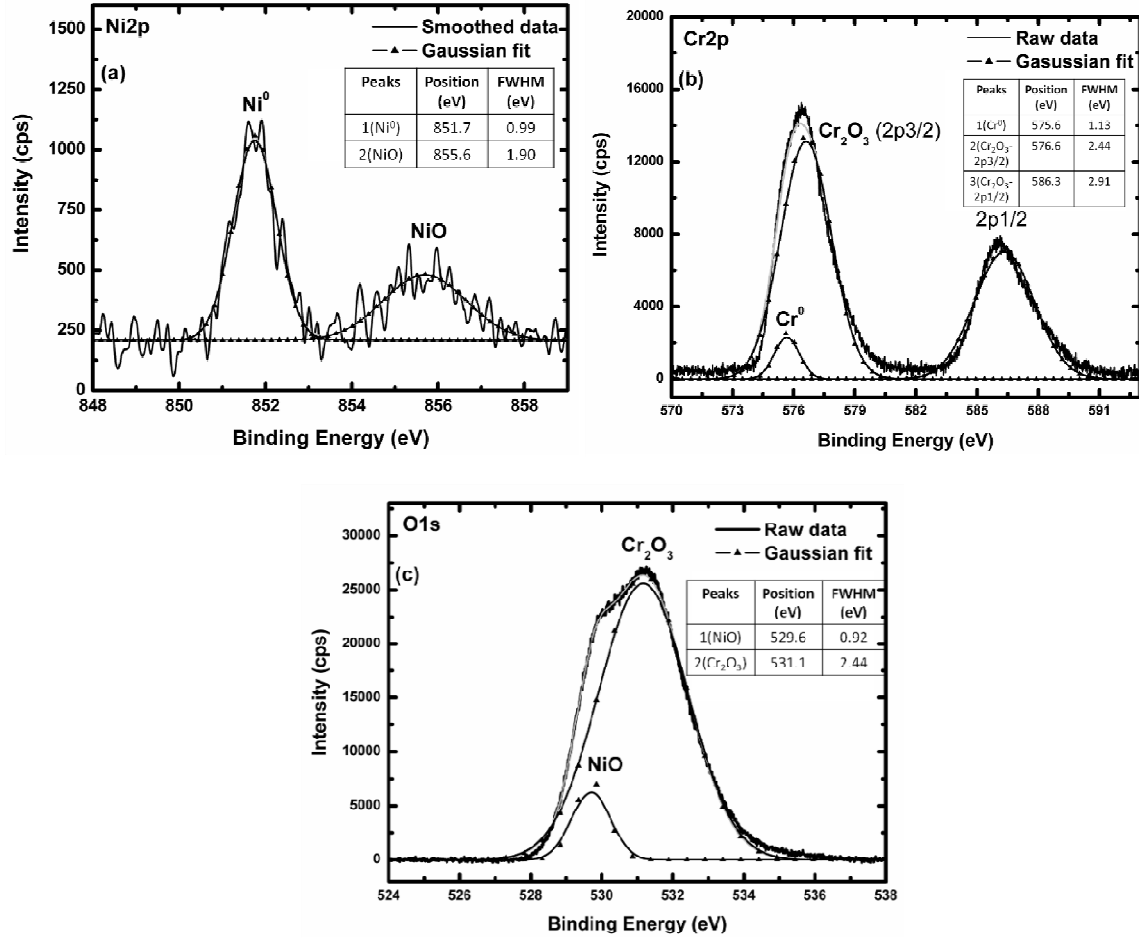


Fig. 4.18. XPS spectra recorded on the surface of Alloy 690 bare substrate exposed to simulated nuclear waste solution, (a) Ni2p spectrum, presence of Ni<sup>0</sup> and NiO are visible, (b) Cr2p spectrum, reveals elemental chromium and Cr<sub>2</sub>O<sub>3</sub> and (c) O1s spectrum shows Cr<sub>2</sub>O<sub>3</sub> and NiO.

Representative WDS spectrum obtained from the bare surface of the Alloy 690 exposed to simulated nuclear waste solution is shown in Fig. 4.19. The characteristic  $K\alpha$  and  $K\beta$  peaks of Ni, Cr and Fe on the specimen shows the presence of Ni, Cr and Fe on the surface of the specimen [44].

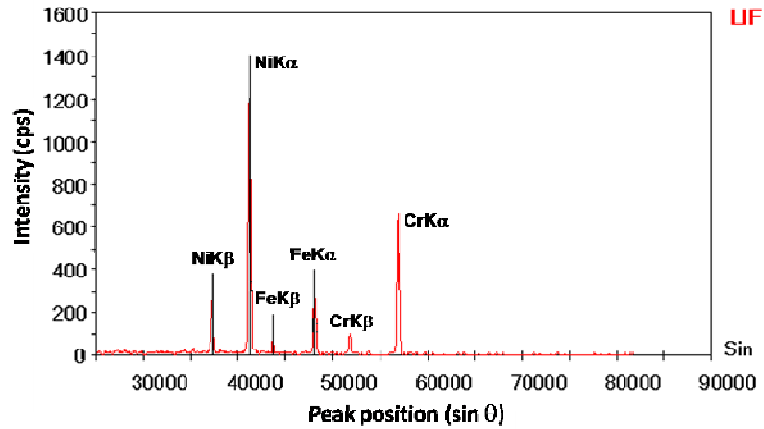


Fig. 4.19. X-ray spectrum (LiF crystal) showing the characteristic Ni, Cr and Fe X-ray peaks on the surface of Alloy 690 bare substrate exposed to simulated nuclear waste solution.

#### 4.3.3.2 Specimens exposed to sodium borosilicate melt

Fig. 4.20 shows Raman spectrum of bare Alloy 690 substrate, which was exposed to sodium borosilicate glass. The strong band at  $558\text{ cm}^{-1}$  and bands at  $305\text{ cm}^{-1}$ ,  $355\text{ cm}^{-1}$  and  $621\text{ cm}^{-1}$  corresponding to  $\text{Cr}_2\text{O}_3$  vibrations [91,113-115,120]. The medium strong band at  $694\text{ cm}^{-1}$  corresponds to  $\text{NiCr}_2\text{O}_4$  mixed oxide while the bands at  $399\text{ cm}^{-1}$  and  $656\text{ cm}^{-1}$  correspond to  $\text{NiO}$  and  $\text{NiFe}_2\text{O}_4$  mixed oxides, respectively [91,92,103]. A broad band at  $874\text{ cm}^{-1}$  belongs to the vibrations of mixed oxides of  $\text{Cr}^{+3}$  and  $\text{Cr}^{+6}$  [106].

Fig. 4.21 shows the XPS survey spectrum and Figs. 4.22 (a & b) show the high resolution spectra for the  $2p_{3/2}$  level of Cr and  $1s$  level of O for the Alloy 690 substrate, recorded on Alloy 690 bare substrate that was exposed to sodium borosilicate melt for 192 hours. A peak at a binding energy value of  $522.4\text{ eV}$  in the survey spectrum seems to have occurred due to the insulating nature of some small portion of the oxide film. For chromium, two  $\text{Cr}2p_{3/2}$  XPS peaks noticed (Fig. 4.22a). The first  $\text{Cr}2p_{3/2}$  peak occurred at  $578.4\text{ eV}$  corresponding to a value that is higher than that of chromium oxide [117-119] and the second

peak occurred at 580.9 eV assigned to  $\text{CrO}_3$  [96]. For O1s region (Fig. 4.22b), the peak noticed at 531.5 eV corresponding to a value that is lower than that of chromium oxide [116,118]. The findings of all the spectra are summarized in Table-4.1.

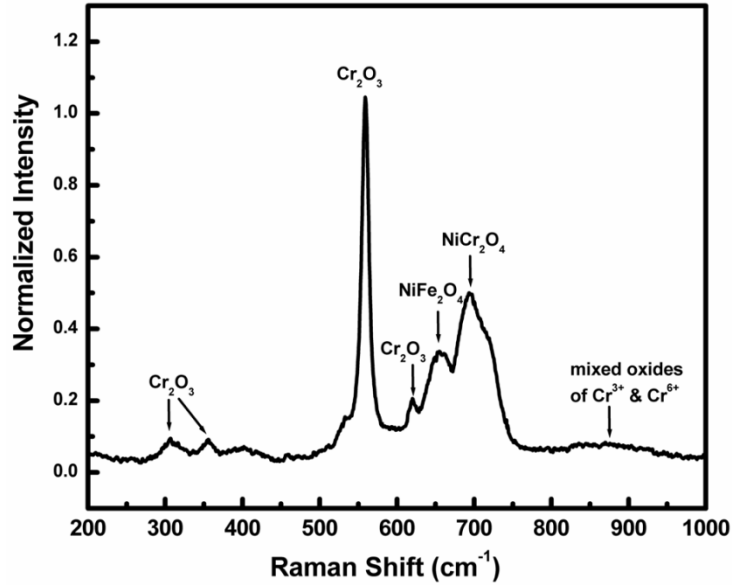


Fig. 4.20. Normalized Raman spectra of bare Alloy 690 bare substrate exposed to sodium borosilicate melt.

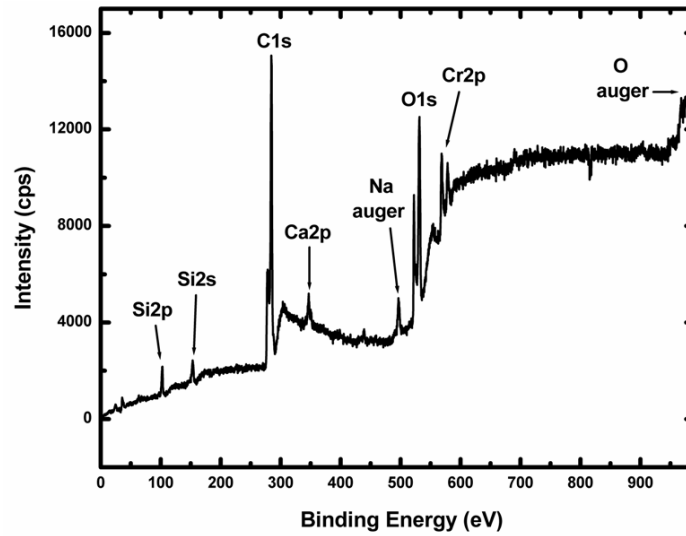


Fig. 4.21. XPS survey spectrum recorded on the surface of Alloy 690 bare substrate exposed to sodium borosilicate melt.

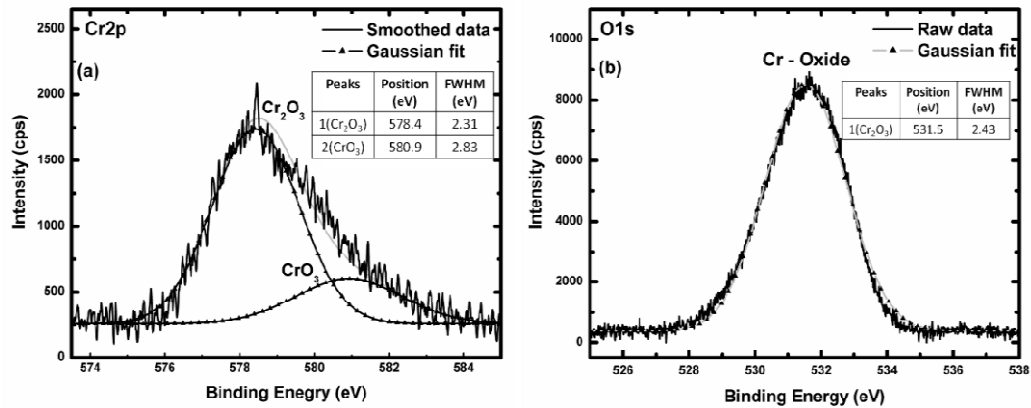


Fig. 4.22. XPS spectra recorded on the surface of Alloy 690 bare substrate exposed to sodium borosilicate melt, (a) Cr2p spectrum, Cr<sub>2</sub>O<sub>3</sub> and CrO<sub>3</sub> are visible and (b) O1s spectrum reveals Cr-oxide.

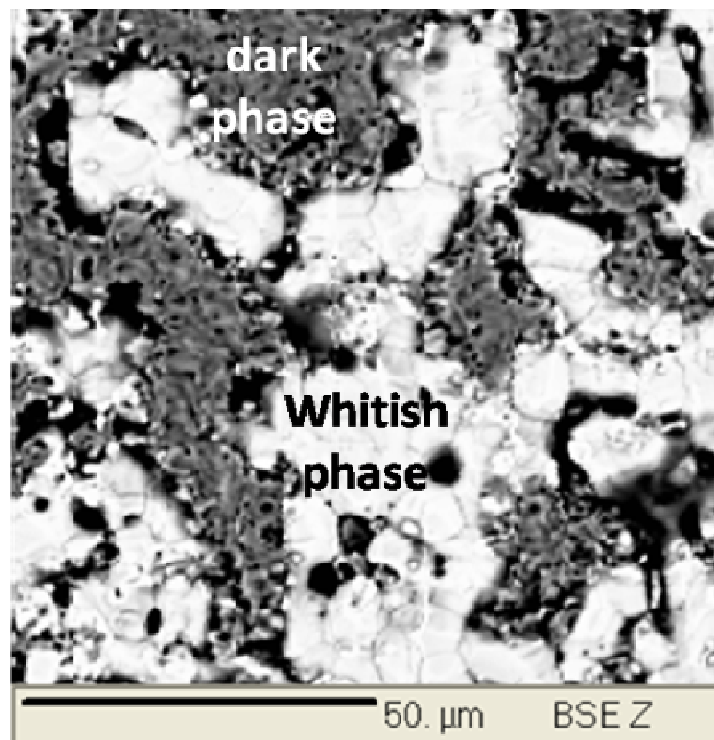
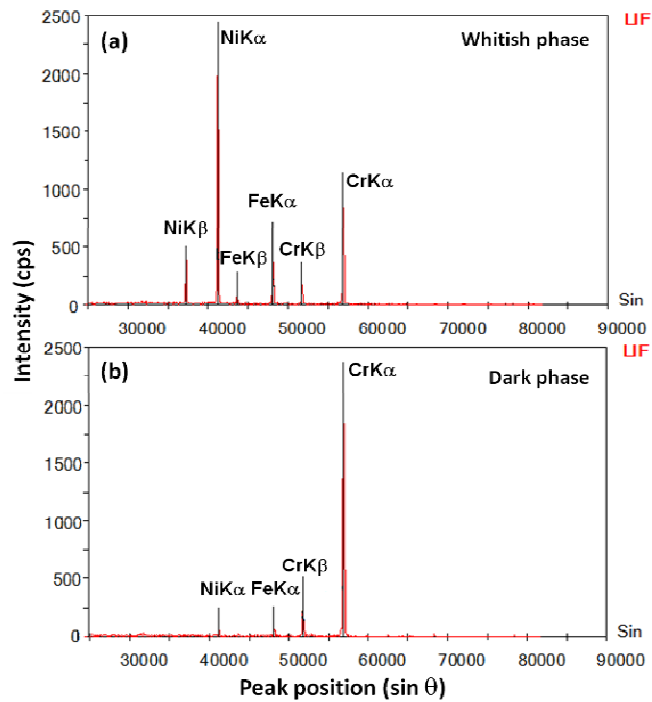


Fig. 4.23. Representative back-scattered electron (BSE) image of Alloy 690 bare substrate exposed to sodium borosilicate melt showing a whitish phase and dark phase.

EPMA analyses of the substrate of Alloy 690 that was exposed to sodium borosilicate melt, using Back-scattered electron (BSE) image analysis indicated the two different phases based upon the image contrast, a whitish phase and dark phase as shown in Fig. 4.23. WDS spectra of whitish phase clearly giving the high intensity peak for nickel and less intensity peak for iron, whereas that of dark phase indicated a high intense peak correspond to chromium as shown in Fig. 4.24.



*Fig. 4.24. X-ray spectra (LiF crystal) showing the variations in Ni, Cr and Fe X-ray intensities on the surface of Alloy 690 bare substrate exposed to sodium borosilicate melt (a) whitish phase and (b) dark phase.*

X-ray mapping on surface of exposed specimens were performed and NiK $\alpha$ , CrK $\alpha$  and FeK $\alpha$  X-ray images as shown in Fig. 4.25 (a–c). NiK $\alpha$  and FeK $\alpha$  X-ray images show the uniform distribution of nickel and iron over the whitish phase, while CrK $\alpha$  image

demonstrates the homogeneous dispersion of chromium on the dark phase. WDS analyses and X-ray mapping studies revealed that, the whitish phase is enriched with nickel along with small amount of iron and the dark phase is mainly composed of chromium.

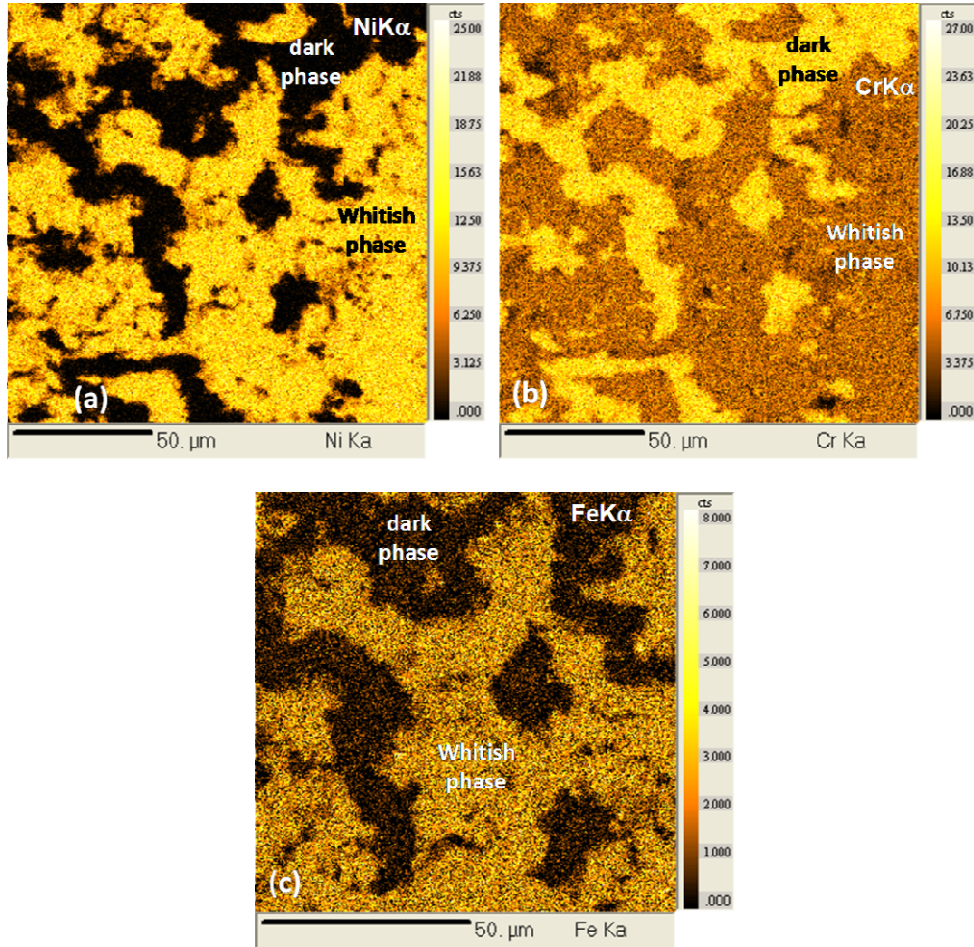


*Fig. 4.25. X-Ray images for (a) NiKa, (b) CrKa and (c) FeKa of surface of Alloy 690 bare substrate that exposed to sodium borosilicate melt revealing the distribution of different elements.*

#### **4.4 Discussions**

Results obtained from the specimens exposed to simulated nuclear waste and sodium borosilicate melt are summarized in Table-4.1.

Table-4.1: Summary of results

Sample history	Technique	Simulated nuclear waste (373 K)	Sodium borosilicate melt (1248 K)
Aluminized and thermally oxidized Alloy 690	Raman spectroscopy	Al <sub>2</sub> O <sub>3</sub> , NiCr <sub>2</sub> O <sub>4</sub> and NiFe <sub>2</sub> O <sub>4</sub> mixed oxides, NiO, Cr <sub>2</sub> O <sub>3</sub> and mixed oxides of Cr <sup>+3</sup> and Cr <sup>+6</sup>	Al <sub>2</sub> O <sub>3</sub> , NiCr <sub>2</sub> O <sub>4</sub> and NiFe <sub>2</sub> O <sub>4</sub> mixed oxides and mixed oxides of Cr <sup>+3</sup> and Cr <sup>+6</sup>
	XPS	Al <sub>2</sub> O <sub>3</sub> and elemental aluminium	Al <sub>2</sub> O <sub>3</sub> , elemental aluminium and NiO
Alloy 690 bare substrate	Raman spectroscopy	γ-Fe <sub>2</sub> O <sub>3</sub> , NiO, Cr <sub>2</sub> O <sub>3</sub> and mixed oxides of Cr <sup>+3</sup> and Cr <sup>+6</sup>	Cr <sub>2</sub> O <sub>3</sub> , NiCr <sub>2</sub> O <sub>4</sub> and NiFe <sub>2</sub> O <sub>4</sub> mixed oxides, NiO and mixed oxides of Cr <sup>+3</sup> and Cr <sup>+6</sup>
	XPS	NiO, elemental nickel and chromium and Cr <sub>2</sub> O <sub>3</sub>	Cr <sub>2</sub> O <sub>3</sub> and CrO <sub>3</sub>

Aluminized and thermally oxidized Alloy 690 specimen having Al<sub>2</sub>O<sub>3</sub> layer on the outermost surface and bare alloy substrates were exposed to nitrate-based simulated nuclear waste solution at 373 K for 216 hours and sodium borosilicate melt at 1248 K for 192 hours. Surfaces of aluminized and thermally oxidized Alloy 690 specimen interacted with simulated nuclear waste which mainly contains Al<sub>2</sub>O<sub>3</sub>, NiCr<sub>2</sub>O<sub>4</sub> and NiFe<sub>2</sub>O<sub>4</sub> mixed oxides, NiO, small amount of Cr<sub>2</sub>O<sub>3</sub>, and mixed oxides of Cr<sup>+3</sup> and Cr<sup>+6</sup> as revealed by Raman spectroscopy. Using same technique, similar surface compositions have been observed for coated samples exposed to sodium borosilicate melt. Raman spectroscopy of surfaces of Alloy 690 bare substrates exposed to simulated nuclear waste revealed the presence of γ-Fe<sub>2</sub>O<sub>3</sub>, NiO, Cr<sub>2</sub>O<sub>3</sub> and mixed oxides of Cr<sup>+3</sup> and Cr<sup>+6</sup>, whereas the bare substrate exposed to sodium borosilicate melt indicated similar surface compositions along with presence of mixed oxides of NiCr<sub>2</sub>O<sub>4</sub> and NiFe<sub>2</sub>O<sub>4</sub>.

Krishnan et al. [85] have studied the Raman spectroscopic and photoluminescence investigations on laser surface modified alumina coatings and reported a prominent Raman peak at  $431.3\text{ cm}^{-1}$  and other less prominent peaks at  $644.2$  and  $574.4\text{ cm}^{-1}$  corresponding to  $\text{Al}_2\text{O}_3$ . Similarly, Misra et al. [86] have observed a peak at  $648\text{ cm}^{-1}$  in the Raman spectra of powdered pure  $\text{Al}_2\text{O}_3$  during the micro-Raman study of aluminium oxide thin film formed through pulsed laser deposition. Kim and Hwang [91] have developed an in-situ Raman spectroscopic system for the study of surface oxide films on Alloy 600 in high temperature water system and recorded the Raman spectra revealing different oxides and mixed oxides. The authors [91] have observed an intense peak at  $687\text{ cm}^{-1}$  ( $\text{NiCr}_2\text{O}_4$ ), less prominent peaks at  $910$  and  $400\text{ cm}^{-1}$  ( $\text{NiO}$ ) and prominent peaks at  $492$  and  $702\text{ cm}^{-1}$  and a shoulder peak at  $654\text{ cm}^{-1}$  ( $\text{NiFe}_2\text{O}_4$ ). They [91] have also noticed an intense band at  $550\text{ cm}^{-1}$  and other less intense bands at  $610$ ,  $352$  and  $302\text{ cm}^{-1}$  representing  $\text{Cr}_2\text{O}_3$ . Abraham et al. [95] have reported a broad band at  $820\text{--}904\text{ cm}^{-1}$  corresponding to a mixture of  $\text{Cr}^{+3}$  and  $\text{Cr}^{+6}$  oxides and a small peak at  $305\text{ cm}^{-1}$  corresponds to  $\text{Cr}_2\text{O}_3$  in the Raman spectra of the oxide film on the surface of Alloy 690 during high temperature passivation studies in lithiated water. Ramya et al. [106] have performed the laser Raman spectroscopic studies of passive films formed on type 316LN SSs during pitting in chloride solution and noted Raman bands around  $665\text{--}680\text{ cm}^{-1}$  corresponds to  $\gamma\text{-Fe}_2\text{O}_3$  and around  $860\text{--}870\text{ cm}^{-1}$  assigned to Cr (III) and Cr (VI) mixed oxides. Therefore, it is evident that the various peaks obtained in Raman spectra in the present study are in accordance with the findings of other investigators [85,86,91,95,106]. Details of Raman spectroscopy results obtained in the present study and those reported in the literature are summarized in Table-4.2.

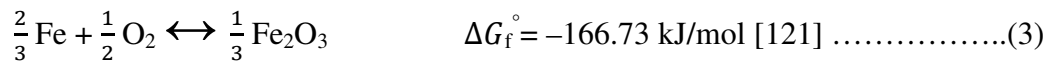
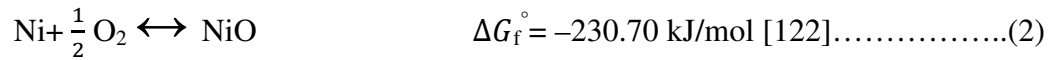
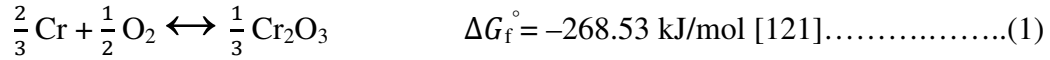
Table-4.2: Details of Raman spectroscopy results and their peak assignments

Raman peaks (in this study)/cm <sup>-1</sup>	Peaks in literature/cm <sup>-1</sup>	Reference	Phase
649	648, 644.2	[85,86]	Al <sub>2</sub> O <sub>3</sub>
430	431.3	[85]	
571	574.4	[85]	
692	687	[91]	NiCr <sub>2</sub> O <sub>4</sub>
687			
694			
906	910	[91]	NiO
910			
399			
489	492	[91]	NiFe <sub>2</sub> O <sub>4</sub>
500			
656			
310	305	[95]	Cr <sub>2</sub> O <sub>3</sub>
305			
558			
540	550	[91]	
355	352		
621	610		
881	820–904	[95]	Cr <sup>+3</sup> & Cr <sup>+6</sup>
875			
872			
874			
660	665–680	[106]	γ-Fe <sub>2</sub> O <sub>3</sub>

The existence of Cr-oxides, as obtained in the present study by Raman spectroscopy on the surface of Alloy 690 substrate exposed to borosilicate melt, appeared to be in agreement with the observations of Dutta et al. [11]. The authors [11] have observed the formation of a continuous, thick Cr<sub>2</sub>O<sub>3</sub> layer at the substrate/glass interface after the exposure of bare Alloy 690 substrate in sodium borosilicate melt at 1248 K for 192 hours. The presence of γ-Fe<sub>2</sub>O<sub>3</sub> and Cr<sub>2</sub>O<sub>3</sub>, as indicated by Raman spectroscopy in case of substrates exposed to simulated nuclear waste solution, is believed to have resulted from the formation

of a bilayer structure consisting of  $\gamma$ -Fe<sub>2</sub>O<sub>3</sub> and Cr<sub>2</sub>O<sub>3</sub> on the surface of the specimen that is in accordance with the observations of Dutta et al. [116].

During the interaction between Alloy 690 bare substrate and borosilicate melt at 1248 K, the following reactions were possible at the interface:



From the values of change in standard free energy of the reaction ( $\Delta G_f^\circ$ ), it is clear that, reaction (1) is thermodynamically most favourable as it has  $\Delta G_f^\circ$  value of -268.53 kJ/mol. Small amounts of NiO and Fe<sub>2</sub>O<sub>3</sub> were also formed at the reaction interface (reaction (2&3)), which lead to the formation of NiCr<sub>2</sub>O<sub>4</sub> (NiO.Cr<sub>2</sub>O<sub>3</sub>) and NiFe<sub>2</sub>O<sub>4</sub> (NiO.Fe<sub>2</sub>O<sub>3</sub>) mixed oxides. Formation of Cr<sub>2</sub>O<sub>3</sub> at the interface was restricted in case of aluminized and thermally oxidized specimens. During the exposure experiments, Al<sub>2</sub>O<sub>3</sub> layer present on the uppermost surfaces of coated specimen, acted as a diffusion barrier between borosilicate melt and the specimen, and outward diffusion of Cr from the substrate to the interface was restricted. Schematic representation of exposure of Alloy 690 bare substrate and aluminized and oxidized specimen with sodium borosilicate melt is given in Figs. 4.26 and 4.27.

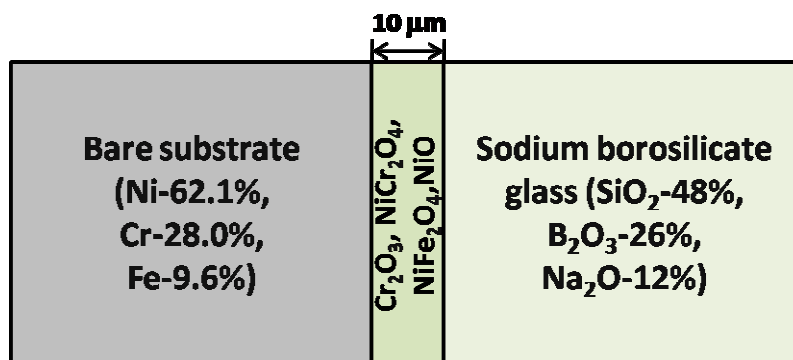


Fig. 4.26. Schematic representation of interaction of Alloy 690 bare substrate with sodium borosilicate melts.

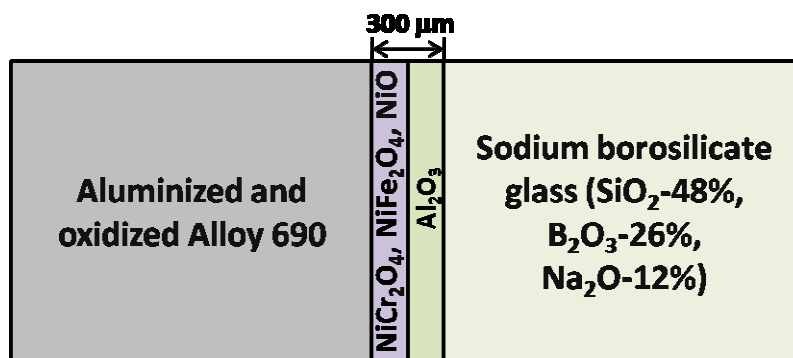


Fig. 4.27. Schematic representation of interaction of aluminized (high Al containing pack) and oxidized Alloy 690 specimen with sodium borosilicate melts.

XPS analyses on aluminized and thermally oxidized Alloy 690 specimen interacted with simulated nuclear waste have shown the presence of  $\text{Al}_2\text{O}_3$  and  $\text{Al}^0$ . Samples exposed to sodium borosilicate melt have also shown the presence of NiO along with  $\text{Al}_2\text{O}_3$  and  $\text{Al}^0$ . For Alloy 690 bare substrate exposed to simulated nuclear waste, XPS analysis indicated the presence of  $\text{Cr}_2\text{O}_3$ , elemental chromium, NiO and elemental nickel, whereas the presence of  $\text{Cr}_2\text{O}_3$  and  $\text{CrO}_3$  have been noticed on the sample exposed in borosilicate melt.

Zähr et al. [99] have carried out the characterization of oxide and hydroxide layers on aluminium alloy materials (Al–Mn–alloy, both side clad with Al–Si–alloy) using XPS. The authors [99] have recorded the Al<sub>2p<sub>3/2</sub></sub> XPS spectrum on pure Al<sub>2</sub>O<sub>3</sub> and aluminium alloy with different conditions and obtained the binding energy peaks at 74.3 eV, which corresponds to Al<sub>2</sub>O<sub>3</sub>. E. Paparazzo [102] has reported the XPS spectrum of O1s level at 531.5 eV corresponds to Al<sub>2</sub>O<sub>3</sub>. Dutta et al. [116] have noticed the Ni<sub>2p<sub>3/2</sub></sub> XPS peak at 852.7 eV corresponds to elemental nickel (Ni<sup>0</sup>) and O1s XPS peak at 530.2 eV corresponds to oxide of chromium. Samantaroy et al. [109] have investigated the corrosion behavior of Alloy 690 by potentiodynamic anodic polarization technique in both 3 M HNO<sub>3</sub> and in simulated HLW in 3 M HNO<sub>3</sub>. Ni<sub>2p<sub>3/2</sub></sub> XPS spectra for Alloy 690, which was passivated in simulated HLW, showed the peak binding energy at 854.0 eV corresponds to NiO. Stypuła et al. [117] have carried out the characterization of passive films on chromium electrodes in aqueous H<sub>2</sub>SO<sub>4</sub> solutions and anhydrous systems H<sub>2</sub>SO<sub>4</sub>–formamide by XPS. The authors [117] have observed the peak of elemental chromium (Cr<sup>0</sup>) at 574.3 eV and that of Cr<sub>2</sub>O<sub>3</sub> at 576.2 eV. Therefore, it appears that the findings of XPS studies in the present investigation are in accordance with the results of other researchers [99,102,116,109,117]. Details of XPS results obtained in the present study and those reported in the literature are given Table-4.3.

Microstructural analysis of aluminized and oxidized Alloy 690 specimen exposed to simulated nuclear waste revealed a two phase structure, a whitish phase and a dark phase. WDS analyses along with X-ray mapping revealed the homogeneous distribution of aluminium over the dark phase and distribution of nickel, chromium and iron on the whitish phase. This indicates that, the dark phase is enriched with Al<sub>2</sub>O<sub>3</sub> and the whitish phase is

composed of  $\text{Cr}_2\text{O}_3$ ,  $\text{NiCr}_2\text{O}_4$ ,  $\text{NiFe}_2\text{O}_4$  and  $\text{NiO}$  as revealed by Raman spectroscopy and XPS studies.

Table-4.3: Details of XPS peaks and their assignments

XPS peaks (in this study)/eV		Peaks in literature/eV	Reference	Phase
Al2p	72.4	72.4	[96]	$\text{Al}^0$
	72.6			
	74.3	74.3	[99]	$\text{Al}_2\text{O}_3$
	74.9			
O1s	531.6	531.5	[98,101,102]	$\text{Al}_2\text{O}_3$
	529.6	529.6	[96]	$\text{NiO}$
	528.6			
	531.1	530.2	[116]	$\text{Cr}_2\text{O}_3$
	531.5			
Ni2p	851.7	852.7	[106,108]	$\text{Ni}^0$
	856.0	854.0	[109–111]	$\text{NiO}$
	855.6			
Cr2p	575.6	574.3	[117]	$\text{Cr}^0$
	576.6	576.2	[117]	$\text{Cr}_2\text{O}_3(2p_{3/2})$
	586.3	586.0	[96]	$\text{Cr}_2\text{O}_3(2p_{1/2})$
	578.4	576.6	[117]	$\text{Cr}_2\text{O}_3$
	580.9	578.5	[96]	$\text{CrO}_3$

Dutta et al. [14] have reported  $\text{Al}_2\text{O}_3$  layer along with  $\text{NiAl}$  and  $\text{Ni}_2\text{Al}_3$  type phases with the help of XRD studies on the surface of aluminized and thermally oxidized Ni-Cr-Fe superalloy 690 specimens that exposed to simulated nuclear waste solution. Therefore, the presence of Ni and Cr on the surface of exposed specimen as indicated in X-ray images is in consistent with the results of previous findings [14]. Alloy 690 bare substrate exposed to simulated nuclear waste showed the presence of Ni, Cr and Fe on the surface of the specimen as revealed by WDS spectrum. Sengupta et al. [44] have obtained the similar WDS spectrum on the grain boundaries of Alloy 690 substrate that exposed to simulated HLW for 384 hours. Aluminized and oxidized Alloy 690 specimen exposed to sodium borosilicate melt revealed a

continuous microstructure. X-ray image and WDS analysis clearly reveal that, the surface of the exposed specimen is enriched with aluminium along with small amounts of nickel, chromium and iron. This is the indication of presence of  $\text{Al}_2\text{O}_3$  along with other compounds like  $\text{NiCr}_2\text{O}_4$ ,  $\text{NiFe}_2\text{O}_4$  and  $\text{NiO}$  as observed by Raman spectroscopy and XPS studies. Dutta et al. [11] have carried out the SEM with EDXS analysis along the cross-section of aluminide coated sample with adhered glass phase. The authors [11] have reported good stability of thermally oxidized aluminide coating after prolonged exposure in borosilicate melt. We have noticed [112] only a partial dissolution of Al into the glass phase after interaction of aluminized and thermally oxidized Alloy 690 substrates with sodium borosilicate melt. Therefore finding of enrichment of Al and depletion of Cr on the surface of specimen after prolonged exposure with sodium borosilicate melt appears to be in agreement with the results of other studies [11,112]. Microscopic analysis of Alloy 690 bare substrate that exposed to sodium borosilicate melt indicated two phase microstructure, a whitish phase and dark phase. WDS analyses and X-ray mapping studies revealed that, the whitish phase is enriched with nickel along with small amount of iron and the dark phase is mainly composed of chromium. The presence of mixed oxides of  $\text{NiCr}_2\text{O}_4$  and  $\text{NiFe}_2\text{O}_4$ , in case of specimen exposed to borosilicate melt is attributed to exposure at elevated temperature (1248 K). By taking into account of Raman spectroscopy results, it may be stated that, the dark phase obtained on the surface of Alloy 690 substrate after exposure with sodium borosilicate melt, is composed of  $\text{Cr}_2\text{O}_3$  and  $\text{NiCr}_2\text{O}_4$  and the whitish phase is of  $\text{NiO}$  and  $\text{NiFe}_2\text{O}_4$ . Therefore, the microscopic analysis results obtained in the present investigation is in agreement with literature [11,14,44,112].

Aluminized and thermally oxidized Alloy 690 specimen with  $\text{Al}_2\text{O}_3$  layer on uppermost surface exposed in simulated nuclear waste and sodium borosilicate melt has shown good stability. From the above discussions, it is evident that the surface composition of coated specimen exposed to simulated nuclear waste is similar to that exposed to sodium borosilicate melt. This could be attributed to the unaltered mixed oxides that were formed on the surface of the specimens during oxidation (1273 K for 4 hours) prior to the exposure in either of the media. In case of Alloy 690 substrate, some minor difference in surface composition was observed between the samples exposed to simulated nuclear waste solution and sodium borosilicate melt. The presence of mixed oxides of  $\text{NiCr}_2\text{O}_4$  and  $\text{NiFe}_2\text{O}_4$ , in case of specimen exposed to borosilicate melt is attributed to exposure to elevated temperature. It is, therefore, evident from the present study that there is a difference in surface composition as detected by the two techniques, those are Raman spectroscopy and XPS. It is known that, XPS is a surface sensitive technique that detects only those photoelectrons involved upto a depth of 10 nm from the surface of the sample, whereas Raman spectroscopy is able to detect the compounds upto a few microns from the surface. Therefore, the difference in surface compositions revealed between the two techniques is believed to have resulted from the depth sensitivity of the two techniques.

Separate analyses of sodium borosilicate glass that interacted with aluminized (with high Al-containing pack (10 wt.%) and thermally oxidized Alloy 690 specimen, indicated the incorporation of  $\text{Al}^{+3}$  from the specimen to the glass phase which leads to the modification of glass structure. Details of these analyses will be discussed in Chapter-6. In order to reduce the Al activity and avoid the inclusion of  $\text{Al}^{+3}$  in glass network, it is intended to reduce the aluminium content in the pack aluminization mixture to 2 wt.%. Interaction of

aluminized (low aluminium containing pack (2 wt.%) and thermally oxidized Alloy 690 specimen with simulated nuclear waste and sodium borosilicate melt will be discussed in the next chapter (Chapter-5).

## 4.5 Conclusions

The following conclusions can be drawn from this investigation:

1. Good stability has shown by aluminized and thermally oxidized Alloy 690 specimen with  $\text{Al}_2\text{O}_3$  layer on uppermost surface even after prolonged exposure in simulated nuclear waste and sodium borosilicate melt.
2. Surface of aluminized and thermally oxidized Alloy 690 specimen with high Al-content exposed to simulated nuclear waste consists of  $\text{Al}_2\text{O}_3$ ,  $\text{NiCr}_2\text{O}_4$  and  $\text{NiFe}_2\text{O}_4$  mixed oxides, NiO, small amount of  $\text{Cr}_2\text{O}_3$  and mixed oxides of  $\text{Cr}^{+3}$  and  $\text{Cr}^{+6}$  as revealed by Raman spectroscopy. Similar surface compositions were noticed for coated samples exposed to sodium borosilicate melt.
3. XPS studies have shown that aluminized and thermally oxidized Alloy 690 specimen exposed to simulated nuclear waste contain  $\text{Al}_2\text{O}_3$  and  $\text{Al}^0$ , whereas samples exposed to borosilicate melt indicated the presence of NiO along with  $\text{Al}_2\text{O}_3$  and  $\text{Al}^0$ .
4. The surface composition of coated specimen exposed to simulated nuclear waste is similar to that exposed in sodium borosilicate melt. This could be attributed to the unaltered mixed oxides that were formed on the surface of the specimens during pre-oxidation treatment.
5. For Alloy 690 bare substrates exposed to simulated nuclear waste, Raman spectroscopy indicated the presence of  $\gamma\text{-Fe}_2\text{O}_3$ , NiO, some amount of  $\text{Cr}_2\text{O}_3$  and mixed oxides of  $\text{Cr}^{+3}$  and  $\text{Cr}^{+6}$ , whereas substrate exposed to borosilicate melt reveal similar composition along

with the presence of mixed oxides of  $\text{NiCr}_2\text{O}_4$  and  $\text{NiFe}_2\text{O}_4$ . The presence of mixed oxides for substrate exposed in molten glass is due to high temperature (1248 K) exposure.

6. Surface of Alloy 690 bare substrates exposed to simulated nuclear waste consists of  $\text{Cr}_2\text{O}_3$ , elemental chromium,  $\text{NiO}$  and elemental nickel as revealed by XPS studies, while the presence of  $\text{Cr}_2\text{O}_3$  and  $\text{CrO}_3$  have been found for the sample exposed to sodium borosilicate melt.
7. The difference in surface compositions indicated between Raman spectroscopy and XPS could be attributed to the depth sensitivity of these two techniques.

# **Interaction of aluminized (using low Al-containing pack) and oxidized Alloy 690 with simulated nuclear waste and sodium borosilicate melts**

---

## **5.1 Introduction**

In previous chapter, it has been shown that exposure of high Al containing coated samples with sodium borosilicate glass lead to the incorporation of  $Al^{+3}$  in the glass. This was attributed to the high activity of excess Al in the coating. In the present chapter, a new coating with low Al was attempted. These low Al containing coated specimens were subjected to similar exposure treatments as was done for high Al containing samples reported in previous chapter. Selection of exposure temperature and time was based on the real plant scale vitrification process. The interacted specimens were characterized by using Raman spectroscopy, XPS and scanning electron microscopy (SEM) with energy dispersive X-ray spectroscopy (EDS).

## **5.2 Experimental Methods**

Alloy 690 specimens, having dimensions 10 mm × 10 mm × 5 mm, were aluminized with low Al-containing pack (2 wt.% Al powder, 2 wt.%  $NH_4Cl$  and 96 wt.%  $Al_2O_3$  powder). The pack was heated to 1273 K and soaked for 4 hours, and subsequently heat treated at 1273

K for 8 h, to grow an oxide layer at the surface. These heat treated specimens were distributed into two sets viz. Set C and Set D. The specimens of set C were exposed to simulated high-level nuclear liquid waste (nitrate-based environment) solution at 373 K for a period of 216 h, and specimens of Set D were exposed to sodium borosilicate melt at 1248 K for a period of 192 h. At the end of the exposure, the specimens of Set C were removed from the flask, cleaned, dried and characterized without any surface modification, using Raman spectroscopy, XPS and SEM with EDS techniques. The specimens of Set D were also characterized using these techniques, after removing the glass phase attached to them during the exposure to borosilicate melt. Linear baseline corrections have been carried out on all the data acquired for the XPS spectra in order to eliminate the background. The positions of all the XPS peaks in the spectrum were assigned on the basis of Gaussian model of peak fitting. The details of experimental procedures and characterization techniques are discussed in Chapter 3.

## **5.3 Results**

### **5.3.1. Microstructure of aluminide coatings**

Microstructural examinations of the cross-section of aluminized Alloy 690 substrate using SEM with EDS indicated the formation of a Cr-rich layer (composition: 6.14Al-73.81Cr-10.63Fe-9.41Ni, at.%) close to the substrate. It was also noted that a layer of NiAl (composition: 53.22Al-1.9Cr-2.29Fe-42.59Ni, at.%) and (Ni,Cr)Al (composition: 54.85Al-11.58Cr-4.65Fe-28.93Ni, at.%) were formed on the outer side of the coating, as shown in Fig. 5.1(a). Chemical composition of these multilayers was determined by EDS point analyses. Fig. 5.1(b) describes the EDS line scan across the cross-section indicated the

presence of  $\text{Al}_2\text{O}_3$  on the uppermost surface. Chemical composition of  $\text{Al}_2\text{O}_3$  layer as revealed by EDS point analyses shows typical as: 65.26O-31.22Al-1.24Cr-0.39Fe-1.9Ni (at.%). Surface microstructure of aluminized and thermally oxidized Alloy 690 substrate is also shown in Fig. 5.1(c). For the purpose of comparison, different aluminides formed on Alloy 690 specimen in high Al (Discussed in Chapter-4) and low Al containing coatings are given in a tabular form in Table-5.1.

Table-5.1. Different aluminides formed on Alloy 690 specimen in high Al and low Al containing coatings.

<b>Aluminides formed on Alloy 690 specimen in high Al (10 wt.%) containing coating</b>	<b>Aluminides formed on Alloy 690 specimen in low Al (2 wt.%) containing coating</b>
Interdiffusion layer	Cr-rich layer
(NiCr)Al	NiAl
(NiCr)Al + $\text{Cr}_5\text{Al}_8$	(NiCr)Al
$\text{Al}_2\text{O}_3$	$\text{Al}_2\text{O}_3$

### 5.3.2. Specimens exposed to simulated nuclear waste solution (Set C)

Fig. 5.2 shows the micro-Raman spectrum for surfaces of specimens of set C, exposed to simulated nuclear waste solution. A predominant peak at  $645\text{ cm}^{-1}$  in the spectrum revealed the presence of  $\text{Al}_2\text{O}_3$  [85-90]. Another peak observed at  $483\text{ cm}^{-1}$  showed the presence of  $\text{NiFe}_2\text{O}_4$  mixed oxide [91]. Raman spectrum also showed the peaks, which correspond to  $\text{Cr}_2\text{O}_3$  at  $310\text{ cm}^{-1}$  [91,95], and mixture of  $\text{Cr}^{3+}$  and  $\text{Cr}^{6+}$  oxides at  $875\text{ cm}^{-1}$  [95].

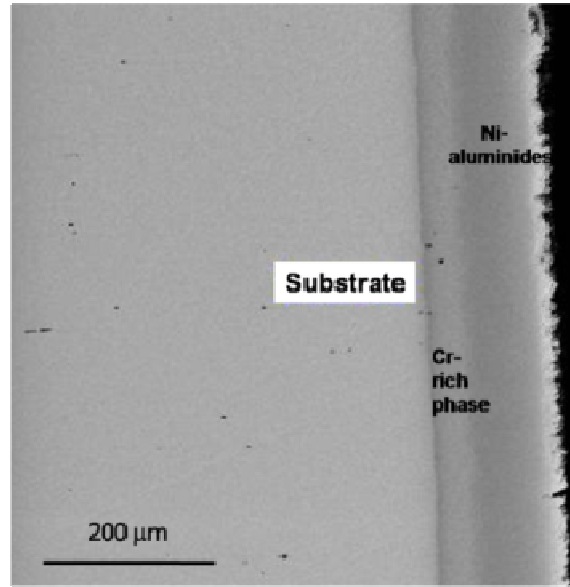


Fig. 5.1(a). Aluminized (using low Al-containing pack) and thermally oxidized Alloy 690 specimen revealing Cr-rich layer, NiAl and (NiCr) Al layer type aluminides along the cross-section.

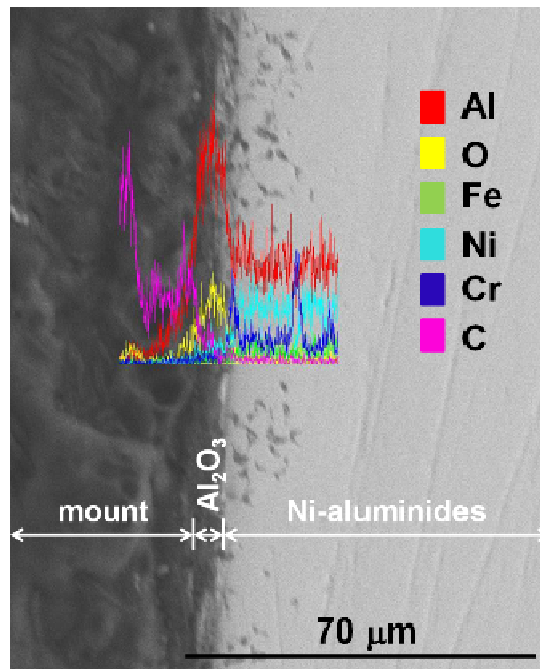


Fig. 5.1 (b). EDS line scan along the cross-section of Aluminized (using low Al-containing pack) and thermally oxidized Alloy 690 specimen revealing Al<sub>2</sub>O<sub>3</sub> on the uppermost surface.

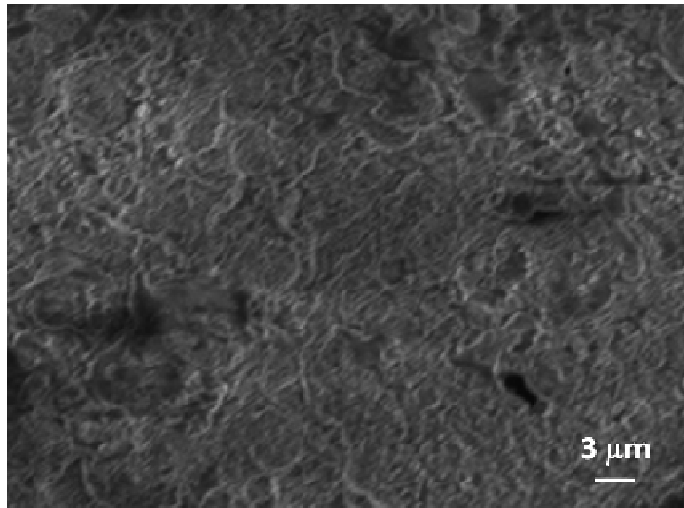


Fig. 5.1(c). Surface image (BSE) of aluminized (using low Al-containing pack) and thermally oxidized Alloy 690 specimen.

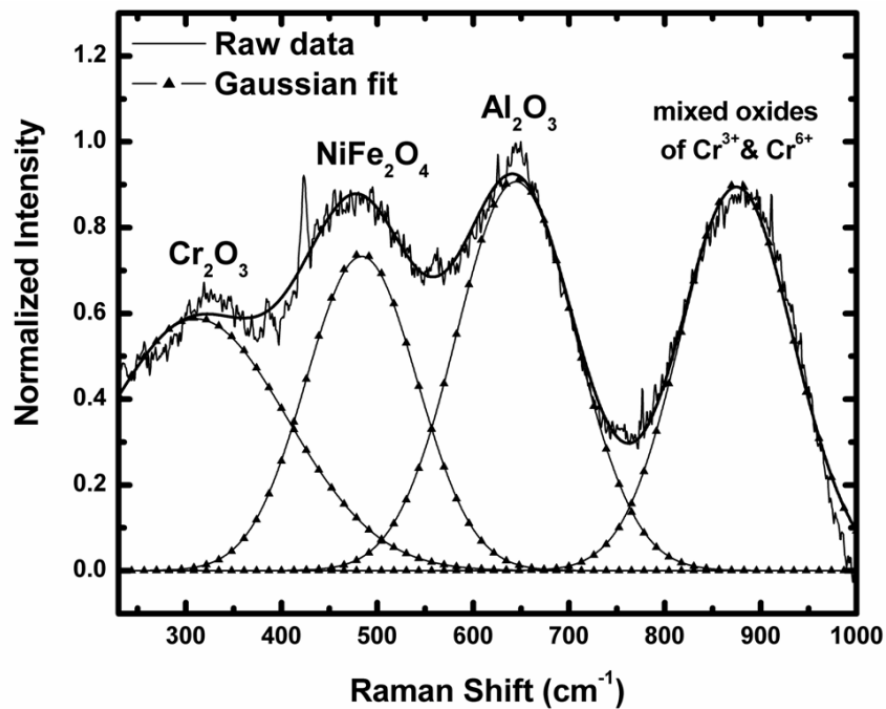
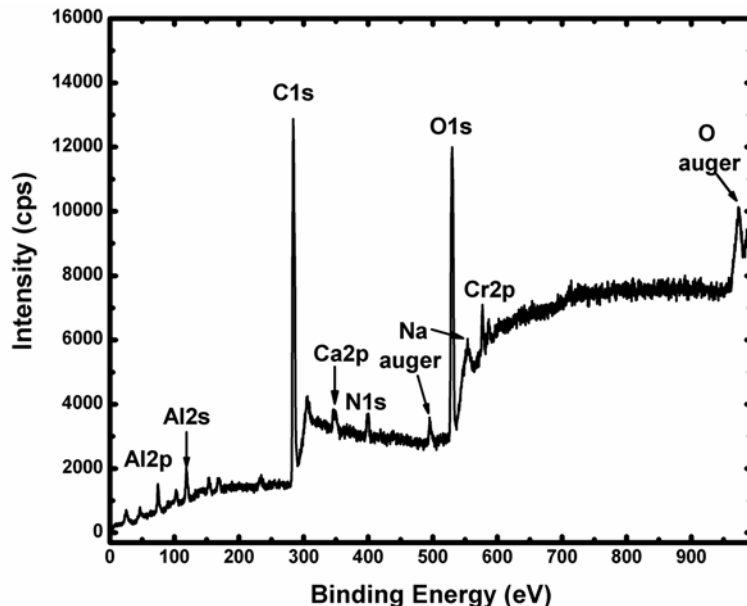


Fig. 5.2. Normalized Raman spectrum of a specimen from Set C after exposure to simulated nuclear waste solution.



*Fig. 5.3. XPS survey spectrum recorded on a specimen from Set C after exposure to simulated high level nuclear waste solution.*

After the exposure of specimens of Set C in simulated nuclear waste, XPS survey spectrum (Fig. 5.3) and high resolution spectra for  $2p_{3/2}$  level of Al and Cr, and  $1s$  level of oxygen were recorded on the specimen surface. For  $Al2p_{3/2}$ , two XPS were obtained as described in Fig. 5.4a. The first peak, obtained at 74.4 eV, corresponds to  $Al_2O_3$  [98-101]. However, for peak occurring at 76.2 eV, no proper oxide could be assigned. Detailed literature review showed that, such peaks were assigned to some native oxides [96]. Based on this observation, in the present study, peak obtained at 76.2 eV was assigned to some suboxide and unstable Al oxides which are termed as native oxide. For chromium, XPS peak was noticed at 576.9 eV ( $2p_{3/2}$ ) along with a satellite peak at 586.7 eV ( $2p_{1/2}$ ) indicating the presence of  $Cr_2O_3$  [117-119] as is shown in Fig. 5.4b.  $O1s$  spectra also contained two peaks. The first peak occurred at 528.9 eV corresponding to a value that is lower than that of  $Cr_2O_3$

[116,118] and the second one at 531.1 eV has been assigned to  $\text{Al}_2\text{O}_3$  [98,101,102] as is evident from Fig. 5.4c.

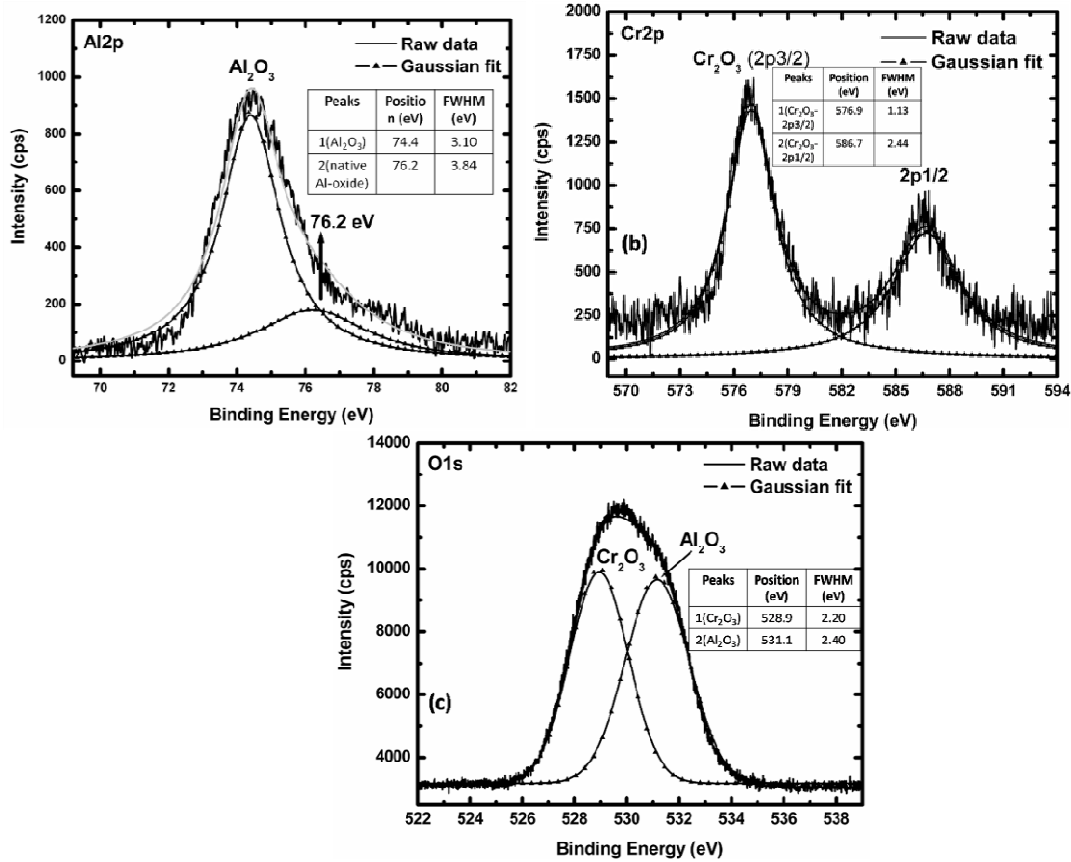
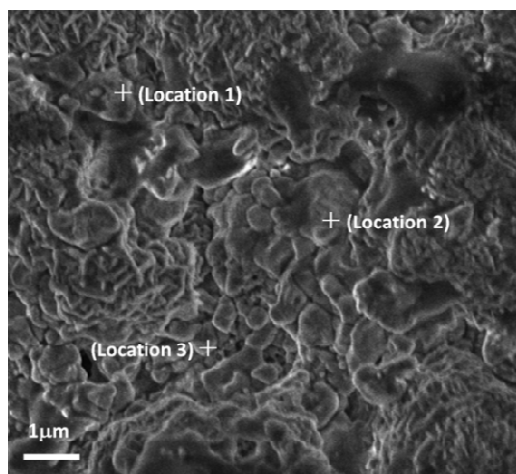


Fig. 5.4. XPS spectra recorded on the surface of a specimen from Set C after exposure to simulated high level nuclear waste solution (a)  $\text{Al}2p$  spectrum showing  $\text{Al}_2\text{O}_3$  and native oxide of Al, (b)  $\text{Cr}2p$  spectrum, reveals  $\text{Cr}_2\text{O}_3$  and (c)  $\text{O}1s$  spectrum shows  $\text{Cr}_2\text{O}_3$  and  $\text{Al}_2\text{O}_3$ .

The microstructure of the surface of a specimen from Set C, exposed to simulated nuclear waste solution, is shown in Fig. 5.5. Presence of a uniform layer was observed on the surface even after prolonged exposure. Quantitative EDS analysis was carried out at three different locations on the exposed specimen in order to understand the surface composition. EDS spectra and results of compositional analysis are described in Fig. 5.6 and Table-5.2 respectively.



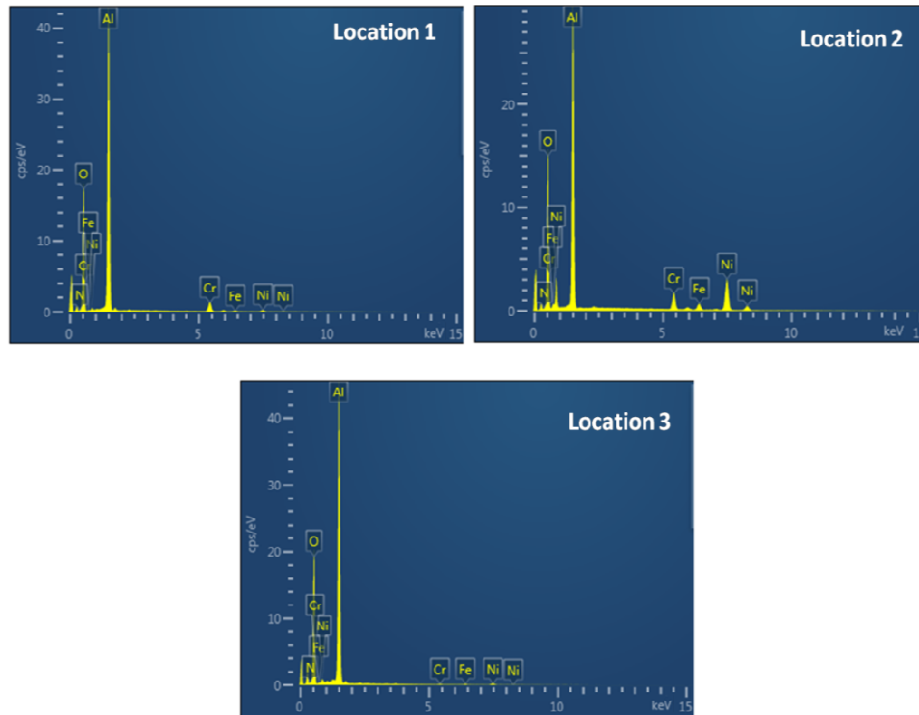
*Fig. 5.5. Secondary electron micrograph of the of a specimen from Set C exposed to simulated nuclear waste revealing pore-free uniform microstructure.*

Table-5.2. Compositional EDS analysis results from different locations of a specimen from Set C exposed to simulated nuclear waste solution.

Locations	Elements in at. %				
	O	Al	Ni	Cr	Fe
Location-1	59.6	37.4	0.6	2.1	0.3
Location-2	52.7	34.3	9.2	2.6	1.2
Location-3	62.6	36.6	0.5	0.1	0.2

EDS analysis shows the variation of Al from 34 to 37 at. % and O from 52 to 62 at. %, reveal the presence of  $\text{Al}_2\text{O}_3$  layer and it is in agreement with the presence of  $\text{Al}_2\text{O}_3$  that was obtained in Raman spectroscopy and XPS studies. This is indicative of the fact that the  $\text{Al}_2\text{O}_3$  layer on surface of the specimen is stable even after prolonged exposure in simulated nuclear waste. Small amounts of Ni, Cr and Fe were also detected on the surface. Figs. 5.7 (a–e) show the  $\text{AlK}\alpha$ ,  $\text{OK}\alpha$ ,  $\text{NiK}\alpha$ ,  $\text{CrK}\alpha$  and  $\text{FeK}\alpha$  X-ray images acquired from the surface of a sample exposed to simulated nuclear waste.  $\text{AlK}\alpha$  and  $\text{OK}\alpha$  images show the

homogeneous distribution of Al and O over the surface as shown in Figs. 5.7 (a and b). Inhomogeneous distributions of Ni, Cr and Fe were also observed, as shown in  $NiK\alpha$ ,  $CrK\alpha$  and  $FeK\alpha$  X-ray images in Figs. 5.7 (c–e), respectively. Combining the information from Raman spectroscopy and XPS with EDS analysis, it could be inferred the presence of  $NiFe_2O_4$  and  $Cr_2O_3$ .



*Fig. 5.6. EDS spectra recorded on different locations of a specimen from Set C exposed to simulated nuclear waste solution.*

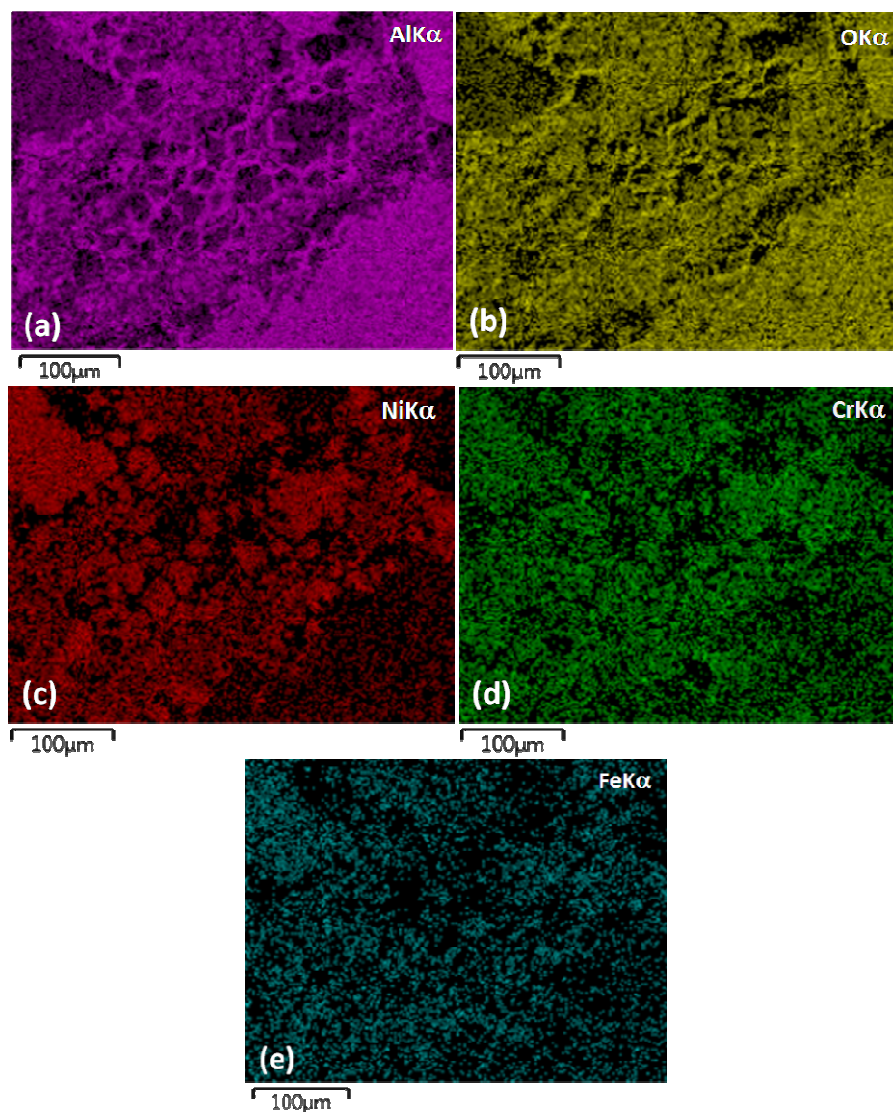


*Fig. 5.7. X-Ray images for (a) AlK $\alpha$ , (b) OK $\alpha$ , (c) NiK $\alpha$ , (d) CrK $\alpha$  and (e) FeK $\alpha$  of a specimen from set C that was exposed to simulated nuclear waste solution revealing the distribution of various elements.*

### **5.3.3. Specimens exposed to sodium borosilicate melt (Set D)**

Fig. 5.8 demonstrates the micro-Raman spectrum of the surfaces of a specimen from Set D exposed to sodium borosilicate melt. The intense peak occurring at  $648\text{ cm}^{-1}$  revealed the presence of aluminium oxide ( $\text{Al}_2\text{O}_3$ ) [85-90]. The peak observed at  $490\text{ cm}^{-1}$  showed the existence of  $\text{NiFe}_2\text{O}_4$  mixed oxide [91] on the surface of the specimen. The

Raman spectrum also revealed presence of  $\text{Cr}_2\text{O}_3$ , and mixture of  $\text{Cr}^{3+}$  and  $\text{Cr}^{6+}$  oxides by the peaks obtained at  $313\text{ cm}^{-1}$  and  $875\text{ cm}^{-1}$  respectively [95].

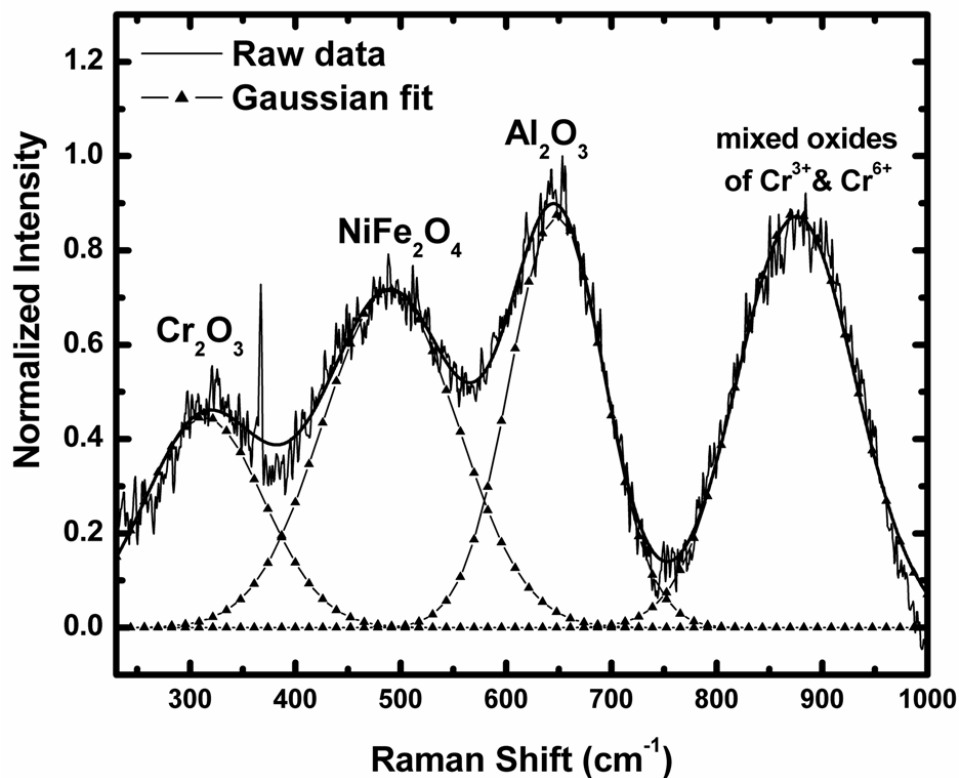


*Fig.5.8. Normalized Raman spectrum of a specimen from Set D after exposure to sodium borosilicate melt.*

Specimens from Set D exposed to sodium borosilicate melt were subjected to XPS survey scan and it is shown in Fig. 5.9.  $\text{Al}2p_{3/2}$  and  $\text{O}1s$  high resolution XPS spectra were also recorded after the exposure. Two XPS peaks were obtained in the case of  $\text{Al}2p_{3/2}$  spectrum as demonstrated in Fig. 5.10a. The first peak appearing at 74.3 eV corresponded to  $\text{Al}_2\text{O}_3$  [98-101]. Peak occurred at 76.7 eV, was assigned to some native oxide of Al [96].  $\text{O}1s$  spectrum showed a minute contribution from  $\text{Cr}_2\text{O}_3$  [116,118] at a binding energy value of 528.0 eV along with strong peak of  $\text{Al}_2\text{O}_3$  [98,101,102] occurring at 530.6 eV (Fig. 5.10b).

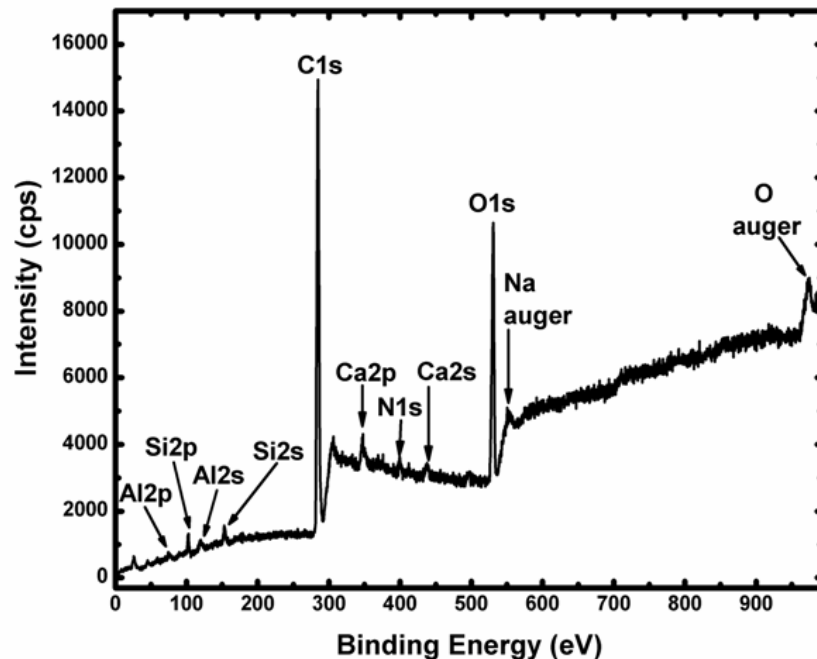


Fig. 5.9. XPS survey spectrum recorded on the surface of a specimen from Set D exposed to sodium borosilicate melt.

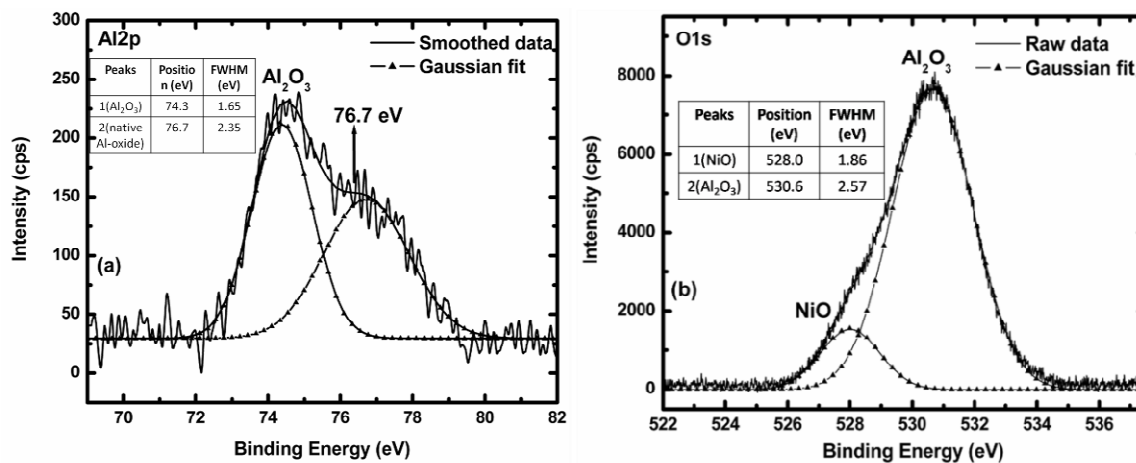
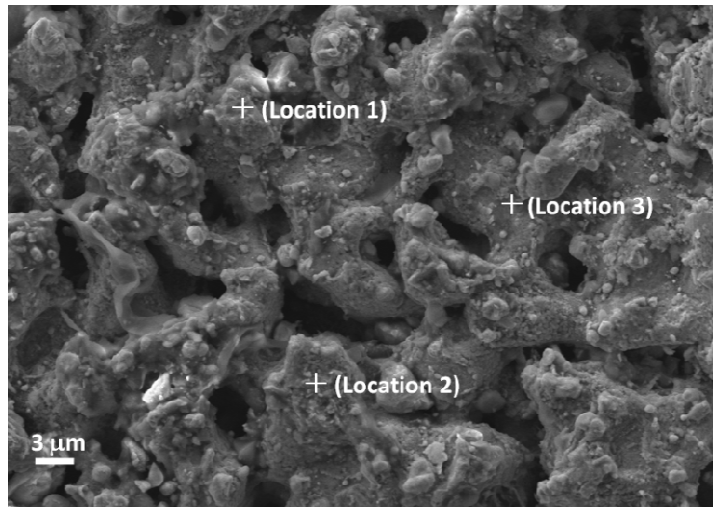


Fig. 5.10. XPS spectra recorded on the surface of a specimen from Set D exposed to sodium borosilicate melt, (a) Al<sub>2</sub>p spectrum showing Al<sub>2</sub>O<sub>3</sub> and native oxide of Al and (b) O1s spectrum reveals Cr<sub>2</sub>O<sub>3</sub> and Al<sub>2</sub>O<sub>3</sub>.



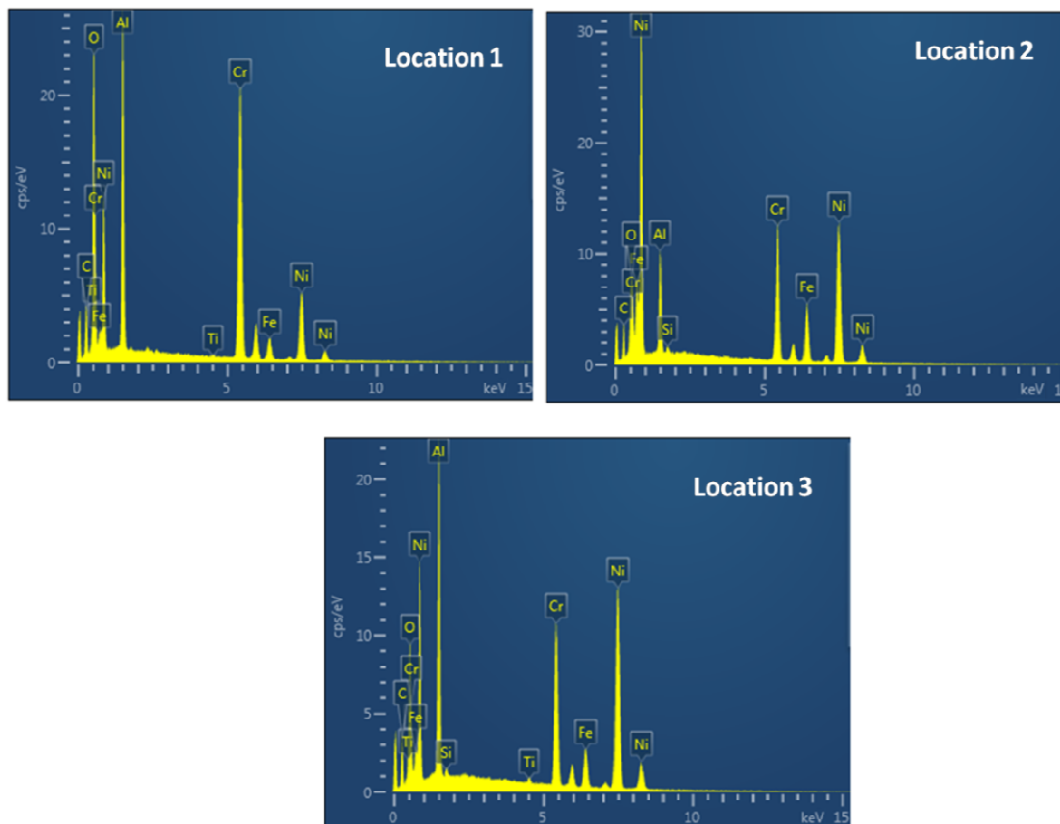
*Fig. 5.11. Secondary electron micrograph of a specimen from Set D that was exposed to sodium borosilicate melt revealing fairly homogeneous microstructure after prolonged exposure.*

Table-5.3. Compositional EDS analysis results from different locations on a specimen from Set D that was exposed to sodium borosilicate melt.

Locations	Elements in at. %						
	O	Al	Ni	Cr	Fe	Si	Ti
Location-1	45.8	20.3	10.4	21.2	2.2	0.0	0.1
Location-2	19.3	14.0	37.2	18.5	10.3	0.7	0.0
Location-3	25.4	25.4	31.4	13.1	3.9	0.6	0.3

The microstructure of a specimen from Set D exposed to sodium borosilicate melt is shown in Fig. 5.11. An almost homogeneous microstructure was observed on the surface of the exposed specimen. Quantitative EDS analysis on the surface of exposed specimen was carried out at three different locations on point to point basis in order to understand the

surface chemistry. EDS spectra and results of compositional analysis are described in Fig. 5.12 and Table-5.3 respectively.



*Fig. 5.12. EDS spectra recorded on different locations of a specimen from Set D exposed to sodium borosilicate melt.*

EDS analysis shows the concentration variation of different elements, viz. Al (14–25 at. %), O (19–45 at.%), Ni (10–31 at.%), Cr (13–21 at.%) and Fe (2–10 at.%), which depicts the presence of  $\text{Al}_2\text{O}_3$  layer,  $\text{NiFe}_2\text{O}_4$  and  $\text{Cr}_2\text{O}_3$ . This is in accordance with the presence of  $\text{Al}_2\text{O}_3$ ,  $\text{Cr}_2\text{O}_3$  and  $\text{NiFe}_2\text{O}_4$  that was detected in Raman spectroscopy and XPS. This also gave the hint of the stability of  $\text{Al}_2\text{O}_3$  layer on the surface of coated specimen after the exposure to sodium borosilicate melt at elevated temperature. X-ray images of  $\text{AlK}\alpha$ ,  $\text{OK}\alpha$ ,  $\text{NiK}\alpha$ ,  $\text{CrK}\alpha$  and  $\text{FeK}\alpha$  (Figs. 5.13 (a-e)) recorded on the surface of coated samples exposed to sodium

borosilicate melt showed the distribution of elements. Al, O, Ni and Cr were almost uniformly dispersed on the surface. In addition, presence of small amount of Fe was observed in some regions.

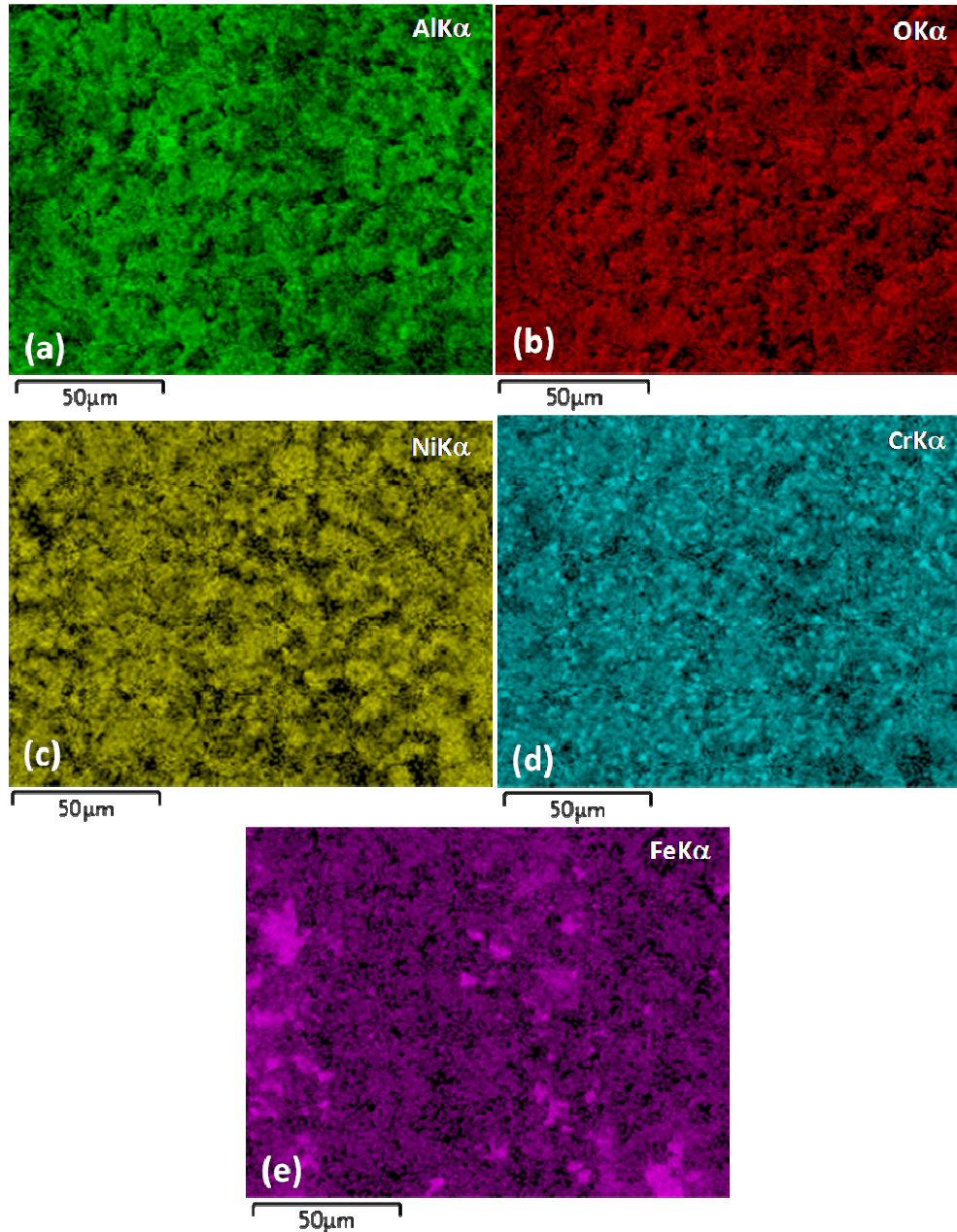


*Fig. 5.13. X-Ray images for (a) AlK $\alpha$ , (b) OK $\alpha$ , (c) NiK $\alpha$ , (d) CrK $\alpha$  and (e) FeK $\alpha$  on specimen from Set D that was exposed to sodium borosilicate melt revealing the distribution of various elements.*

## 5.4 Discussions

Aluminized (using low Al-containing pack) and thermally oxidized Alloy 690 specimen with  $\text{Al}_2\text{O}_3$  layer on outer surface were interacted with simulated nuclear waste at 373 K for 216 hours and sodium borosilicate melt at 1248 K for 198 hours. After interaction with simulated nuclear waste, surfaces of aluminized and thermally oxidized Alloy 690 specimen showed the presence of  $\text{Al}_2\text{O}_3$ ,  $\text{NiFe}_2\text{O}_4$  mixed oxide,  $\text{Cr}_2\text{O}_3$  and mixed oxides of  $\text{Cr}^{+3}$  and  $\text{Cr}^{+6}$  as revealed by Raman spectroscopy (Figs. 5.3 & 5.8). Stoichiometry of mixed oxides of  $\text{Cr}^{+3}$  and  $\text{Cr}^{+6}$  was determined using FWHM method. The typical values obtained were 46% of  $\text{Cr}^{+3}$  and 54% of  $\text{Cr}^{+6}$ . Even the samples exposed to sodium borosilicate melt, showed the presence of nearly same oxides. Both these results clearly show that, aluminium oxide formed on the uppermost surface is providing sufficient protection against aggressive environments. The various peaks obtained in the Raman spectra in the present study are in agreement with the findings of other researchers [85,86,91,95]. Raman spectroscopy results obtained in the present study and those reported in the literature are summarized in Table-5.4.

XPS analyses on both aluminized and thermally oxidized Alloy 690 specimen exposed to simulated nuclear waste and sodium borosilicate melt have revealed the presence of  $\text{Al}_2\text{O}_3$  and  $\text{Cr}_2\text{O}_3$ . The results of XPS studies in the present study are in accordance with the findings of other investigators [99,102,116,117]. Details of XPS results obtained in the present study and those reported in the literature are given in Table-5.5.

Surfaces of aluminized and thermally oxidized Alloy 690 specimens exposed to simulated nuclear waste solution and sodium borosilicate melt consist of  $\text{Al}_2\text{O}_3$  layer. Presence of  $\text{Al}_2\text{O}_3$  could be attributed to the good stability of aluminide coatings with  $\text{Al}_2\text{O}_3$  layer on the top of the surface. Good adherence of aluminide coatings on the surface of Alloy

690 substrate, even after prolonged exposure in nitrate-based solution (simulated nuclear high-level liquid waste) has been observed by Dutta et al [14]. Presence of Ni in EDS spectrum obtained from the surface of the oxidized specimen could be attributed to the existence of NiAl along with NiO and Ni<sub>2</sub>Al<sub>3</sub> on the specimen surface after the interaction with simulated nuclear waste [14]. Presence of NiAl layer has also been detected just below the outermost layer of Al<sub>2</sub>O<sub>3</sub> during the characterization studies of aluminides formed on Ni-based superalloy 690 as described in earlier studies [123].

Table-5.4: Details of Raman spectroscopy results and their peak assignments

Raman peaks (in this study)/cm <sup>-1</sup>	Peaks in literature/cm <sup>-1</sup>	Reference	Phase
645	644.2	[86,85]	Al <sub>2</sub> O <sub>3</sub>
648	648	[86]	
483	492	[91]	NiFe <sub>2</sub> O <sub>4</sub>
490			
310	305	[95]	Cr <sub>2</sub> O <sub>3</sub>
313			
875	820–904	[95]	Cr <sup>+3</sup> & Cr <sup>+6</sup>

Table-5.5: Details of XPS peaks and their assignments

XPS peaks (in this study)/eV	Peaks in literature/eV	Reference	Phase
Al2p	74.4	[99]	Al <sub>2</sub> O <sub>3</sub>
	74.3		
	76.2	[96]	Native Al oxide
	76.7		
Cr2p	576.9	[117]	Cr <sub>2</sub> O <sub>3</sub> (2p <sub>3/2</sub> )
	586.7	[117]	Cr <sub>2</sub> O <sub>3</sub> (2p <sub>1/2</sub> )
O1s	528.9	[116]	Cr <sub>2</sub> O <sub>3</sub>
	531.1	[98,101,102]	Al <sub>2</sub> O <sub>3</sub>
	528.0	[116]	Cr <sub>2</sub> O <sub>3</sub>
	530.6	[98,101,102]	Al <sub>2</sub> O <sub>3</sub>

The major difference obtained between the two coatings performed by high Al and low Al was in the incorporation of Al content to the exposed sodium borosilicate glass. Inclusion of Al to the glass network was observed during the exposure with high Al containing coatings. Exposure of low Al containing coatings with sodium borosilicate glass did not reveal any incorporation of Al in the glass matrix. However, before reaching to the conclusion, it is prudent to examine the exposed borosilicate glass to support this argument.

Detailed analyses of sodium borosilicate glass that interacted with aluminized and thermally oxidized Alloy 690 specimens provide the information about structure of sodium borosilicate glass. Results of such analyses will be discussed in detail in Chapter-6. Structural changes of sodium borosilicate glass matrices are not desirable in the view of stability of vitrified nuclear waste product. Therefore, the optimized composition for pack aluminization is 2 wt.%-Al powder, 2 wt.%-NH<sub>4</sub>Cl and 96 wt.%-Al<sub>2</sub>O<sub>3</sub> powder.

The presence of Cr<sub>2</sub>O<sub>3</sub>, NiFe<sub>2</sub>O<sub>4</sub> and mixed oxides of Cr<sup>+3</sup> and Cr<sup>+6</sup> could be attributed to unaltered oxides formed on the surface during the oxidation treatment (1273 K for 8 hours) prior to the exposure in both the media. The existence of these phases along with Al<sub>2</sub>O<sub>3</sub> on the surface of the coated specimen even after prolonged exposure to both the media signifies the good stability of Al<sub>2</sub>O<sub>3</sub> layer.

## 5.5 Conclusions

The main conclusions in the present study can be drawn as follows:

1. The surface of aluminized (using low Al-containing pack) and thermally oxidized Alloy 690 specimen exposed to simulated nuclear waste consists of Al<sub>2</sub>O<sub>3</sub>, NiFe<sub>2</sub>O<sub>4</sub> mixed

oxide,  $\text{Cr}_2\text{O}_3$  and mixed oxides of  $\text{Cr}^{+3}$  and  $\text{Cr}^{+6}$  as revealed by Raman spectroscopy. Similar surface compositions were noticed for coated samples exposed to sodium borosilicate melt.

2. The XPS analysis showed that aluminized (using low Al-containing pack) and thermally oxidized Alloy 690 specimen interacted with simulated nuclear waste and sodium borosilicate melt contain  $\text{Al}_2\text{O}_3$  and  $\text{Cr}_2\text{O}_3$  on the surface.
3. The existence of  $\text{Al}_2\text{O}_3$  phase on the surface of the coated specimen even after prolonged exposure to simulated nuclear waste and sodium borosilicate melt indicated the good stability of aluminide coatings which is having  $\text{Al}_2\text{O}_3$  layer on top surface.
4. The optimized composition for pack aluminization is low Al (2 wt.%) containing pack as it provides good stability of aluminide coatings and borosilicate glass even after prolonged exposure.



# **Characterization of interacted sodium borosilicate glass**

---

---

## **6.1 Introduction**

In chapter 4 and 5, detailed surface characterization of coated specimens (prepared using high and low aluminium containing pack) that exposed to simulated nuclear waste and sodium borosilicate melt have been carried out and reported. In order to complete the analyses, sodium borosilicate glass, which was adhering to the coated specimens, was studied in this chapter. For this purpose, the glass was carefully removed, powdered and analyzed using FT-IR spectroscopy, Raman spectroscopy and XPS.

In the present study, borosilicate glasses have been used because, they are one of the most widely used matrices for immobilizing the radioactive ions present in the waste generated during the reprocessing of spent nuclear fuel. Borosilicate glasses are composed of the structural groupings present in the crystalline compounds associated with the glass-forming system and there are separate borate and silicate networks [135]. Based on the studies on the structural aspects of borosilicate glasses using various techniques like  $^{29}\text{Si}$ ,  $^{11}\text{B}$ ,  $^{17}\text{O}$  magic angle spinning nuclear magnetic resonance (MAS NMR), Raman and IR spectroscopy, the presence of structural units like trigonally coordinated boron ( $\text{BO}_3$ ), tetrahedrally coordinated boron ( $\text{BO}_4$ ), silicon atoms with 3 and 4 bridging oxygen atoms ( $\text{Q}^3$

and  $Q^4$ : where  $Q^n$  represents silicon structural units having  $n$ -number of bridging oxygen atoms),  $Q^n$  units with Si–O–B linkages etc. are well known. The addition of network modifiers (alkali/alkaline earth metal oxides) to borosilicate and borate glasses results in the initial conversion of  $BO_3$  to  $BO_4$  structural units [59]. Sodium borosilicate glass has ability to tolerate minor variations of waste composition. Moreover, its high chemical, mechanical and thermal stability, sufficient waste solubility, moderate processing temperatures (1273-1473 K) and more compatibility as host solid with the waste components makes it more suitable as matrices for nuclear waste immobilization [62-64].

Analyses of glass samples that exposed to high aluminum containing (10 wt.% Al) specimens and low aluminium containing (2 wt.% Al) specimens have discussed separately in detail in this chapter.

## **6.2 Experimental Methods**

The composition of the sodium borosilicate glass used in the present investigation is given in Chapter 3. Aluminized (high and low Al-containing packs) and thermally oxidized Alloy 690 specimens having dimensions of about 10 mm × 10 mm × 5 mm were exposed to sodium borosilicate melt at 1248 K for a total period of 192 h. Glass sample were taken from the vicinity of the aluminized and oxidized superalloy 690 specimen after the interaction experiments, were characterized using FT–IR spectroscopy, Raman spectroscopy and XPS techniques. The details experimental procedures and characterization techniques are also discussed in Chapter 3. Unreacted glass was also characterized using the above mentioned techniques, for comparison.

## 6.3 Results

### 6.3.1 Characterization of sodium borosilicate glass interacted with aluminized (with high Al-containing pack) and oxidized Alloy 690 specimen

Chemical composition of glass constituent elements in the vicinity of specimen/glass interface after interaction of glass with coated alloy was analyzed by energy dispersive X-ray spectroscopy (EDS) technique and is given Table-6.1. Since boron is a low Z element, it could not be analyzed quantitatively using EDS technique. Due to omission of B in glass phase during quantitative EDXS analysis, some overestimation of Si, Al and O was expected.

Table-6.1: Composition of glass constituent elements after interaction with coated alloy

Compositions of elements (at.%)							
O	Si	Al	Na	Ti	Ni	Cr	Fe
62.90	20.90	9.81	5.84	0.37	0.12	0.04	0.04

#### 6.3.1.1 FT-IR results

Mid-infrared spectra of both the reacted (with high Al containing coated specimen) and unreacted glasses are presented in Fig. 6.1. The observed bands could be attributed to the vibrational bands of specific groups. The broad absorption band observed in 900-1200  $\text{cm}^{-1}$  region corresponds to the combined stretching vibration of Si-O-Si and B-O-B tetrahedral network. Similarly the band at 1250-1500  $\text{cm}^{-1}$  region is attributed to stretching vibration of  $\text{BO}_3$  triangular units with non-bridging oxygen (NBO) [59,64,124-127]. The weaker band at

650-750  $\text{cm}^{-1}$  corresponds to the bending vibrations of bridging oxygen (BO) between trigonal  $\text{BO}_3$  groups [124,126, 64].

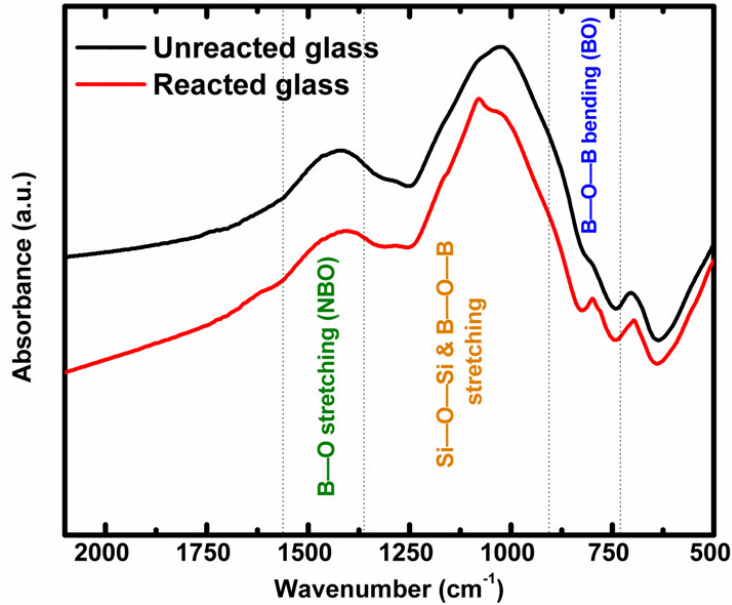


*Fig. 6.1. Mid-infrared absorption spectrum of sodium borosilicate glass interacted with aluminized (with high Al containing pack) and thermally oxidized Alloy 690 specimen indicating different structural silicate and borate chains. Spectrum of unreacted glass is also shown for comparison.*

Aforementioned mid-infrared bands are strong and broad, and overlap on the weak Al–O bands, whereas in far-infrared region (Fig. 6.2), the distinct spectral features of Longitudinal Optical (LO) and Transverse Optical (TO) stretching and bending Al–O vibrations have been observed. An intense band appeared at  $460 \text{ cm}^{-1}$  is typical of the Al–O stretching mode of  $\text{Al}_2\text{O}_3$  (LO mode). A prominent peak at  $372.4 \text{ cm}^{-1}$  corresponds to bending mode of Al–O vibration (TO) [128-130]. Similarly, weaker bands at  $395 \text{ cm}^{-1}$ ,  $506 \text{ cm}^{-1}$  and  $435 \text{ cm}^{-1}$  assigned to the Al–O bending vibrations with TO, LO and TO modes respectively [128,129].

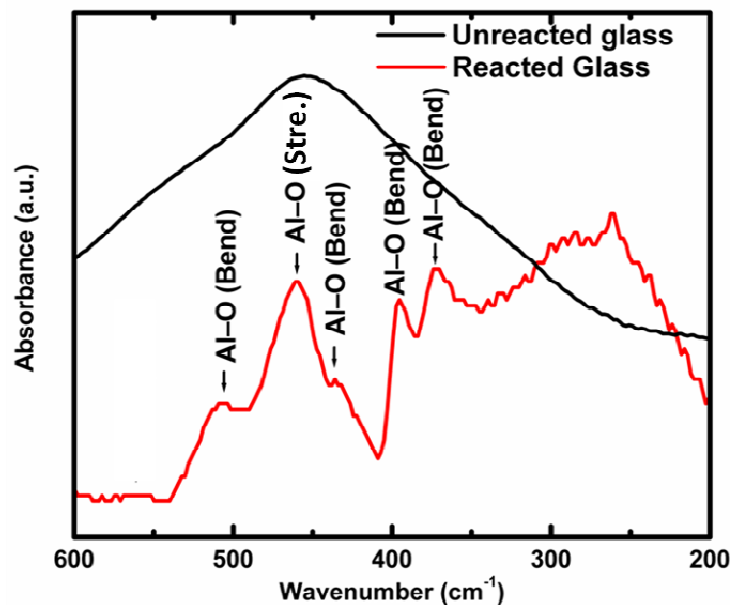


*Fig. 6.2. Far-infrared absorption spectrum of sodium borosilicate glass interacted with aluminized (with high Al containing pack) and thermally oxidized Alloy 690 specimen showing distinct spectral features of Al–O stretching and bending vibration bands. Spectrum of unreacted glass is also shown.*

### 6.3.1.2 XPS spectra

Fig.6.3 shows the XPS survey spectra of unreacted sodium borosilicate glass, and that glass which interacted with aluminized (with high Al containing pack) and thermally oxidized Alloy 690 substrates. Photoelectron spectra for O1s of unreacted and reacted glasses are shown in Figs. 6.4(a) and 6.4(b) respectively. There are two separate peaks in the spectrum of unreacted glass at 529.8 eV and 531.0 eV as shown in Fig. 6.4(a) corresponds to NBO and BO atom respectively. But in the spectrum of reacted glass (Fig. 6.4(b)), only one peak at 530.7 eV representing BO atom was observed. No peak corresponds to NBO atom was noticed in the O1s spectrum of reacted glass.

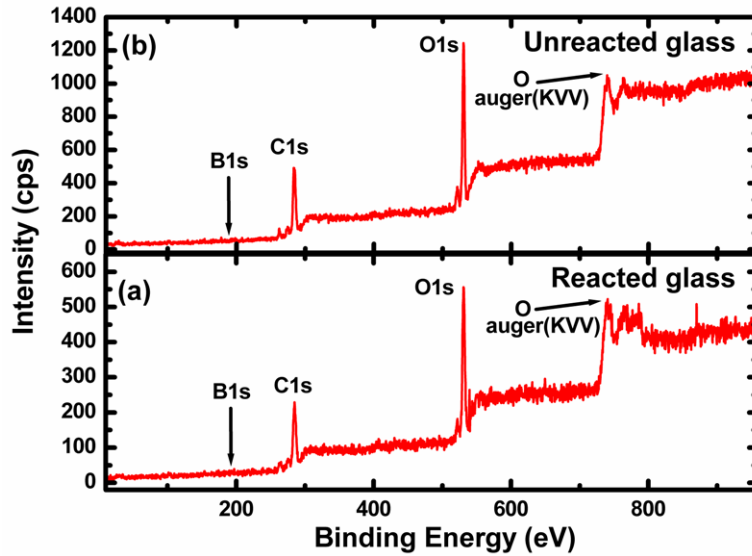


Fig. 6.3. XPS survey spectra of (a) sodium borosilicate glass that interacted with aluminized (with high Al containing pack) and thermally oxidized Alloy 690 specimen and (b) unreacted sodium borosilicate glass.

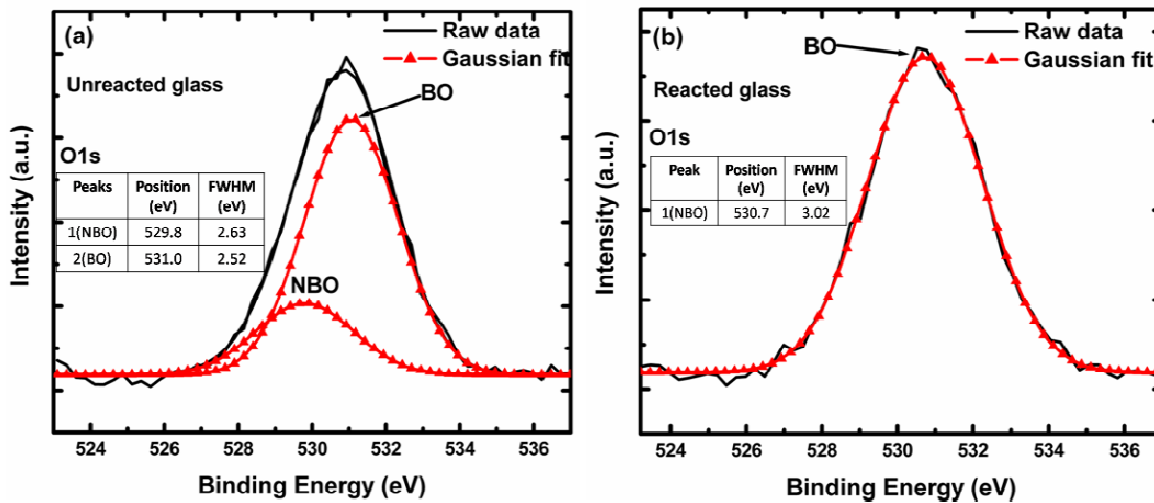


Fig. 6.4. O1s photoelectron spectrum of (a) unreacted sodium borosilicate glass and (b) glass interacted with aluminized (with high Al containing pack) and thermally oxidized Alloy 690 specimen. Non-bridging oxygen (NBO) component has disappeared from spectrum of reacted glass due to incorporation of  $Al^{+3}$  in the glass structure.

Photoelectron spectra for B1s of unreacted and reacted sodium borosilicate glass are shown in Figs. 6.5(a) and 6.5(b), respectively. The binding energy peak was obtained at 190.2 eV for unreacted glass (Fig. 6.5(a)). The binding energy of B1s peak for reacted glass shifts towards the higher energy side and occurred at 191.9 eV as is evident from Fig. 6.5(b). No change in X-ray photoelectron spectra on Si2p, Ti2p and Fe2p were observed on sodium borosilicate glass after interaction with coated and thermally oxidized alloy 690.

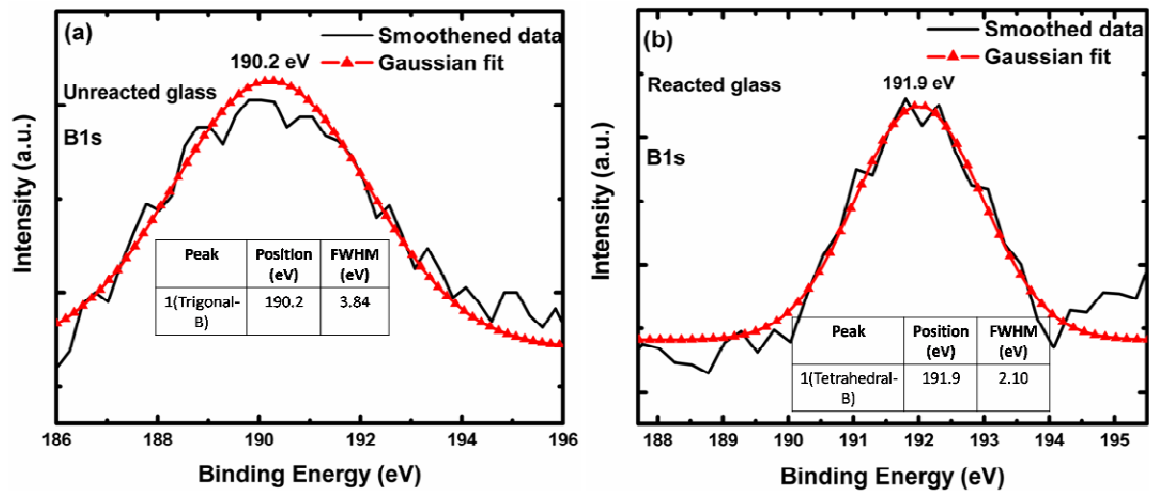


Fig. 6.5. B1s photoelectron spectrum of (a) unreacted sodium borosilicate glass and (b) glass interacted with aluminized (with high Al containing pack) and thermally oxidized Alloy 690 specimen. Chemical shift towards higher energy side in reacted glass is due to decrease in electron density on boron atom after conversion of trigonal boron to tetrahedral boron.

### 6.3.2 Glass interacted with aluminized (with low Al-containing pack) and oxidized Alloy 690 specimen

#### 6.3.2.1 Micro-Raman spectra

Micro-Raman spectra of reacted (with low Al containing coated specimen) and unreacted glasses were recorded and are described in Fig. 6.6. Four broad peaks were

observed in Raman spectra of both reacted and unreacted glasses. No additional bands were observed in Raman spectra of sodium borosilicate glass that interacted with aluminized and thermally oxidized Alloy 690 substrate. The peak obtained at around  $460\text{ cm}^{-1}$  corresponds to bending of Si–O–Si bonds and mixed Si–O–B bonds of the three-dimensional network [131].

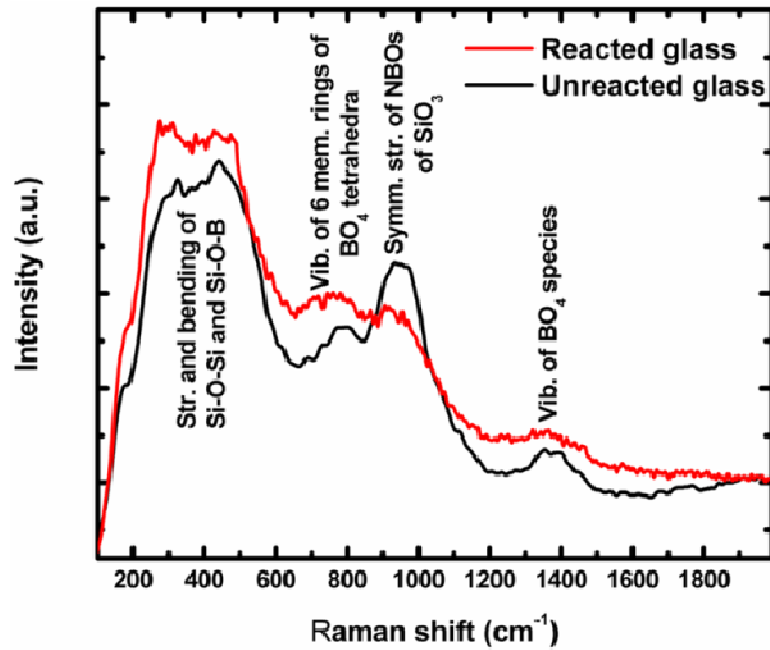


*Fig. 6.6. Micro-Raman spectra of sodium borosilicate glass interacted with aluminized (with low Al containing pack) and thermally oxidized Alloy 690 specimen indicating different structural silicate and borate units. Spectra of unreacted glass are also shown.*

A peak occurred at about  $770\text{ cm}^{-1}$  corresponds to the symmetric breathing vibration of six-membered rings of  $\text{BO}_4$  tetrahedra [131-132]. A band observed at around  $945\text{ cm}^{-1}$  is mainly due to the symmetric stretching mode of the non-bridging bonds (NBO) of  $\text{SiO}_3$  chain units [131]. Another weak band obtained at around  $1350\text{ cm}^{-1}$  is corresponds to the vibrations of  $\text{BO}_4$  species [63].

### 6.3.2.2 XPS spectra

XPS survey spectra of sodium borosilicate glass that interacted with aluminized (with low Al containing pack) and thermally oxidized Alloy 690 substrates and that of unreacted glass are shown in Fig. 6.7. Similar spectra have been obtained for both reacted and unreacted glasses. The high resolution XPS spectra were recorded for 1s level of O and B and 2p<sub>3/2</sub> level of Si. The O1s XPS spectrum of unreacted glass (Fig. 6.8a) consists of two peaks. The first peak occurred at 529.9 eV corresponding to NBO atom and the second the second peak occurred at 530.9 eV is corresponding to BO.

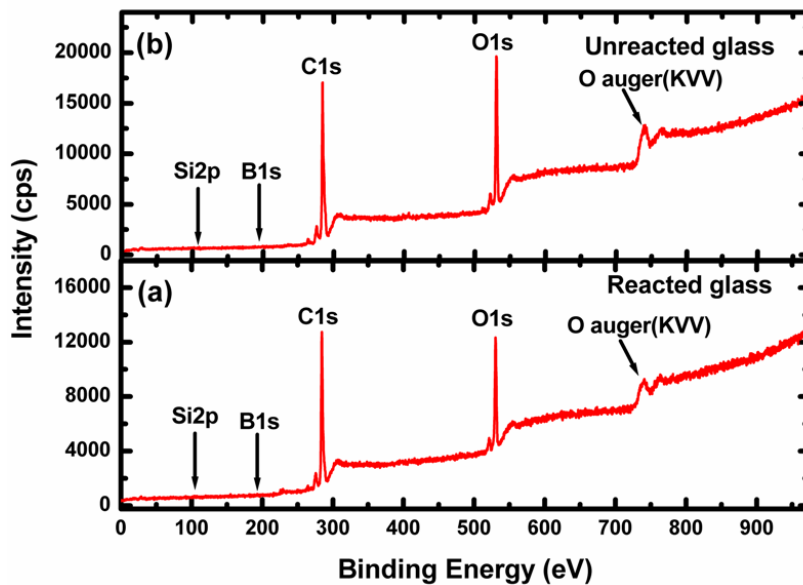


*Fig. 6.7. XPS survey spectra of (a) sodium borosilicate glass that interacted with aluminized (with low Al containing pack) and thermally oxidized Alloy 690 specimen and (b) unreacted sodium borosilicate glass.*

Similarly, O1s spectrum of reacted (with low Al containing pack) glass (Fig. 6.8b) also showed two peaks at 529.8 and 530.8 eV correspond to NBO and BO atom respectively

[133,134]. Si2p<sub>3/2</sub> XPS spectra of unreacted and reacted (with low Al containing pack) glass, as shown in Fig. 6.9 (a & b) showed the peaks at 103.3 and 103.5 eV respectively. B1s spectra of unreacted and reacted (with low Al containing pack) glass indicated the peaks at 192.6 and 192.8 eV respectively (Fig. 6.10 (a & b)).

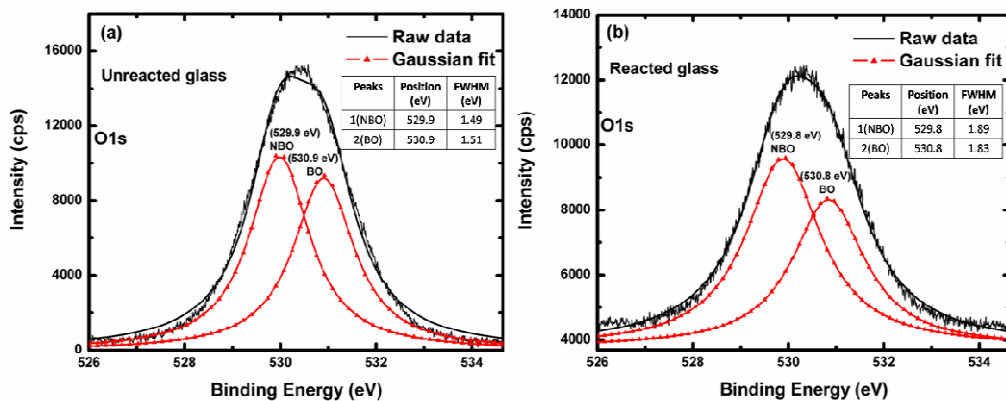


Fig. 6.8. O1s XPS spectra of (a) unreacted sodium borosilicate glass and that of (b) sodium borosilicate glass that reacted with aluminized (with low Al containing pack) and thermally oxidized Alloy 690 substrate, showing the peaks of NBO and BO.

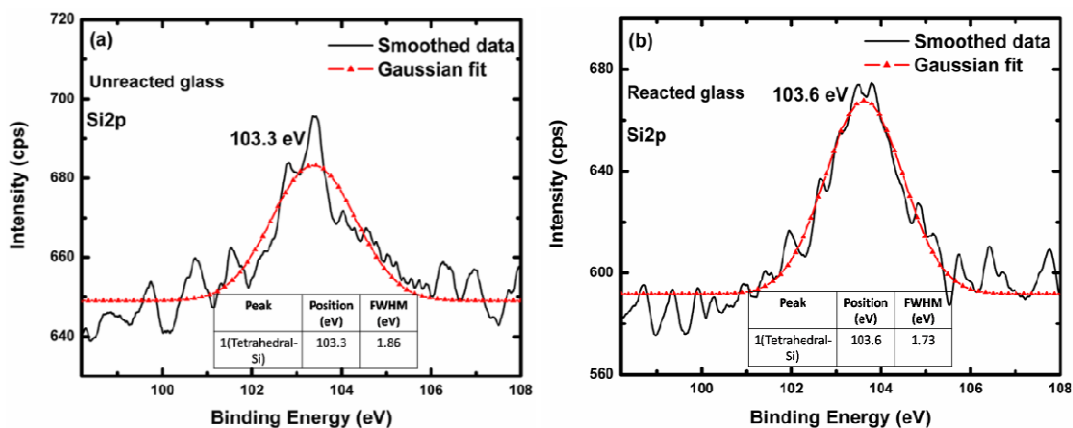


Fig. 6.9. Si2p XPS spectra of (a) unreacted sodium borosilicate glass and that of (b) sodium borosilicate glass that reacted with aluminized (with low Al containing pack) and thermally oxidized Alloy 690 substrate.

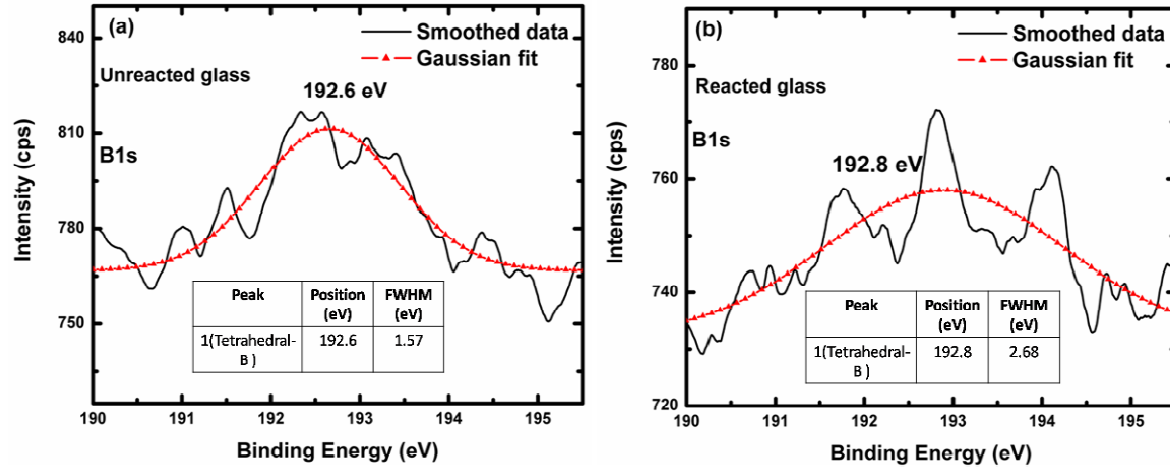


Fig. 6.10. B1s XPS spectra of (a) unreacted sodium borosilicate glass and that of (b) sodium borosilicate glass that reacted with aluminized (with low Al containing pack) and thermally oxidized Alloy 690 substrate.

## 6.4 Discussions

Salient features of the present investigation on borosilicate glass are as follows:

- FTIR studies of sodium borosilicate glass that interacted with aluminized (with high Al containing pack) and thermally oxidized Alloy 690 specimen revealed the incorporation of  $Al^{+3}$  in the glass network.
- XPS analyses of borosilicate glass that interacted with aluminized (with high Al containing pack) and thermally oxidized Alloy 690 specimen also indicated structural modification of the glass due to inclusion of  $Al^{+3}$  in the glass network.
- Raman spectroscopy and XPS analyses of sodium borosilicate glass that interacted with aluminized (with low Al containing pack) and thermally oxidized Alloy 690 specimen showed that, there is no change in the structure of the glass after exposure with coated specimen.

Various bands in the mid-infrared spectra of sodium borosilicate glass interacted with aluminized (with high Al-containing pack) Alloy 690 specimen having  $\text{Al}_2\text{O}_3$  layer on surface compare well with spectra available in the literature [59, 64,124]. Mishra et al. [59] have studied the effect of BaO addition on the structural aspects of sodium borosilicate glasses and observed broad peaks around  $1400\text{ cm}^{-1}$ ,  $1000\text{ cm}^{-1}$  and  $450\text{ cm}^{-1}$  and assigned these bands to the stretching vibration of the B–O linkages present in various boron structural units, asymmetric stretching vibration of Si–O–Si/Si–O–B linkages and bending vibration of Si–O–Si/ Si–O–B linkages respectively. Goel et al. [64] have performed the structural analysis of sodium alumino-borosilicate-based simulated high-level nuclear waste glass using FT-IR spectroscopy. The authors [64] have reported the transmittance bands at  $800\text{-}1300\text{ cm}^{-1}$  region (correspond to the stretching vibrations of the  $\text{SiO}_4$  tetrahedron with a different number of BO atoms),  $300\text{-}600\text{ cm}^{-1}$  region (due to bending vibrations of Si–O–Si and Si–O–Al linkages),  $1350\text{-}1500\text{ cm}^{-1}$  region (assigned to B–O vibrations in the  $\text{BO}_3$  triangle) and  $650\text{-}800\text{ cm}^{-1}$  region (correspond to bending vibrations of BO between triangular boron atoms). IR absorption spectra of sodium barium borosilicate glasses have been recorded by Mohapatra et al. [124] during their investigation of electron beam irradiation effects in sodium barium borosilicate glasses, which is the base glass for immobilization of nuclear high level radioactive waste, and noticed identical features.

The features of Al–O peaks observed in far-infrared spectra of reacted (with high Al containing coated specimen) glass can be attributed to the modified glass structure occurred due to the incorporation of  $\text{Al}^{3+}$  in the glass structure. There is also a possibility that some of the  $\text{Al}_2\text{O}_3$  molecules from the  $\text{Al}_2\text{O}_3$  layer at the surface of aluminide layers might diffuse in the glass during the interaction period. Some enrichment of aluminium in sodium borosilicate

Table-6.2: Details of FTIR peaks and their assignments

FTIR bands (in this study) /cm <sup>-1</sup>	Peaks in literature /cm <sup>-1</sup>	Reference	Phase
900–1200	1000	[59,64,124–127]	Str. Vib. of Si–O–Si and B–O–B
1250-1500	1400	[59,64,124–127]	BO <sub>3</sub> triangular units with NBO
650-750	650–800	[64,124,]	Bend. Vib. BO between triagonal BO <sub>3</sub> groups
460	457	[130]	Al–O stretching (LO)
372.4	379.8	[128–129,130]	Al–O bending (LO)
395	397.5	[128,129]	Al–O bending (TO)
506	510.9	[128,129]	Al–O bending (LO)
435	439.1	[128,129]	Al–O bending (TO)

glass phase close to coating/glass interface is noticed after the interaction with thermally oxidized aluminide coating on Alloy 690 substrate for a prolonged period of 192 hours has been reported by Dutta et al. [11]. The present results are in agreement with the observations of Peng et al. [128] who carried out a study of vibrational modes of stressed alumina films formed by heating Fe<sub>3</sub>Al under different oxidizing atmospheres using FT-IR spectroscopy. Details of FTIR results obtained in this study and those reported in the literature are summarized in Table-6.2.

The disappearance of NBO component in the O1s photoelectron spectra of reacted glass can be explained on the basis of the findings of Miura et al. [135] who have carried out XPS of sodium borosilicate glasses. The authors [135] have reported that NBO component does not appear in the XPS spectra at the region where  $R (= Na_2O/B_2O_3)$  is smaller than 0.6

for  $K (= \text{SiO}_2/ \text{B}_2\text{O}_3) \geq 2.0$ . In the present study  $R= 0.4$  and  $K= 1.8$ , and incorporation of Al in the glass network was confirmed by FT-IR studies. Jean et al. [71] carried out the interfacial reaction between borosilicate glass (BSG) and sapphire ( $\alpha\text{-Al}_2\text{O}_3$ ) and noticed the built up of interdiffusion layer at the sapphire/BSG interface that moves towards BSG with reaction time. The interdiffusion layer at the interface is rich in  $\text{Al}^{+3}$ ,  $\text{K}^+$ , and poor in  $\text{Si}^{+4}$  in a glassy matrix whose composition is different from BSG. They [71] have proposed that, the  $\text{Al}^{+3}$  substitutes  $\text{Si}^{+4}$  in BSG and forms  $[\text{AlO}_{4/2}]^{-1}$  tetrahedra, in which  $\text{Al}^{+3}$  acts as a glass network former and the negative charge is compensated by alkali ions in BSG. This necessity of charge compensation provides an electrochemical driving force for alkali ions to undergo diffusion from BSG to interdiffusion layer. According to the Dell model [136], in the region of  $R < 0.5$  the oxide ions from sodium oxides enter predominantly in borate network to form tetrahedral  $\text{BO}_4$  groups, regardless of the silica content. Smedskjaer et al. [137] have reported the conversion of trigonal boron to tetrahedral boron without NBO formation by addition of  $\text{Na}_2\text{O}$  to  $\text{B}_2\text{O}_3$  glasses. Similarly El-Damrawi et al. [138] have explained the removal of NBOs due to addition of  $\text{Al}_2\text{O}_3$  to alkali silicate glasses. Therefore, the finding of disappearance of NBO peak in the spectrum of reacted glass as observed in the present investigation is in agreement with the results of other investigators [135,137-138]. The modified glass structure due to incorporation of  $\text{Al}^{3+}$  ion has been shown pictorially in Fig. 6.11. A small shift of B1s photoelectron peak of reacted glass towards higher energy was noticed, which could be because of decrease in electron density on boron atom after conversion of trigonal boron to tetrahedral boron. Details of XPS peaks obtained in the present study and those reported in literature are given in Table-6.3.

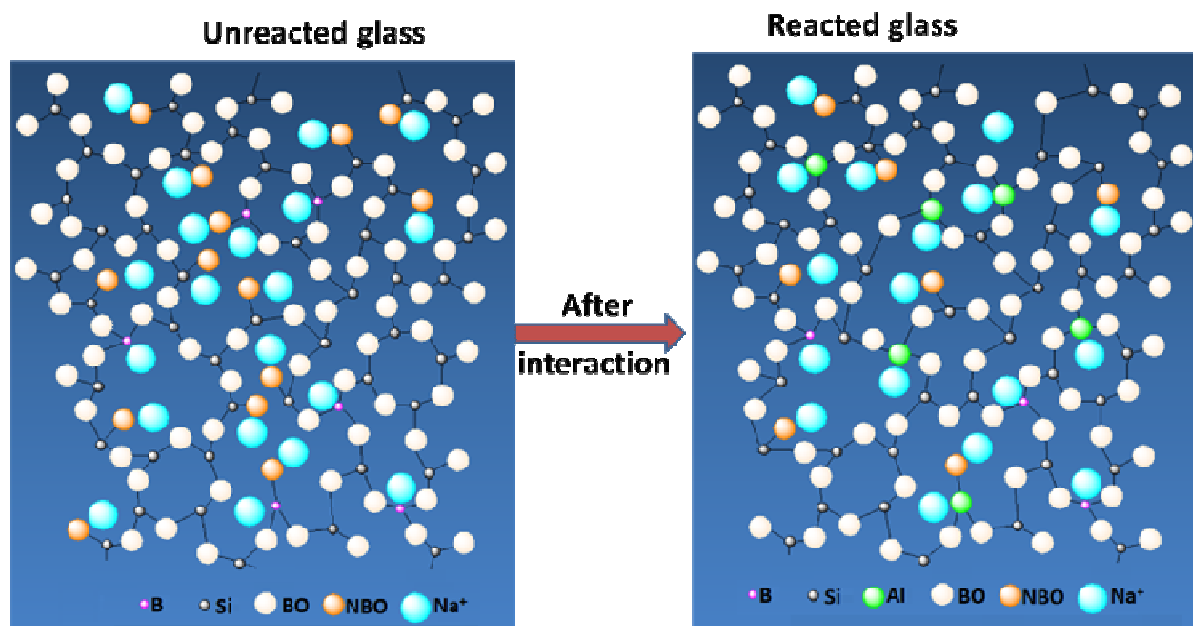


Fig. 6.11. Pictorial representation of modified sodium borosilicate glass structure due to incorporation of  $Al^{3+}$  from high Al containing coating.

Table-6.3: Details of XPS peaks and their assignments

XPS peaks (in this study) / (eV)		Peaks in literature / eV	Reference	Phase
O1s-unreacted	529.8	529.2	[135]	NBO
	531.0	531.1	[135]	BO
O1s-reacted	530.7	531.1	[135]	BO
B1s-unreacted	190.2	191.1	[135]	Trigonal B
B1s-reacted	191.9	-	-	Tetrahedral B

Miro-Raman replaced with spectroscopy analysis of sodium borosilicate glass that interacted with aluminized (with low Al-containing pack) and thermally oxidized Alloy 690 substrate and unreacted glass have revealed the similar spectra and indicated the presence of several structural units present in the glass network. Furukawa et al. [131] have investigated the structure of borosilicate glass by using Raman spectroscopy as the primary tool. The authors [131] have observed a dominant feature as a broad band at  $550$  to  $450\text{ cm}^{-1}$ , which is

due to bending or rocking of Si–O–Si bonds as well as mixed Si–O–B bonds of the three-dimensional network. Another band occurred at 950 to 975  $\text{cm}^{-1}$  mainly due to the symmetric stretching mode of the non-bridging bonds of  $\text{SiO}_3$  chain units [131]. Maniu et al. [132] have studied the influence of CaO content on the structure of borate glasses by using Raman spectroscopy. They [132] have reported a band at 770  $\text{cm}^{-1}$  in the Raman spectra, which was assigned to the symmetric breathing vibration of six-member rings with one  $\text{BO}_4$  tetrahedron. Effects of the iron content and redox state on the structure of sodium borosilicate glasses were investigated by Cochain et al. [63]. The researchers [63] have obtained a high-frequency band at about 1380  $\text{cm}^{-1}$ , which involves the vibrations of  $\text{BO}_4$  species and was attributed to  $\text{BO}_2\text{O}^-$  linked to  $\text{BO}_4^-$ . Therefore, it is clear that the present results from micro-Raman spectroscopy are in agreement with the observations of other researchers [63,131,132]. Details of Raman spectroscopy results obtained in the present study and those reported in the literature are summarized in Table-6.4. O1s, Si2p and B1s XPS spectra of sodium borosilicate glass that interacted with aluminized (with low Al-containing pack) and thermally oxidized Alloy 690 substrate and unreacted glass have shown the binding energy peaks at similar positions. Nesbitt et al. [133] have reported the binding energy range, 529–532 eV corresponds to BO and NBO contributions during the bridging, non-bridging and free oxygen estimation studies of  $\text{Na}_2\text{O}$ – $\text{SiO}_2$  glasses. Therefore the identified peaks in O1s XPS spectra of both unreacted and reacted glass to BOs and NBOs is in accordance with the literature [133,134,135]. Details of XPS results obtained in the present study and those reported in the literature are given in Table-6.5.

Table-6.4. Raman spectroscopy results and their peak assignments

Raman peaks (in this study)/cm <sup>-1</sup>	Peaks in literature/cm <sup>-1</sup>	Reference	Phase
460	450–550	[131]	Str. and bend. of Si–O–Si and Si–O–B
770	770	[131,132]	Vib. of 6 mem. rings of BO <sub>4</sub> tetrahedra
945	950–975	[131]	Symm. str. of NBOs of SiO <sub>3</sub>
1350	1380	[63]	Vib. of BO <sub>4</sub> species

Table-6.5. Details of XPS peaks and their assignments

XPS peaks (in this study) /eV	Peaks in literature /eV	Reference	Phase	
O1s-unreacted	529.9	529.2	[135]	NBO
	530.9	531.1	[135]	BO
O1s-reacted	529.8	529.2	[135]	NBO
	530.8	531.1	[135]	BO
Si2p-unreacted	103.3	103.0	[135]	Tetrahedral Si
Si2p-reacted	103.5	103.0	[135]	Tetrahedral Si
B1s-unreacted	192.6	191.1	[135]	Trigonal B
B1s-reacted	192.8	191.1	[135]	Trigonal B

Based on all these findings, it may be summarized that the interaction of aluminized (with high Al-containing pack) and thermally oxidized superalloy 690 substrate having Al<sub>2</sub>O<sub>3</sub> layer on top with sodium borosilicate glass resulted the modified glass structure because of incorporation of Al<sup>+3</sup> in the glass network. On the other hand, the Raman spectroscopy and XPS studies of sodium borosilicate glass that interacted with aluminized (with low Al-containing pack) and thermally oxidized Alloy 690 substrate, indicated that, there is no change in the structure of sodium borosilicate glass after prolonged exposure. This showed that, there is no elemental or molecular incorporation from the coated specimen to the glass network structure. Therefore, the low Al containing pack aluminization

composition (2 wt.% Al, 2 wt.% NH<sub>4</sub>Cl and 96 wt.% Al<sub>2</sub>O<sub>3</sub>) is acceptable for preparation of aluminized coatings on Alloy 690 specimens, that is used in metallic and ceramic melter pots for the vitrification of high level nuclear waste.

## 6.5 Conclusions

The following conclusions can be drawn from this chapter:

1. Mid-infrared and far-infrared spectroscopy, and X-ray photoelectron spectroscopy (O1s and B1s) on sodium borosilicate glass interacted with aluminized (with high Al-containing pack) and thermally oxidized Alloy 690 with Al<sub>2</sub>O<sub>3</sub> layer on top indicates modified glass structure due to inclusion of Al<sup>+3</sup> in glass structure.
2. Besides aluminium, no substantial elemental transfer from coating to glass phase is observed.
3. Micro-Raman spectroscopy and XPS analysis of sodium borosilicate glass that interacted with aluminized (with low Al-containing pack) and thermally oxidized Alloy 690 substrates indicated no elemental or molecular incorporation from the coated specimen to the glass, and therefore no structural modification of the glass network after the prolonged exposure.
4. Low Al containing pack aluminization composition (2 wt.% Al, 2 wt.% NH<sub>4</sub>Cl and 96 wt.% Al<sub>2</sub>O<sub>3</sub>) is acceptable for synthesis of aluminized coatings on Alloy 690 specimens, that is used in metallic and ceramic melter pots for the vitrification of high level nuclear waste.

### Summary and future scope

---

This chapter discusses the summary of the present work and also the scope for the future work. In the present work, aluminized (using high/low Al-containing pack) and thermally oxidized Alloy 690 substrates and bare specimens have been exposed to simulated nuclear waste and sodium borosilicate melt. Important findings are summarized below:

- Surface of aluminized (using high Al-containing pack) and thermally oxidized Alloy 690 specimen exposed to simulated nuclear waste consists of  $\text{Al}_2\text{O}_3$ ,  $\text{NiCr}_2\text{O}_4$  and  $\text{NiFe}_2\text{O}_4$  mixed oxides,  $\text{NiO}$ ,  $\text{Cr}_2\text{O}_3$ , mixed oxides of  $\text{Cr}^{+3}$  and  $\text{Cr}^{+6}$  and elemental aluminium. Similar surface compositions were also noticed for coated samples exposed to sodium borosilicate melt. Sodium borosilicate glass that exposed with aluminized and oxidized Alloy 690 specimen having high aluminium content indicated modified glass structure due to incorporation of  $\text{Al}^{+3}$  in the glass network.
- The surface composition of coated specimen exposed to simulated nuclear waste is similar to that exposed in sodium borosilicate melt. This could be attributed to the unaltered mixed oxides that were formed on the surface of the specimens during pre-oxidation treatment.
- Alloy 690 bare substrates exposed to simulated nuclear waste, Raman spectroscopy indicated the presence of  $\gamma\text{-Fe}_2\text{O}_3$ ,  $\text{NiO}$ , some amount of  $\text{Cr}_2\text{O}_3$ , mixed oxides of  $\text{Cr}^{+3}$  and  $\text{Cr}^{+6}$  and elemental nickel and chromium, whereas bare substrate exposed

to borosilicate melt reveal similar composition along with the presence of thick  $\text{Cr}_2\text{O}_3$  layer, mixed oxides of  $\text{NiCr}_2\text{O}_4$  and  $\text{NiFe}_2\text{O}_4$ . The presence of mixed oxides for substrate exposed in molten glass is due to high temperature (1248 K) exposure.

- Aluminized (using low Al-containing pack) and thermally oxidized Alloy 690 specimen exposed to simulated nuclear waste contains of  $\text{Al}_2\text{O}_3$ ,  $\text{NiFe}_2\text{O}_4$  mixed oxide,  $\text{Cr}_2\text{O}_3$  and mixed oxides of  $\text{Cr}^{+3}$  and  $\text{Cr}^{+6}$ . Whereas coated specimens exposed to sodium borosilicate melt reveal similar surface compositions. Sodium borosilicate glass exposed with coated specimens having low aluminium content indicated no structural modification of the glass network after the prolonged exposure.
- The existence of  $\text{Al}_2\text{O}_3$  phase on the surface of the coated specimen even after prolonged exposure to simulated nuclear waste and sodium borosilicate melt indicated the good stability of aluminide coatings which is having  $\text{Al}_2\text{O}_3$  layer on top surface.
- Low Al containing pack aluminization composition (2 wt.% Al, 2 wt.%  $\text{NH}_4\text{Cl}$  and 96 wt.%  $\text{Al}_2\text{O}_3$ ) is acceptable for synthesis of aluminized coatings on Alloy 690 specimens, that is used in metallic and ceramic melter pots for the vitrification of high level nuclear waste.

### **Scope for future work**

In actual service condition, the temperature of HLW can go upto 393K. Therefore, it is prudent to carry out the exposure to synthetic waste at higher temperature to understand the worst case scenario. The present work can be extended by studying the interaction of

different aluminide coated Ni–Cr–containing, Fe–Ni–Cr containing superalloys in corrosive environments pertinent to high temperature applications.



## References

- 
- [1] M.A. Audero, A.M. Bevilacqua, N.B.M. de Bernasconi, D.O. Russo, M.E. Sterba, *J. Nucl. Mater.* 223 (1995) 151.
- [2] C.P. Kaushik, R.K. Mishra, P. Sengupta, Amar Kumar, D. Das, G.B. Kale, Kanwar Raj, *J. Nucl. Mater.* 358 (2006) 129.
- [3] K. Raj, K.K. Prasad, N.K. Bansal, *Nucl. Eng. Des.* 236 (2006) 914.
- [4] P. Sengupta, D. Rogalla, H.W. Becker, G.K. Dey, S. Chakraborty, *J. Hazard. Mater.* 192 (2011) 208.
- [5] J.Di Martino, C. Rapin, P. Berthod, R. Podor, P. Steinmetz, *Corros. Sci.* 46 (2004) 1849.
- [6] J.Di Martino, C. Rapin, P. Berthod, R. Podor, P. Steinmetz, *Corros. Sci.* 46 (2004) 1865.
- [7] A. Carton, C. Rapin, R. Podor, P. Berthod, *J. Electrochem. Soc.* 153 (2006) 121.
- [8] C. Rapin, M. Vilasi, R. Podor, A. Carton, B. Gaillard-Allemand, P. Berthod, P. Steinmetz, *Mater. Sci. Forum* 461-464 (2004) 1125.
- [9] H. Khedim, S. Abdelouhab, R. Podor, C. Rapin, M. Vilasi, P.-J. Panteix, M. Toplis, F. Faure, *J. Non-Cryst. Solids* 357 (2011) 31.
- [10] S. Abdelouhab, C. Rapin, R. Podor, P. Berthod, M. Vilasi, *J. Electrochem. Soc.* 154 (2007) 500.
- [11] R.S. Dutta, C. Yusufali, B. Paul, S. Majumdar, P. Sengupta, R.K. Mishra, C.P. Kaushik, R.J. Kshirsagar, U.D. Kulkarni, G.K. Dey, *J. Nucl. Mater.* 432 (2013) 72.
- [12] V. Kain, P. Sengupta, P.K. De, S. Banerjee, *Metall. Mater. Trans. A* 36 A (2005) 1075.

- 
- [13] R.S. Dutta, S. Majumdar, P.K. Limaye, U.D. Kulkarni, G.K. Dey, *Trans. IIM* 64 (2011) 31.
- [14] R.S. Dutta, C. Yusufali, S. Majumdar, R.K. Mishra, C.P. Kaushik, R.J. Kshirsagar, U.D. Kulkarni, G.K. Dey, *Mater. Sci. Forum* 710 (2012) 733.
- [15] G.B. Balazs, C. Rüssel, *J. Non-Cryst. Solids* 105 (1988) 1.
- [16] S.K. Sundaram, J.Y. Hsu, R.F. Speyer, *J. Am. Cer. Soc.* 78 (1995) 1940.
- [17] Y. Miura, K. Takahashi, *J. Non-Cryst. Solids* 38 (1980) 347.
- [18] D. Lizarazu, P. Steinmetz, J.L. Bernard, *Mater. Sci. Forum* 251 (1996) 709.
- [19] W. Minquan, G.E. Manzen, C. Feng, Y.U. Zhichu, T. Ying, *J. Non-Cryst. Solids* 80 (1986) 379.
- [20] R. Eck, *Ceram. Eng. Sci. Proc.* 6 (1985) 274.
- [21] K. Ooka, *J. Ceram. Soc. Japan* 72 (1964) 108.
- [22] S.K. Sundaram, J.Y. Hsu, R.E. Speyer, *J. Am. Cer. Soc.* 77 (1994) 1613.
- [23] P. Steinmetz, C. Rapin, *Mater. Sci. Forum* 369–372 (2001) 865.
- [24] C. Rapin, R. Podor, J. Gassert, M. Vilasi, *Mater. Sci. Forum* 595–598 (2008) 1119.
- [25] H. Khedim, S. Abdelouhab, R. Podor, C. Rapin, M. Vilasi, *Mater. Sci. Forum* 595–598 (2008) 621.
- [26] H. Khedim, R. Podor, C. Rapin, M. Vilasi, *J. Am. Ceram. Soc.* 91 (2008) 3571.
- [27] W. Thiemsorn, K. Keowkamnerd, P. Suwannathada, H. Hessenkemper, S.Phanichaphant, *Bull. Mater. Sci.* 30 (2007) 487.
- [28] J.Y. Tilquin, P. Duveiller, J. Glibert, P. Claes, *J. Non-Cryst. Solids* 211 (1997) 95.
- [29] J.Y. Tilquin, P. Duveiller, J. Glibert, P. Claes, *J. Non-Cryst. Solids* 224 (1998) 216.

- 
- [30] H. Khedim, T. Katrina, R. Podor, P.J. Panteix, C. Rapin, M. Vilasi, *J. Am. Ceram. Soc.* 93 (2010) 1347.
- [31] H. Khedim, R. Podor, P.J. Panteix, C. Rapin, M. Vilasi, *J. Non-Cryst. Solids* 356 (2010) 2734.
- [32] M.I. Ojovan, W.E. Lee, *New Developments in Glassy Nuclear Wasteforms*, Nova Science Publishers, 2007
- [33] R.K. Mishra, P. Sengupta, C.P. Kaushik, A.K. Tyagi, G.B. Kale, K. Raj, *J. Nucl. Mater.* 360 (2007) 143.
- [34] R.K. Mishra, V. Sudarsan, P. Sengupta, R.K. Vatsa, A.K. Tyagi, C.P. Kaushik, D. Das, K. Raj, *J. Am. Ceram. Soc.* 91 (2008) 3903.
- [35] P. Sengupta, S. Fanara, S. Chakraborty, *J. Hazard. Mater.* 190 (2011) 229.
- [36] P. Sengupta, C.P. Kaushik, G.K. Dey, Immobilization of high level nuclear Wwastes: the Indian Scenario, in: M. Ramkumar (Ed.), *On a Sustainable Future of the Earth's Natural Resources*, Springer-Verlag, Berlin, 2013.
- [37] P. Sengupta, J. Mitra, G.B. Kale, *J. Nucl. Mater.* 350 (2006) 66.
- [38] P. Sengupta, C.P. Kaushik, R.K. Mishra, G.B. Kale, *J. Am. Ceram. Soc.* 90 (2007) 3057.
- [39] P. Sengupta, C.P. Kaushik, G.B. Kale, D. Das, K. Raj, B.P. Sharma, *J. Nucl. Mater.* 392 (2009) 379.
- [40] P. Sengupta, *J. Nucl. Mater.* 411 (2011) 181.
- [41] H. Sahlaoui, H. Sidhom, J. Philbert, *Acta Mater.* 50 (2002) 1383.
- [42] D. Zhu, C.W. Kim, D.E. Day, *J. Nucl. Mater.* 336 (2005) 47.

- 
- [43] J.H. Hsu, J.W. Newkirk, C.W. Kim, C.S. Ray, R.K. Brow, M.E. Schlesinger, D.E. Day, *Corros. Sci.* 75 (2013) 148.
- [44] P. Sengupta, N. Soudamini, C.P. Kaushik, Jagannath, R.K. Mishra, G.B. Kale, K. Raj, D. Das, B.P. Sharma, *J. Nucl. Mater.* 374 (2008) 185.
- [45] M.I. Ojovan, W.E. Lee, *An Introduction to Nuclear Waste Immobilization*, Elsevier, The Netherlands, 2005.
- [46] P.K. Wattal, *Sadhana* 38 (2013) 849.
- [47] R.K. Mishra, Investigations of solubility of different nuclear waste constituents in glasses, their structural and physico-chemical characterization, PhD Thesis, University of Mumbai, Mumbai, 2008.
- [48] W.E. Lee, M.I. Ojovan, M.C. Stennett, N.C. Hyatt, *Adv. Appl. Ceram.* 105 (2006) 3.
- [49] I.W. Donald, *Waste immobilization in glass and ceramic based hosts*, Wiley, United Kingdom, 2010.
- [50] I.W. Donald, B.L. Metcalfe, R.N.J. Taylor, *J. Mater. Sci.* 32 (1997) 5851.
- [51] M.J. Plodinec, *Glass Technol.* 41 (2000) 186.
- [52] A. Paul, *Chemistry of glass*, Chapman and Hall, New York, 1990.
- [53] A.R. West, *Solid state chemistry and its applications*, Wiley, Singapore, 2003.
- [54] W.H. Zachariasen, *J. Am. Chem. Soc.* 54 (1932) 3841.
- [55] L. L. Hench, D. E. Clark, and J. Campbell, *Nucl. Chem. Waste Mgt.* 5 (1984) 149.
- [56] K.S. Chun, S.S. Kim, C.H. Kang, *J. Nucl. Mater.* 298 (2001) 150.
- [57] L. Dewan, L.W. Hobbs, J.M. Delaye, *J. Non-Cryst. Solids* 358 (2012) 3427.
- [58] H.G. Pfaender, *Schott Guide to Glass*, 2nd Ed., Chapman & Hall, New York, 1996.

- 
- [59] R.K. Mishra, V. Sudarsan, C.P. Kaushik, Kanwar Raj, S.K. Kulshreshtha, A.K. Tyagi, *J. Non-Cryst. Solids* 353 (2007) 1612.
- [60] J. Ramkumar, S. Chandramouleeswaran, V. Sudarsan, R.K. Mishra, C.P. Kaushik, Kanwar Raj, A.K. Tyagi, *J. Hazard. Mater.* 172 (2009) 457.
- [61] M.S. Gaafar, S.Y. Marzouk, *Physica B* 388 (2007) 294.
- [62] V.S. Yalmali, D.S. Deshingkar, P.K. Wattal, S.R. Bharadwaj, *J. Non-Cryst. Solids* 353 (2007) 4647.
- [63] B. Cochain, D. R. Neuville, G. S. Henderson, C. A. McCammon, O. Pinet, P. Richet, *J. Am. Ceram. Soc.* 95 (2012) 962.
- [64] A. Goel, J.S. McCloy, K.M. Fox, C.J. Leslie, B.J. Riley, *J. Non-Cryst. Solids* 358 (2012) 674.
- [65] M. Fábíán, E. Sváb, M.V. Zimmermann, *J. Non-Cryst. Solids* 380 (2013) 71.
- [66] M. Fábíán, E. Sváb, T. Proffen, E. Veress, *J. Non-Cryst. Solids* 354 (2008) 3299.
- [67] R.K. Mishra, R. Mishra, C.P. Kaushik, A.K. Tyagi, D. Das, K. Raj, *J. Nucl. Mater.* 392 (2009) 1.
- [68] R.K. Mishra, V. Sudarsan, C.P. Kaushik, K. Raj, S.K. Kulshreshtha, A.K. Tyagi, *J. Nucl. Mater.* 359 (2006) 132.
- [69] P. Sengupta, K.K. Dey, R. Halder, T.G. Ajithkumar, G. Abraham, R.K. Mishra, C.P. Kaushik, G.K. Dey, *J. Am. Ceram. Soc.* 98 (2015) 88.
- [70] M. Karabulut, G.K. Marasinghe, C.S. Ray, D.E. Day, O. Ozturk, G.D. Waddill, *J. Non-Cryst. Solids* 249(1999) 106.
- [71] J.H. Jean, T.K. Gupta, *J. Mater. Res.* 7 (1992) 2514.

- 
- [72] R. Bianco, R.A. Rapp, Pack cementation diffusion coatings, in: K.H. Stern (Ed.), Metallurgical and ceramic protective coatings, Chapman & Hall, London, 1996.
- [73] R.W. Cahn, P. Haasen and E.J. Kramer, Material science and engineering: Characterization of material, VCH Publisher Inc., New York (1991).
- [74] D. Naumann, Infrared spectroscopy in microbiology. In Encyclopedia of analytical chemistry: Applications, theory and instrumentation. Ed. R.A Meyers, pp. 102-131, Chichester; New York: Wiley (2000).
- [75] P.R. Griffiths, J.A. De Haseth, Fourier transform infrared spectrometry, New York: Wiley (1986).
- [76] B. Stuart, D.J. Ando, Modern infrared spectroscopy. New York: Published on behalf of ACOL (University of Greenwich) by Wiley (1996).
- [77] C.V. Raman, *Nature* 123 (1928) 50.
- [78] C.V. Raman, *Trans. Faraday Soc.* 25 (1929) 781.
- [79] K.S. Krishnan, *Nature* 122 (1928) 961.
- [80] P. F. J. d. Paula, Physical Chemistry, 8 ed. W. H. Freeman Company, New York, 2006.
- [81] H. C. Swart, G. L. P. Berning, *Mater Chem Phys.*, 41 (1995) 251.
- [82] J. H. Liu, R. Mendonça, R.W. Bosch, M.J. Konstantinovic, *J Nucl Mater.*, 393 (2009) 242.
- [83] J. M. Sanz, L. Soriano, P. Prieto, G. Tyuliev, C. Morant, E. Elizalde, *Thin Solid Films*, 332 (1998) 209.
- [84] T. L. Barr, Modern ESCA, The principle and practice of photoelectron spectroscopy, Ed: Tery Lynn Barr, CRC Press, 1994.

- 
- [85] R. Krishnan, R. Kesavamoorthy, S. Dash, A.K. Tyagi, B. Raj, *Scripta Mater.* 48 (2003) 1099.
- [86] A. Misra, H.D. Bist, M.S. Navati, R.K. Thareja, J. Narayan, *Mater. Sci. Eng. B* 79 (2001) 49.
- [87] P.V. Thomas, V. Ramakrishnan, V.K. Vaidyan, *Thin Solid Films* 170 (1989) 35.
- [88] V.F. Korzo, V.N. Cherhyaev, *Thin Solid Films* 34 (1976) 381.
- [89] T. Laha, K. Balani, A. Agarwal, S. Patil, S. Seal, *Metall. Mater. Trans. A* 36 (2005) 301.
- [90] K.R. Nagabhushana, B.N. Lakshminarasappa, F. Singh, *Bull. Mater. Sci.* 32 (2009) 515.
- [91] J.H. Kim, I.S. Hwang, *Nucl. Eng. Des.* 235 (2005) 1029.
- [92] Z. Wang, S.K. Saxena, P. Lazor, H.S.C. O'Neill, *J. Phys. Chem. Solids* 64 (2003) 425.
- [93] N. Mironova-Ulmane, A. Kuzmin, I. Steins, J. Grabis, I. Sildos, M. Pärs, *J. Phys.: Conf. Series* 93 (2007) 012039.
- [94] R.E. Dietz, G.I. Parisot, A.E. Meixner, *Phys. Rev. B* 4 (1971) 2302.
- [95] G.J. Abraham, R. Bhambroo, V. Kain, R. Shekhar, G.K. Dey, V.S. Raja, *Nucl. Eng. Des.* 243 (2012) 69.
- [96] C.D. Wagner, W.M. Riggs, L.E. Davis, J.F. Moulder and G.E. Muilenberg, *Handbook of X-ray photoelectron spectroscopy*, Perkin-Elmer corporation, Eden prairie, Minnesota, 1979.
- [97] K. Domen, T. J. Chuang, *J. Chem. Phys.* 90 (1989) 3318.
- [98] T. Gougousi, D. Barua, E.D. Young, G.N. Parsons, *Chem. Mater.* 17 (2005) 5093.

- 
- [99] J. Zähr, S. Oswald, M. TÜRpe, H.J. Ullrich and U. Füssel, *Vacuum* 86 (2012) 1216.
- [100] J. Koo, S. Kim, S. Kim, S. Jeon, H. Jeon, *J. Korean Phys.Soc.* 48, (2006) 131.
- [101] B. Lee, S.Y. Park, H.C. Kim, K. Cho, E.M. Vogel, M.J. Kim, R.M. Wallace, J. Kim, *App. Phys. Lett.* 92 (2008) 203102.
- [102] E. Paparazzo, *Appl. Surf. Sci.* 25 (1986) 1.
- [103] A. Ahlawat, V. G. Sathe, *J. Raman Spectrosc.* 42 (2011) 1087.
- [104] Y. Shi, J. Ding, Z.X. Shen, W.X. Sun, L. Wang, *Solid State Commun.* 115 (2000) 237.
- [105] P. R. Graves, C. Johnston, J. J. Campaniello, *Mater. Res. Bull.* 23 (1988) 1651.
- [106] S. Ramya, T. Anita, H. Shaikh, R.K. Dayal, *Corros. Sci.* 52 (2010) 2114.
- [107] S. Cava, S.M. Tebcherani, I.A. Souza, S.A. Pianaro, C.A. Paskocimas, E. Longo, J.A. Varela, *Mater. Chem. Phys.* 103 (2007) 394.
- [108] S. Uhlenbrock, C. Scharfschwerdt, M Neumann, G Illing, H-J. Freund, *J. Phys.: Condens. Matter* 4 (1992) 7973.
- [109] P.K. Samantaroy, G. Suresh, R. Paul, U.K. Mudali and B. Raj, *J. Nucl. Mater.* 418 (2011) 27.
- [110] K.S. Kim, N. Winograd, *Surf. Sci.* 43 (1974) 625.
- [111] L. Soriano, I. Preda, A. Gutiérrez, and S. Palacín, M. Abbate, A. Vollmer, *Phys. Rev. B* 75 (2007) 233417.
- [112] C. Yusufali, R.J. Kshirsagar, Jagannath, R.K. Mishra, R.S. Dutta and G.K. Dey, *J. Non-Cryst. Solids* 366 (2013) 54.
- [113] P.M. Sousa, A.J. Silvestre, N. Popovici, O. Conde, *Appl. Surf. Sci.* 247 (2005) 423.
- [114] I.R. Beattie, T.R. Gilson, *J. Chem. Soc. A* 5 (1970) 980.

- 
- [115] S.H. Shim, T.S. Duffy, R. Jeanloz, C.S. Yoo, V. Iota, *Phys. Rev. B* 69 (2004) 144107.
- [116] R.S. Dutta, A. Lobo, R. Purandare, S.K. Kulkarni and G.K. Dey, *Metall. Mater. Trans. A* 33 (2002) 1437.
- [117] B. Stypuła, J. Stoch, *Corros. Sci.* 36 (1994) 2159.
- [118] M. C. Biesinger, C. Brown, J. R. Mycroft, R. D. Davidson, N. S. McIntyre, *Surf. Interface Anal.* 36 (2004) 1550.
- [119] B.P. Payne, M.C. Biesinger, N.S. McIntyre, *J. Electron Spectrosc. Relat. Phenom.* 184 (2011) 29.
- [120] K.F. McCarty, D.R. Boehme, *J. Solid State Chem.* 79(1989) 19.
- [121] NIST-JANAF THERMOCHEMICAL TABLES, *J. Phys. Chem. Ref. Data, Monograph 9*, Page no. 973 & 1248.
- [122] D.G. Archer, *J. Phys. Chem. Ref. Data* 28 (1999)1485.
- [123] R.S. Dutta, A. Arya, C. Yusufali, B. Vishwanadh, R. Tewari and G.K. Dey, *Surf. Coat. Technol.* 235 (2013) 741.
- [124] M. Mohapatra, R.M. Kadam, R.K. Mishra, D. Dutta, P.K. Pujari, C.P. Kaushik, R.J. Kshirsagar, B.S. Tomar, S.V. Godbole, *Nucl. Instrum. Methods B* 269 (2011) 2057.
- [125] L. Stoch, M. Sroda, *J. Mol. Struct.* 511–512 (1999) 77.
- [126] K. El-Egili, *Physica B* 325 (2003) 340.
- [127] U. Harder, P. Reich, W. Willfahrt, *J. Mol. Struct.* 349 (1995) 297.
- [128] W.W. Peng, P. Roy, L. Favaro, E. Amzallag, J.B. Brubach, A. Congeduti, M.A. Guidi-Cestelli, A.M. Huntz, J. Barros, R. Tétot, *Acta Mater.* 59 (2011) 2723.
- [129] M. Schubert, T.E. Tiwald, C.M. Herzinger, *Phys. Rev. B* 61 (2000) 8187.

- 
- [130] A. Boumaza, L. Favaro, J.Lédion, G. Sattonnay, J.B. Brubach, P. Berthet, A.M. Huntz, P. Roy, R. Tétot, *J. Solid State Chem.* 182 (2009) 1171.
- [131] T. Furukawa, W.B. White, *J. Mater. Sci.* 16 (1981) 2689.
- [132] D. Maniu, T. Iliescu, I. Ardelean, S. Cinta-Pinzaru, N. Tarcea and W. Kiefer, *J. Mol. Struct.* 651-653 (2003) 485.
- [133] H.W. Nesbitt, G.M. Bancroft, G.S. Henderson, R. Ho, K.N. Dalby, Y. Huang, Z. Yan, *J. Non-Cryst. Solids* 357 (2011) 170.
- [134] T. Asahi, S. Nakayama, T. Nanba, H. Kiyono, H. Yamashita, T. Maekawa, *J. Ceram. Process. Res.* 9 (2008) 401.
- [135] Y. Miura, H. Kusano, T. Nanba, S. Matsumoto, *J. Non-Cryst. Solids* 290 (2001) 1.
- [136] W.J. Dell, P.J. Bray, S.Z. Xiao, *J. Non-Cryst. Solids* 58 (1983) 1.
- [137] M.M. Smedskjaer, Q. Zheng, J.C. Mauro, M. Potuzak, S. Mørup, Y. Yue, *J. Non-Cryst. Solids* 357 (2011) 3744.
- [138] G. El-Damrawi, W. Müller-Warmuth, *Phys. Chem. Glasses* 34 (1993) 52.

## List of publications included in the present thesis

1. Infrared and X-ray photoelectron spectroscopy studies on sodium borosilicate glass interacted with thermally oxidized aluminides formed on Alloy 690

**C. Yusufali**, R.J. Kshirsagar, Jagannath, R.K. Mishra, R.S. Dutta and G.K. Dey, *J. Non-Cryst. Solids* 366 (2013) 54-58.

2. Surface studies on aluminized and thermally oxidized Alloy 690 substrates interacted with nitrate-based simulated nuclear waste and sodium borosilicate melt using Raman spectroscopy and X-ray photoelectron spectroscopy

**C. Yusufali**, R.J. Kshirsagar, Jagannath, R. Halder, G.J. Abraham, R.K. Mishra, C.P. Kaushik, R.S. Dutta and G.K. Dey, *Surf. Coat. Technol.* 266 (2015) 31-37.